

2011-01-01

An Experimental Study On The Effect Of Particle Geometry On Drag And Flow Behaviors In A Packed Fluidized Bed

Md Mahamudur Rahman

University of Texas at El Paso, mmrahman@miners.utep.edu

Follow this and additional works at: https://digitalcommons.utep.edu/open_etd



Part of the [Oil, Gas, and Energy Commons](#)

Recommended Citation

Rahman, Md Mahamudur, "An Experimental Study On The Effect Of Particle Geometry On Drag And Flow Behaviors In A Packed Fluidized Bed" (2011). *Open Access Theses & Dissertations*. 2371.

https://digitalcommons.utep.edu/open_etd/2371

This is brought to you for free and open access by DigitalCommons@UTEP. It has been accepted for inclusion in Open Access Theses & Dissertations by an authorized administrator of DigitalCommons@UTEP. For more information, please contact lweber@utep.edu.

AN EXPERIMENTAL STUDY ON THE EFFECT OF PARTICLE GEOMETRY
ON DRAG AND FLOW BEHAVIORS IN A PACKED FLUIDIZED BED

MD MAHAMUDUR RAHMAN

Department of Mechanical Engineering

APPROVED:

Ahsan Choudhuri, Ph.D., Chair

Norman Love, Ph.D.

Vinod Kimar, Ph.D.

Benjamin C. Flores, Ph.D.
Acting Dean of the Graduate School

Copyright
by
Md Mahamudur Rahman
2011

Dedication

To my family who supported me throughout my career

AN EXPERIMENTAL STUDY ON THE EFFECT OF PARTICLE GEOMETRY
ON DRAG AND FLOW BEHAVIORS IN A PACKED FLUIDIZED BED

by

MD MAHAMUDUR RAHMAN, B.S.ME

THESIS

Presented to the Faculty of the Graduate School of

The University of Texas at El Paso

in Partial Fulfillment

of the Requirements

for the Degree of

MASTER OF SCIENCE

Department of Mechanical Engineering

THE UNIVERSITY OF TEXAS AT EL PASO

August 2011

Acknowledgements

At the very beginning, I would like to thank our creator for providing me such great opportunities of studying and learning till now. Also, I would like to thank all the people around me who have made this thesis possible. I am very grateful to my mother for her continuous support throughout my career and even for this thesis also.

Next I would like to thank my supervisor and committee chair Dr. Ahsan Choudhuri for allowing me to work with him and in his Center for Space Exploration Technology Research (cSETR) lab as a graduate research assistant. For the last one and half years, he enriched my knowledge by continuously providing me guidance regarding how to work for a project, what things are required to be considered, how to do those things. He has always suggested me to work hard, try to learn more to achieve the success in life. He is always inspiring me to communicate with people, to try to learn from everywhere, to build a successful career.

Then I would like to thank Dr. Norman Love, my co-supervisor for his continuous support through guiding me regarding my research works, course works, paper writing, presentation making. He spent huge time with me to show me how to write a paper, how to present in front of people, even in the weekends. He showed me the way how to organize a paper, even this thesis also. I'm extremely thankful to him for his technical and theoretical support. When I was not able to find any way how to do an experiment, he worked with me in the lab, did the experiments, even showed me how to use some useful data acquisition, and data analysis software. He was with me all the time for the last one and half year. Every time I faced any problem with anything, he just raised his hand for me. I am really grateful to him.

I would like to thank Mr. Nathaniel Robinson, Assistant Director Center for Space Exploration Technology Research, for keeping us always careful regarding the safety considerations, for approving and processing my purchase orders within a very short time.

A special thank goes to all my cSETR lab friends, especially Mr. Bidhan, Mr. Vishwanath for giving me technical and mental support all the time, and even they helped me in my project.

I would like to thank Mechanical Engineering Machine Shop people Mr. David Powell, Mr. Angel Lerma for giving me huge support in building my experimental setup. I am really grateful to all the Mechanical Engineering Department staffs for their kind help that they provided me to make this thesis possible.

Finally, the financial support provided by the U.S Department of Energy under awards DE-FOA-0000173 (Project Manager Robie Lewis) through the Graduate Assistance is gratefully acknowledged.

Abstract

Gasification offers a promising solution to producing fuels effectively in the coming years by providing a low-cost energy system, clean environmental performance, and reliability. Feedstock is prepared and fed to a gasifier in either a dry form or as slurry (mixed with water). One application of this technology uses heat, pressure, and steam to convert feedstock into a gaseous mixture, composed primarily of carbon monoxide (CO) and hydrogen (H₂), named as syngas. Several technical and commercial issues were identified by the Nation Energy Technology Laboratory (NETL) in 2006 Multiphase workshop. US Department of Energy (DOE) is now focusing on attaining a significant development in the design and operation of multiphase flow devices. They postulated different short-term, long term research goals to modify and develop these device performances by the year 2015.

Despite previous efforts to develop the fundamentals of flow field in a fluidized bed reactor, most of them are based on spherical particles whereas actual beds are operated on non-spherical particles. Hence, this thesis focuses on presenting the hydrodynamic analysis of a packed fluidized bed operated with both spherical and non-spherical particles to generate fundamental idea useful for designing the non-spherical particle based fluidized bed reactor. For this purpose, gas phase analysis and particle scale motion analysis were performed in this study. Pressure fluctuations and high speed imaging analysis were utilized to characterize the bed behavior in semi-dilute flow (less than 4% in this work). To present the effect of bed diameters on fluidization behavior, a plexiglass tube with 3.8 cm outside diameter and a quartz tube with 12 cm outside diameter were employed. Pressure fluctuations at different bed heights were also analyzed.

Borosilicate spherical glass beads with a 1mm diameter and crushed non-spherical particles with diameters between 150 to 2000 μm were used for the experimental analysis. This thesis also presents a method to analyze the particle sphericity, particle size distribution, and particle characterization. Mapping of several bed pressure drops with superficial gas velocity across the bed are presented showing the minimum fluidization, full fluidization, and terminal velocity. MatPIV analysis of high speed images, captured at 500 frames per second, and PIV analysis with 62 Hz CCD camera and 5 Amp laser showing the flow field vectors, magnitude of velocity, vorticity for both spherical and non-

spherical particles, are also presented to characterize the bed behavior at particle scale motion. The pressure fluctuations with spherical particles show more uniform behavior with spherical particles than the non-spherical particles and the increased bed height produce more uniform pressure fluctuation response. Drag coefficient analysis for non-spherical particle diameters between 500 to 600 μm , 600 to 710 μm , 710-850 μm , 850-1180 μm and 1180-2000 μm were conducted in this work to generate a fundamental idea regarding the required uplifting drag force for fluidizing the particles in a packed bed.

Table of Contents

Acknowledgements.....	v
Abstract.....	vii
Table of Contents.....	ix
List of Tables	xiii
List of Figures.....	xiv
Chapter 1: Introduction.....	1
1.1 General overview.....	1
1.2 Fundamentals of multiphase flow.....	2
1.3 brief description of fluidized bed.....	3
1.4 organization of Thesis.....	3
1.5 statement of objectives	4
1.6 Relevance and outcomes.....	4
1.8 Facilities and other resources.....	4
Chapter 2: Literature Review.....	6
2.1 gasification.....	6
2.2 Fluidized bed reactors.....	9
2.3 gas-solid flows in Fluidized bed reactors	14
2.3.1 Particle Selection	14
2.3.2 Flow Regimes	16
2.3.4 Bed Pressure Drop	17
2.3.5 Minimum Fluidization Velocity	18
2.3.6 Terminal Velocity	20
2.3.7 Full Fluidization.....	21
2.4 Drag correlations	23
2.5 Research Works	26
Chapter 3: Technical Approach	29
3.1 Fluidized bed Systems	29
3.2 1 st Generation Fluidized Bed System Components	31
3.2.1 Fluidized Bed Column.....	31

3.2.2	Flow Straighter	31
3.2.3	Mesh Catch	31
3.2.4	Compressor	32
3.2.5	Fluid Supply System.....	33
3.2.6	Needle valve	33
3.2.7	Digital Mass Flow Meter	33
3.2.8	Pressure Regulator	34
3.3	2nd Generation Fluidized Bed System Components	34
3.3.1	Fluidized Bed Column.....	34
3.3.2	Flow Straighter	35
3.3.3	Mesh Catch	36
3.3.4	Blower.....	36
3.3.5	Fluid Delivery System	37
3.3.6	Butterfly Valve	37
3.3.7	Thermal Mass Flow Meter.....	38
3.4	Pressure Measurement	38
3.4.1	Differential Pressure Transducer	38
3.4.2	External Power Supply	40
3.5	Data Acquisition	41
3.5.1	Terminal Block	41
3.5.2	LabVIEW	41
3.5.3	Digital Manometer.....	412
3.6	High Speed Imaging	42
3.7	MatPIV	43
3.7.1	Image Format.....	43
3.7.2	Image Contrast.....	44
3.7.3	Coordinate System.....	45
3.7.4	Image Masking	46
3.7.5	Noise Filtering	47
3.7.6	Integral and Differential Quantities	47
3.8	PIV (Particle Image Velocimetry)	47
3.9	Particle Production.....	49
3.9.1	Hydraulic Compressor	49
3.9.2	Die and Punch.....	49

3.9.3 Precision Balance.....	50
3.9.4 Sieve Shaker and Sieves	50
3.10 Drag Analysis	51
3.10.1 Microscopic Video Camera	51
3.10.2 Dino Capture Software	52
3.10.3 Hopper	52
3.10.4 High Speed Camera	52
3.10.5 Methodology	53
3.11 Test Matrix.....	54
3.12 Instruments Used	55
3.13 Operating Conditions.....	56
3.14 Experimental Uncertainties	56
Chapter 4: Results and Discussions	57
4.1 Results From 1 st Generation Fluidized Bed.....	57
4.1.1 Results for Spherical Particles	57
4.1.2 Results for Non-Spherical Particles.....	62
4.1.3 Effect of Particle Sphericity.....	68
4.1.4 Analytical and Experimental Pressure Drop Comparison	69
4.1.5 Analytical and Experimental U_{mf} Comparison	69
4.2 Results From 2 nd Generation Fluidized Bed	69
4.2.1 Results for Spherical Particles	70
4.2.2 Results for Non-Spherical Particles.....	82
4.2.3 Effect of Particle Sphericity.....	91
4.3 Effect Of Bed Diameter	92
4.4 Drag Analysis Results.....	93
4.4.1 Single Particle Drag Analysis.....	93
4.4.2 Multiple Particle Drag Analysis	95
Chapter 6: Summary and Conclusions	99
6.1 Summary Of Results.....	99
6.2 Conclusions.....	101
6.3 Recommendations For Further Study	103

References.....	105
Appendix A.....	108
Sample Calculations	108
Particle Mean Size	108
Analytical Bed Pressure Drop	108
Gas Superficial Velocity.....	109
Error Analysis.....	109
Terminal Velocity of Free Falling Single Rice Grain	110
Flow Blockage Ratio	111
Appendix B.....	112
Key Parts and Instruments Specifications	112
Appendix C.....	115
Nomenclature.....	115
Curriculum Vita.....	116

List of Tables

Table 2.1: Some Industrial Applications of Fluidized Bed Reactors.	10
Table 2.2: Different Drag Correlations.....	24
Table 3.1(a): Test Matrix (Pressure Measurement).....	55
Table 3.1(b): Test Matrix (Drag Measurement).	55
Table 3.2: List of Instruments Used for the Current Study.	55
Table 3.3: Operating Conditions.....	56
Table 3.4: Accuracy Results for 2 nd Generation Bed ($U_{mf}=1.67$ m/s).	56
Table 3.5: Accuracy Results for 1 st Generation Bed with Spherical Particles ($U_{mf}=.94$ m/s).	56
Table 3.6: Accuracy Results for 3.8 cm Bed with Non-Spherical Particles ($U_{mf}=.94$ m/s).....	56
Table 4.1: Physical Properties of Borosilicate Glass Particles.	58
Table 4.2: Analytical and Experimental Pressure Drop Variance (1 st Gen).....	69
Table 4.3: Analytical and Experimental U_{mf} Variance (1 st Gen).....	69
Table 4.4: Analytical and Experimental Pressure Drop Variance (2 nd Gen).....	75
Table 4.5: Analytical and Experimental U_{mf} Variance (2 nd Gen).....	75

List of Figures

Chapter 2 Literature Review

Figure 2.1: Cross-Section of Sasol's First Gasifier	6
Figure 2.2: Products of Coal-Gasification Process.....	7
Figure 2.3: Example of Pyrolysis	8
Figure 2.4: Example of Oxidation and Reduction	9
Figure 2.5: Types of Fluidized Bed Reactors	11
Figure 2.6: A Typical fluidized bed.....	12
Figure 2.7: Bubbling Fluidized Bed	13
Figure 2.8: Example of Circulating Bed.....	13
Figure 2.9: Vibrating Fluidized Bed.....	14
Figure 2.10: The Geldar's Classification of Particle	15
Figure 2.11: Progressive Change in Flow Regimes with Gas Velocity	16
Figure 2.12: Bed Performance with Respect to the Gas Velocity	18
Figure 2.13: Bed Behavior at Minimum Fluidization	19
Figure 2.14: Pressure Drop in a Bubbling Fluidized Bed.....	21
Figure 2.15: Bed Stages at Different Flow Rate.....	22
Figure 2.16: Behavior of a Bed Illustrating Various Regimes	22
Figure 2.17: Force Balance on a Particle Moving in an Upward Stream	23
Figure 2.18: Measured Drag Coefficient	26
Figure 2.19: Drag Coefficients of Several Simple 3D and 2D Shape	26

Chapter 3 Technical Approach

Figure 3.1: Schematic of 1 st Generation Fluidized Bed.....	29
Figure 3.2: Experimental Setup of 1 st Generation Fluidized Bed.....	30
Figure 3.3: Experimental Setup of 2 nd Generation Fluidized Bed.....	30
Figure 3.4: Honeycomb Shaped Distributor for 1 st Generation Fluidized Bed	31
Figure 3.5: Mash Catch.....	32
Figure 3.6: Rotary Screw Air Compressor	32
Figure 3.7: SS Integral Bonnet Angle-Pattern Needle Valve	33
Figure 3.8: Omega Digital Mass Flow Meter	33
Figure 3.9: SMC AC40-N04C3-Z Air Filter, Pressure Regulator & Lubricator.....	34
Figure 3.10: Fluidized Bed Section	36
Figure 3.11: Flow Distributor for 2 nd Generation Bed	36
Figure 3.12: Mesh Catch for 2 nd Generation Bed	36
Figure 3.13: High Pressure Blower	36
Figure 3.14: Fluid delivery system	37
Figure 3.15: Wafer Style Butterfly Valve.....	37
Figure 3.16: Thermal Mass Flow Meter	38
Figure 3.17: Omega PX277-30D5V Differential Pressure Transmitter	39
Figure 3.18: Wiring Diagram for the Pressure Transducer	39
Figure 3.19: Switch Configuration for the Pressure Transducer	40
Figure 3.20: External Power Supply.....	40
Figure 3.21: National Instruments Data Acquisition Device (DAQ)	41

Figure 3.22: LabVIEW Virtual Instrument File	42
Figure 3.23: HHP 4252 Digital Manometer	42
Figure 3.23: FASTCAM Super 10 K High Speed Camera	43
Figure 3.24: High Speed Particle Motion Captured at (a) Minimum Fluidization Velocity (b) Transition and (c) Full Fluidization Showing Zoomed Portion of the Test Section.....	43
Figure 3.25: Pixel Region of RGB Image	44
Figure 3.26: Pixel Region of Gray Scale Image	44
Figure 3.27: Gray Scale Image with Initial Contrast	45
Figure 3.28: Gray Scale Image with Final Contrast	45
Figure 3.29: World Coordinate System	46
Figure 3.30: Masking Out the Region	46
Figure 3.31: PIV System.....	48
Figure 3.32: High Speed Image for PIV Analysis	48
Figure 3.33: Hydraulic Compressor	49
Figure 3.34: Die and Punch	49
Figure 3.35: Precision Balance	50
Figure 3.36: Sieve Shaker and Sieves.....	50
Figure 3.37: Schematic of Drag Analyzing Equipment.....	51
Figure 3.38: Dino Capture Microscopic Video Camera.....	51
Figure 3.39: Hopper	52
Figure 3.40: Dantec High Speed Camera	52
Figure 3.41: Vertical Motion of Single Free Falling Rice Grain.....	53
Figure 3.42: (A) Horizontal motion and (B) Inclined motion of a free falling rice grain	54

Chapter 4 Results and Discussions

Figure 4.1: Spherical Glass Beads	67
Figure 4.2: Bed (1 st Gen) Performance Curve with Spherical Particles	68
Figure 4.3: Images for MatPIV Analysis for Spherical Particles	69
Figure 4.4: Instantaneous flow field vector with spherical particles (1 st Gen.).....	60
Figure 4.5: Instantaneous velocity magnitude with spherical particles (1 st Gen.).....	60
Figure 4.6: Instantaneous vorticity with spherical particles (1 st Gen.)	61
Figure 4.7: Bed Expansion at U_{mf} with Channeling (spherical particles).....	61
Figure 4.8: Bubble Collapse for Spherical Particles.....	62
Figure 4.9: Non-Spherical Glass Particles.....	62
Figure 4.10: Particle Size Distribution	63
Figure 4.11: Bed (1 st Gen) Performance Curve with Non-Spherical Particle	64
Figure 4.12: MatPIV Images for Non-Spherical particles.....	65
Figure 4.13: Instantaneous flow field vector with non-spherical particles (1 st Gen.)	65
Figure 4.14: Average velocity vector with non-spherical particles (1 st Gen.).....	66
Figure 4.15: Instantaneous vorticity with non-spherical particles (1 st Gen.)	66
Figure 4.16: Bed Expansion at U_{mf} with Channeling Non-Spherical Particles	67
Figure 4.17: Bubble Collapse for Non-Spherical Particles	67
Figure 4.18: Particles Staked to the Column due to Electrostatic Buildup	68
Figure 4.19: Bed (1 st Gen) Performance Curve with Spherical and Non-Spherical particles	68
Figure 4.20: Bed (2 nd Gen) Performance Curve with Spherical Particles	70
Figure 4.21: Bed (2 nd Gen) Performance Curve at Different Bed Heights (without Honeycomb).....	71
Figure 4.22: Bed (2 nd Gen) Performance Curve at Different Bed Heights (with Honeycomb)	71

Figure 4.23: Bed (2 nd Gen) Performance Curve with and without the Honeycomb (2cm Bed)....	72
Figure 4.24: Bed (2 nd Gen) Performance Curve with and without the Honeycomb (2.5cm Bed)....	73
Figure 4.25: Bed (2 nd Gen) Performance Curve with and without the Honeycomb (3cm Bed)....	73
Figure 4.26: Bed (2 nd Gen) Performance Curve with and without the Honeycomb (4 cm Bed)....	74
Figure 4.27: Bed (2 nd Gen) Performance Curve with and without the Honeycomb (5cm Bed)....	74
Figure 4.28: (a) Particle Image for PIV Analysis Showing (b) a Zoomed Section	76
Figure 4.29: Instantaneous flow field vector for 3 cm bed height (2 nd Gen).....	77
Figure 4.30: Average flow field vector at 3 cm bed height (2 nd Gen)	77
Figure 4.31: Instantaneous vorticity at 3cm bed height (2 nd Gen).....	78
Figure 4.32: Instantaneous flow field vector at 5 cm bed height (2 nd Gen).....	78
Figure 4.33: Average flow field vector at 5 cm bed height (2 nd Gen)	79
Figure 4.34: Instantaneous vorticity at 5 cm bed height (2 nd Gen).....	79
Figure 4.35: Fixed Bed Regime (2 nd Gen).....	80
Figure 4.36: Bed (2 nd Gen) at U_{mf}).....	81
Figure 4.37: Bubbling Bed Regime (2 nd Gen)	81
Figure 4.38: Turbulent Churning Regime (2 nd Gen)	82
Figure 4.39: Particle Size Distribution for 12 cm Bed	83
Figure 4.40: Particles for Sphericity Analysis	84
Figure 4.41: Particle Longest Diameter Tracking	84
Figure 4.42: Correction Factor Measurement	85
Figure 4.43: Particle Classification	85
Figure 4.44: Bed (2 nd Gen) Performance with Non-Spherical Particles.....	86
Figure 4.45: Bed (2 nd Gen) Performance Curve at Different Bed Heights (without honeycomb) ..	87
Figure 4.46: Bed (2 nd Gen) Performance Curve at Different Bed Heights (with honeycomb)	87
Figure 4.47: Bed (2 nd Gen) Performance curve with and without honeycomb (2.5 cm Bed)	88
Figure 4.48: Bed (2 nd Gen) Performance curve with and without honeycomb (3 cm Bed)	89
Figure 4.49: Instantaneous flow field vector at 3 cm bed height (2 nd Gen).....	89
Figure 4.50: Average flow field vector at 3 cm bed height (2 nd Gen)	90
Figure 4.51: Instantaneous vorticity at 3 cm bed height (2 nd Gen).....	90
Figure 4.52: Bed Performance with Spherical and Non-Spherical Particles without Honeycomb ..	91
Figure 4.53: Bed Performance with Spherical and Non-Spherical Particles with Honeycomb ..	92
Figure 4.54: Effect of Bed Diameter on Bed Performance	93
Figure 4.55: Magnified Photograph of Rice Grains	94
Figure 4.56: Scaling of the Camera Frame.....	95
Figure 4.57: Drag Coefficient for $\Phi=.53$	96
Figure 4.58: Drag Coefficient for $\Phi=.58$	96
Figure 4.59: Drag Coefficient for $\Phi=.63$	97
Figure 4.60: Drag Coefficient for $\Phi=.68$	97
Figure 4.61: Drag Coefficient for all Sphericities	98

Chapter 1: Introduction

1.1 GENERAL OVERVIEW

Coal gasification, one of the most versatile, and clean technologies, is a thermo-chemical process which breaks down coal or any carbon based feedstock into its basic chemical constituents, and converts them into electricity, hydrogen, and other valuable products rather than direct burning of them. The feedstock is prepared and fed to the gasifier in either a dry form or as slurry (mixed with water). In the gasifier, which is a robust reactor vessel and is the heart of the gasification processes, the feedstock break apart when exposed to steam and carefully controlled amounts of air or oxygen under high temperature and pressure in a reducing (oxygen-starved) atmosphere, and initiates chemical reactions which produces the syngas made up primarily of carbon monoxide, and hydrogen, and smaller quantities of carbon dioxide, and methane (CH_4). At this point, fluidized bed reactors offer the advantages of excellent solid mixing, and heat transfer characteristics¹.

Gas-solid flows in a fluidized bed reactor are exceedingly complex, and involve multiple (time and length) scales with interaction of phases. Hence, in order to design, optimize, and to control the gas-solid flows in a fluidized bed reactor, it is necessary to obtain information characterizing the system transport properties such as pressure fluctuations, particle, and fluid velocity profiles, and drag coefficient. In order to acquire this information, Laser Doppler Anemometry (LDA), Particle Image Velocimetry with MatLab (MatPIV), PIV, and Digital Image Analysis (DIA) were employed in this report. Pressure fluctuations were used to determine the minimum fluidization and terminal velocities. Different particle concentrations were employed to investigate the bed behavior at dense and dilute flows (at 6% solids volume fraction).

It is often difficult to measure the motion of the particles in a fluidized bed experimentally. As such, computational techniques are rapidly emerging as means of capturing the full range of bed hydrodynamics, and as a tool for plant level design². This thesis focuses on presenting a method of obtaining the full-field visualization of rotational motions of solid particles in a fluidized bed, and then incorporating the acquired data into simulation software to verify the results. Generally two different approaches can be used to model the gas-solid flows, one is continuum approach, regularly known as

Eulerian approach, analyzes all the particles as a continuum, and the second one is combined continuum, also named as Molecular Dynamics (MD) or Discrete Element Model (DEM) or Lagrangian Approach, treats each particle separately³. This thesis also focuses on simulating the gas-solid flows in a fluidized bed using the Eulerian Approach to represent both the gas and solid phases.

1.2 FUNDAMENTALS OF MULTIPHASE FLOW

The term multiphase flow represents any fluid flow that consists of more than one phase of fluid having some level of phase or component separation at a scale well above the molecular level. Eventually many processing technologies deal with multiphase flow, from cavitating pumps and turbines to electro-photographic processes to papermaking to the pellet form of almost all raw plastics. In these processes, large amount of coal, granular material, grain, ore, etc., are transported and require these materials to flow at many stages. For this reason, the effectiveness and the efficiency of those processes largely depend on the ability to predict the fluid flow behavior of these processes. Multiphase flow can be usually identified into two general topologies, one is disperse flow, and the other one is separated flow. Flow that consists of finite particles, drops or bubbles distributed in a connected volume of the continuous phase, is termed as the disperse flow. On the other hand flow consisting of two or more continuous streams of different fluids separated by interfaces is named as the separated flow.

The study of multiphase flow postulates the need to model and predict the detailed behavior of those flows, and the phenomena that they manifest. These models can be explored in three ways: (1) experimentally, where laboratory-sized models are equipped with appropriate instrumentation, (2) theoretically, where mathematical equations and models are employed to analyze the flow, and (3) computationally, where the power and memory size of modern computers are used to identify the complexity of the flow.

In disperse flows, two types of computational models are prevalent, one is the trajectory model, and another one is the two-fluid model. The motion of the fluid in disperse phase is evaluated by following either the motion of the actual particles or the motion of larger, representative particles, in the trajectory model. On the other hand, the disperse phase is treated as a second continuous phase intermixed and interacting with the continuous phase in the two-fluid model. In contrast, the single

phase fluid flow equations in the two streams, coupled through appropriate dynamic and kinematic conditions at the interface, can be solved for separated flows⁴.

1.3 BRIEF DESCRIPTION OF FLUIDIZED BED

When fluid flows through a packed bed at such a velocity that the bed becomes loosened, and the solid-fluid mixture behaves like a fluid, then the bed is said to be a fluidized bed. The fluid velocity is maintained sufficient enough to make the solid particles suspended, but not large enough to carry the particles out of the bed. The solid particles swirl around the bed rapidly to obtain vigorous agitation of the solids in contact with the fluid, and create excellent mixing among the solid particles, and the fluid. The fluidized material in a fluidized bed is almost always a solid, and the fluidized medium is either a liquid or a gas. The behavior of the fluidized bed largely depends on the properties of the solid particles and the fluid, and the excellent mixing of the solid and the fluid enables the fluidized bed to maintain nearly uniform temperature even in highly exothermic reaction situations where the particles catalyze a reaction in the species contained in the fluid⁶. That is why; fluidized beds find wide application in catalyst regeneration, solid-gas reactors, combustion of coal, roasting of ores, drying, and gas adsorption operations⁵.

1.4 ORGANIZATION OF THESIS

Chapter 1 introduces the importance of fluidized beds as well as their application in fossil energy systems. Brief description of fundamentals of multiphase flow, research objectives, and laboratory facility information are also included in this chapter. Chapter 2 summarizes the literature review on the coal gasification process, different fluidized bed reactors, fluidization behavior of a fluidized bed, flow field phenomena of gas-solid flows, different regimes of flow, and presents different correlations for drag coefficient. Chapter 3 gives an outline of the design, construction and components of the experimental setup. It also provides a brief review on previous setup design to show the research progress from its initial approach. Chapter 4 explains the methodology used to estimate bed pressure, fluid and particle velocity, and drag coefficient. Chapter 5 presents the results including discussion about the theoretical and experimental values. Finally chapter 6 provides summary and conclusion about this project as well as future recommendations for the future work on fluidized beds.

1.5 STATEMENT OF OBJECTIVES

The overall thesis goal is to develop a fundamental idea of a packed fluidized bed by characterizing the bed with different flow regimes, bed pressure drop with respect to increasing gas superficial velocity, and particle scale motion with high speed imaging technique in a semi-dilute flow (volume fraction of less than 10%). This thesis also initiates the production of enough drag analysis data which will be used for developing an empirical drag correlation to estimate the uplifting force required by the solid particles while fluidizing. This thesis outlines the following objective:

1. To obtain full-field visualization of rotational motion of both spherical and non-spherical particles.
2. To evaluate drag force on non-spherical particles.

1.6 RELEVANCE AND OUTCOMES

The 2006 Multiphase Workshop organized by the National Energy Technology Laboratory (NETL) identified several issues that cut across the four tracks, which can be grouped into four categories: Numerical algorithm and software development, Theory and model development, Physical and computational experiments, and Communication, collaboration, and education. This workshop postulated a set of near-midterm, mid-term, and long-term research needs in each of the mentioned four tracks to attain a significant development in the design, operation, and troubleshooting of multiphase flow devices in fossil fuel processing plants by the year 2015. These needs include further developments in theory, laboratory scale experiments for measuring various physical and transport properties, code development, and validation of computer models¹. A novel diagnostic technique was used in this work to generate engineering data useful for design processes for both spherical and non-spherical particle based solid-fluid system.

1.8 FACILITIES AND OTHER RESOURCES

The necessary experiments, including testing and analysis, were performed at the Center for Space Exploration and Technology Research (cSETR) laboratory located in the Mechanical Engineering Department at The University of Texas at El Paso, having the adequate fluid dynamics instrumentation including a Laser Doppler Velocimeter (LDV), a high speed 2kHz Particle Image Velocimeter (PIV), a

stereo PIV, high speed and infrared imaging system, various flow controllers, flow meters, and high speed data acquisition system, a high pressure compressor, a high pressure and high flow rate blower, a microscopic video camera, a hydraulic compressor, a sieve shaker.

Chapter 2: Literature Review

2.1 GASIFICATION

Gasification uses heat, pressure, and steam to convert feedstock into a gaseous mixture, composed primarily of carbon monoxide (CO) and hydrogen (H₂), named as syngas. The feedstock is prepared and fed to a robust reactor vessel named as gasifier in either a dry form or as slurry (mixed with water)⁷. Figure 2.1 shows the cross-section of a gasifier used to perform the coal gasification process.

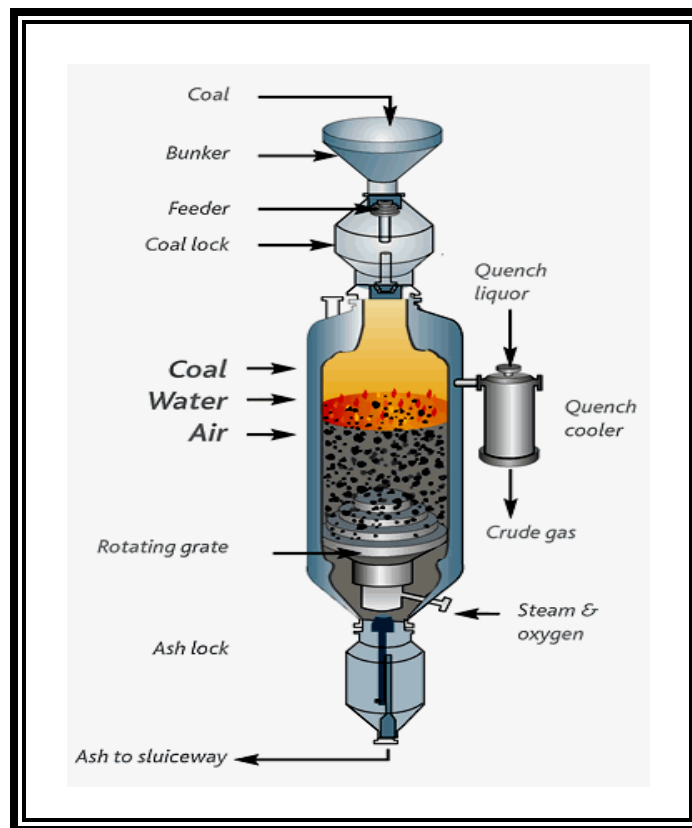


Figure 2.1: Cross-section of Sasol's first gasifier⁸

The raw syngas from the gasifier is driven through the treatment facilities for gas cleaning, conditioning, and separation, and then depending on the desired applications, Figure 2.4 shows the products and by-products are extracted from the clean syngas.

In the power production process, supplied purified syngas from the gasification side of the plant to the power side of the plant, is mixed with air and then ignited to drive the combustion turbine. The combustion turbine ignites the syngas-air mixture in a combined thermal and mechanical process and

releases energy that is converted to electrical power by the generator. The generated electric power is then fed to the electric grid for distribution.

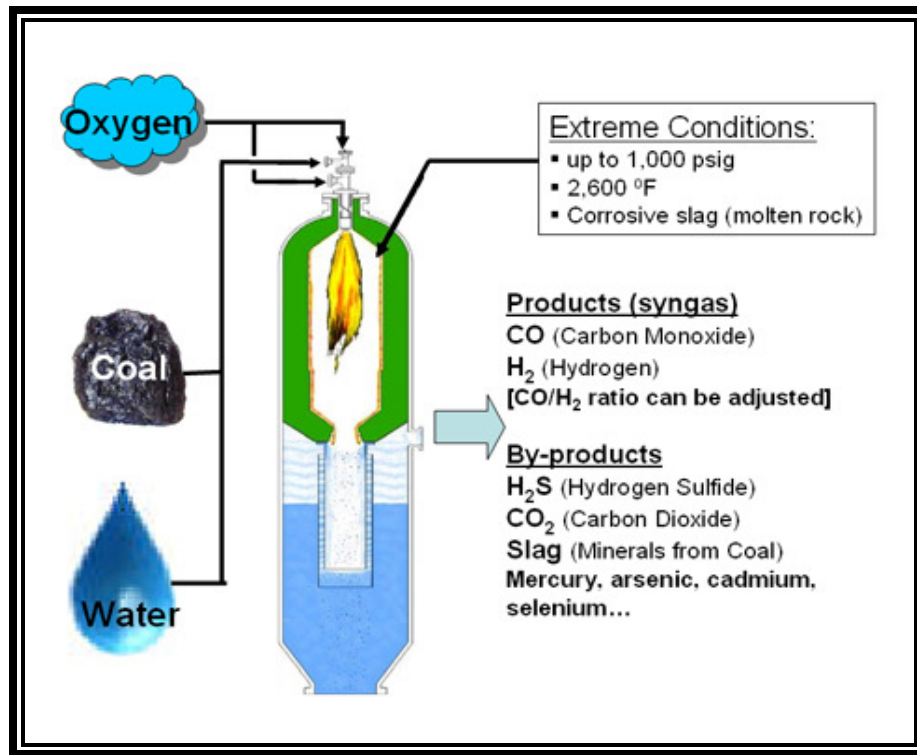


Figure 2.2: Products of coal-gasification process¹

Gasification process was originally developed to produce town gas from coal for lighting and cooking in the early 1800s. By the early 1900s, electricity and natural gas replaced the general public use of syngas. Since the 1920s, gasification process has been largely used to produce synthetic fuels and chemicals, especially during the times of war. Today, the use of gasification system as an energy source is causing huge interest due to increasing global fuel costs¹.

Gasification offers enormous promising worldwide applications in the coming years for its low-cost energy system, clean environmental performance, reliability, product flexibility, near-zero emissions, high efficiency, energy security, and fuel flexibility. To make gasification process more efficient, user friendly, more reliable, more economic, the Department of Energy (DOE) is taking a two-pronged approach. One approach is to ensure long-term technology improvements and the other one is to make the current research advances applicable to commercial application. Various project works are

going on at lab, bench, and pilot scales to ensure continued developments of the gasification technology, and to bring the small scale research works into commercial application, FutureGen and NETL are working together and trying to develop a technology base for the highly efficient, cost-effective, fuel-flexible future power plants¹.

The feedstock particles then undergo three thermal and chemical processes (1) Pyrolysis, (2) Oxidation, and (3) Reduction.

2.1.1 Pyrolysis

Pyrolysis is a chemical breakdown of complex compounds under heat where volatile substances such as methane, tar, and hydrogen are released and a combustible substance char is produced. This production of char reduces the weight of coal up to 70 percent. Figure 2.2 presents the simplified depiction of pyrolysis chemistry.

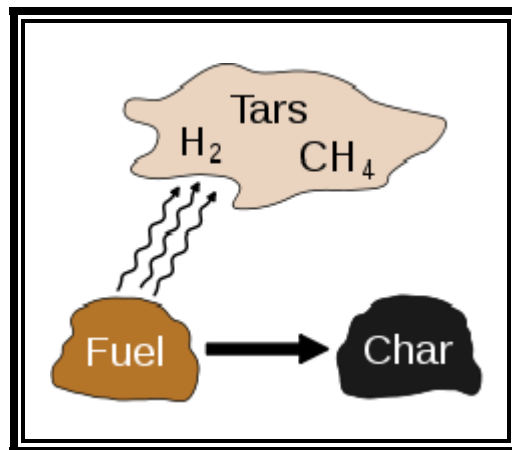


Figure 2.3: Example of pyrolysis⁹

2.1.2 Oxidation

The volatile products released and some of the char formed in Pyrolysis goes to exothermic reaction with air or oxygen and form carbon monoxide and carbon dioxide. Figure 2.3 shows the fundamentals of the oxidation process.

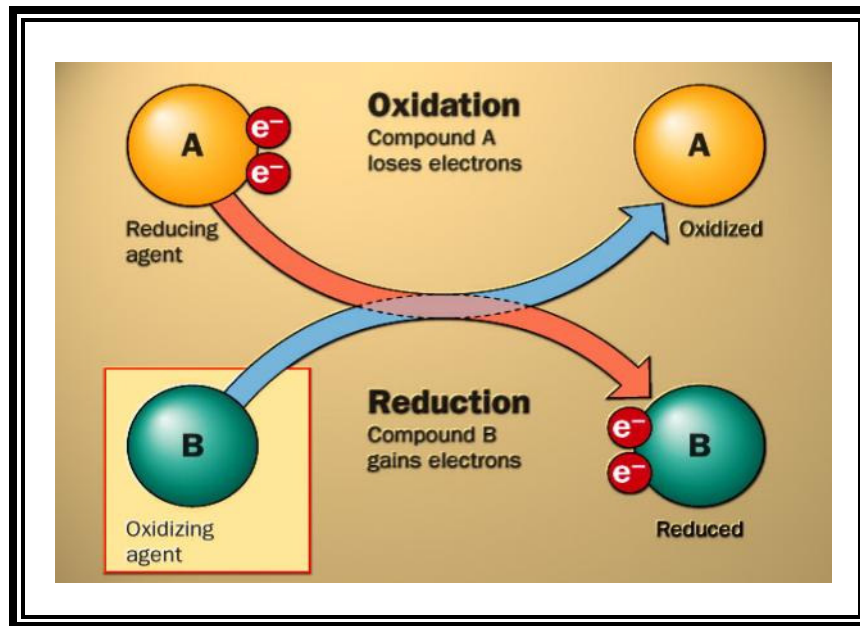


Figure 2.4: Example of Oxidation and Reduction¹⁰

2.1.3 Reduction

The char then reacts with the carbon dioxide and steam to produce carbon monoxide and hydrogen. This carbon monoxide, hydrogen, some methane then forms the gaseous mixture known as syngas. Slag is the waste product of this process.

2.2 FLUIDIZED BED REACTORS

A fluidized bed reactor is a device where a fluid (gas or liquid) is passed through a granular solid material at high velocities so that the solid becomes suspended and behaves as though it were a fluid to carry out a variety of multiphase chemical reactions. Fritz Winkler in Germany in the 1920s first developed the fluidized bed gas generator. In United States, the fluidized bed reactor found its first application in a petroleum industry as the Catalytic Cracking Unit created in Baton Rouge, LA in 1942 by the Standard Oil Company of New Jersey which is now known as Exxon Mobil Company. Today this reactor finds wide applications in petrochemical, chemical, metallurgical, and energy industries due to its excellent solid mixing and heat transfer phenomena⁵. Some typical applications and flow regimes prevailing in these reactors are presented in Table 2.1.

Table 2.1: Some Industrial Applications of Fluidized Bed Reactors⁵

Processes/applications	Operating regime
Fluidized bed catalytic cracking (FCC)	Riser reactor: fast-fluidized bed regime Regenerator: bubbling bed/turbulent fluidized bed regime
Maleic anhydride/phthalic anhydride	Turbulent fluidized bed regime
Acrylonitrile	Bubbling/turbulent bed regime
Ethylene dichloride	Bubbling/turbulent bed regime
Polymerization of olefins (polyethylene/polypropylene)	Bubbling/turbulent fluidized bed regime
Coal gasification	Turbulent fluidized bed regime
Fischer-Tropsch synthesis	Dense phase/fast-fluidized bed regime
Acrylonitrile/metacrylonitrile	Bubbling/turbulent bed regime
Calcination/roasting of ores	Bubbling/turbulent bed regime
Incineration of solid waste	Bubbling/turbulent bed regime

In the fluidized bed reactor, solid particles are usually supported by a porous plate distributor, and the fluid is passed through the distributor up through the solid materials. Since at the lower fluid velocities the fluid passes through the voids, the solids remain steady, and this bed is termed as the packed bed reactor. With increasing the fluid velocity, the force of the fluid tries to balance the weight of the solid particles. The stage where the force of the fluid equals the weight of the solid particles is termed as incipient fluidization, and it occurs at minimum fluidization velocity. The solid particles then start to expand and swirl around as the fluid velocity surpasses the minimum fluidization velocity, and this stage the reactor is known as the fluidized bed.

Depending on different flow regimes and different configuration of beds, several varieties of fluidized bed reactors are used in practice as shown in Figure 2.5.

Bubbling fluid beds offer excellent solid mixing and bed-to-wall heat transfer characteristics due to the gross circulation of solid particles in gas bubbles. This circulation of solids counterbalances the tendency of denser particles settling at the bottom of the bed when the fluidization occurs in a bubbling bed of wide particle size distribution and widely varying density. Hence, at the gas velocity close to the minimum fluidization velocity, solid segregation dominates and at very large velocity, circulation of solids dominates in the process.

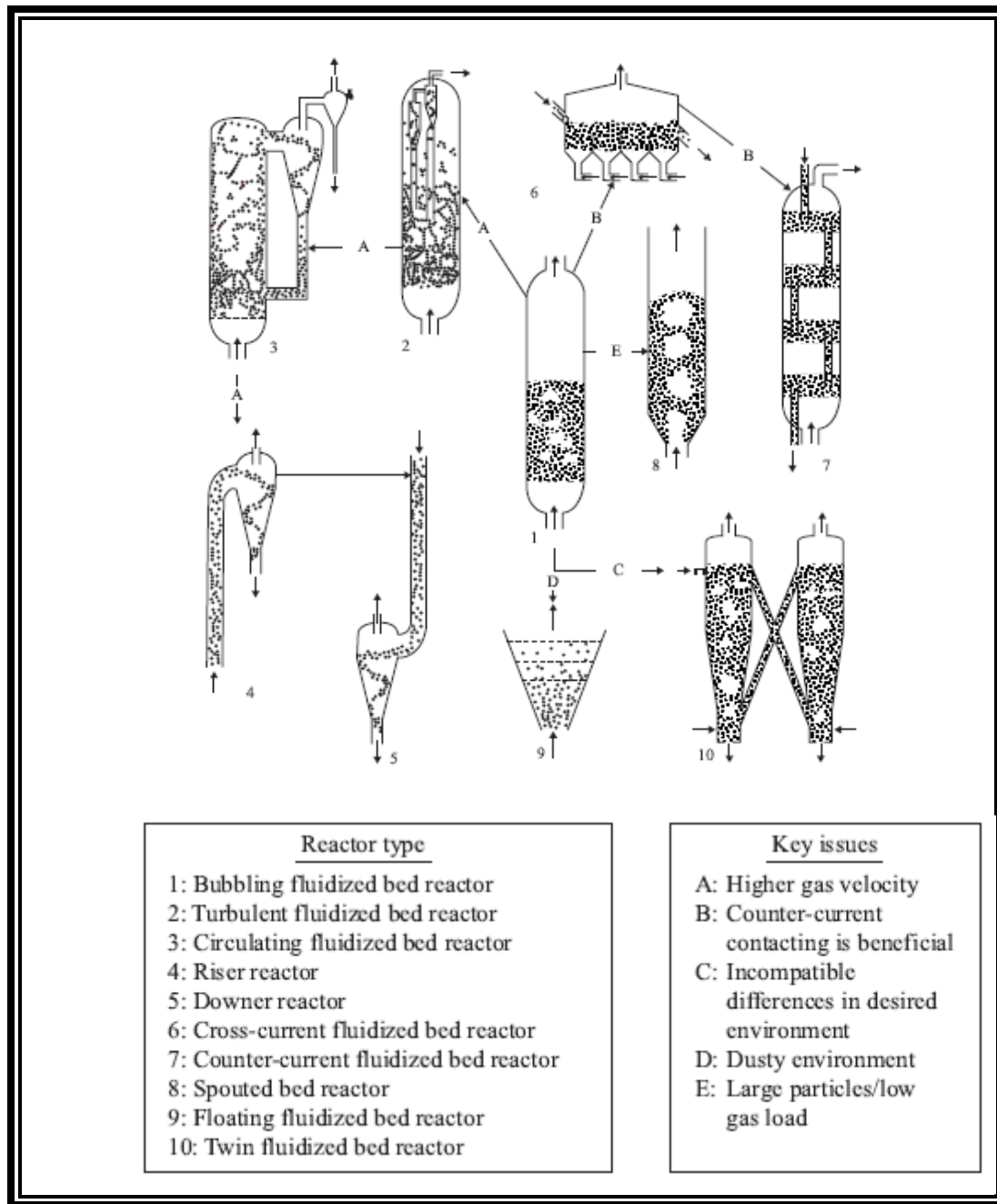


Figure 2.5: Types of Fluidized Bed Reactors¹⁵

The riser reactors are operated in the fast fluidized regime, where the gas superficial velocity becomes greater than twenty times the terminal settling velocity of solids. The solids flow down in the near wall region and flow up through the central core in this type of bed.

A typical fluidized bed schematic is shown in Figure 2.6.

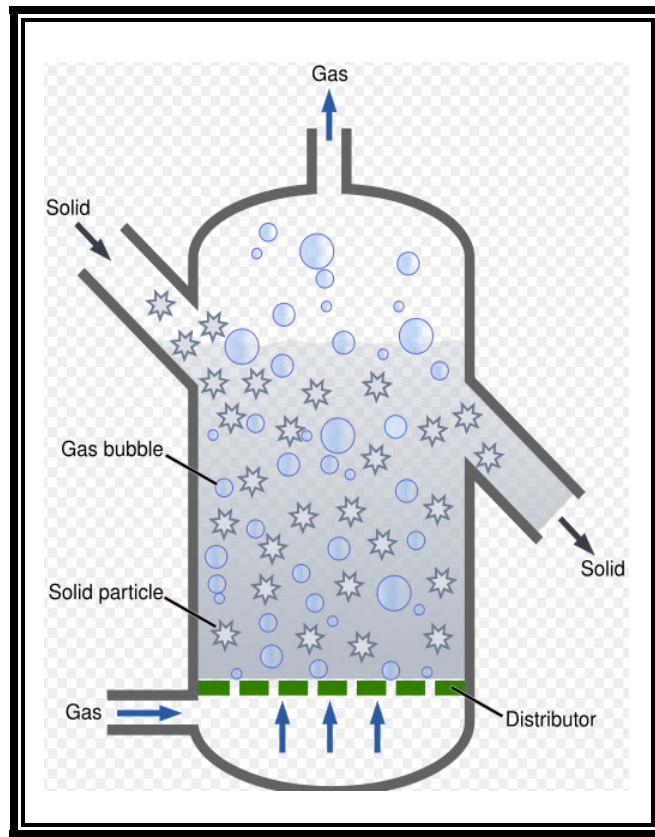


Figure 2.6: A typical fluidized bed¹⁵

Fluidized bed can be coarsely classified by the flow behavior of fluid, including¹¹ (1) Stationary bed, (2) Circulating bed, (3) Vibratory bed.

2.2.1 Stationary or Bubbling Bed

In this type of bed, the fluidization of the solids exhibits relatively stationary behavior with some fine particles being entrained. Figure 2.5 shows the bubbling fluidized bed with combustion system.



Figure 2.7: Bubbling Fluidized Bed¹²

2.2.2 Circulating Bed

The particle bed gets suspended by the fluidization due to a large kinetic energy of the fluid in this type of bed, and large particles can be entrained from the bed due to the coarseness of the bed. A circulating Fluidized bed is shown in Figure 2.6.

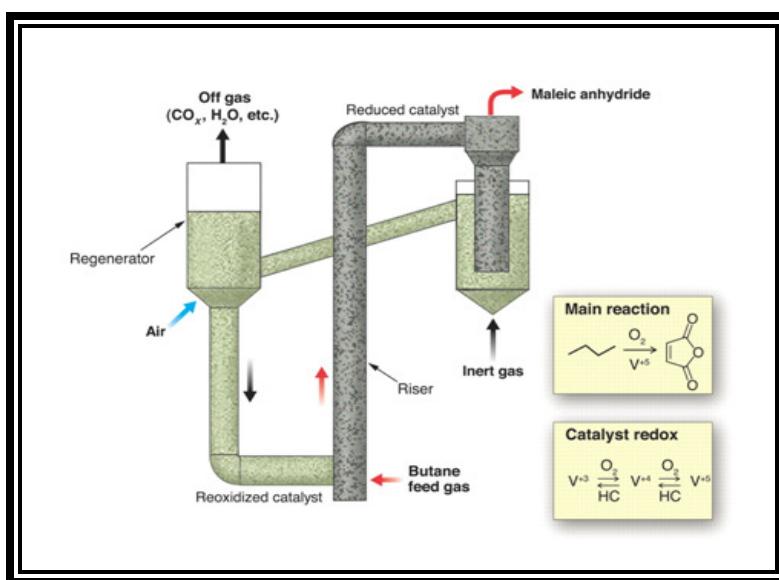


Figure 2.8: Example of Circulating Bed¹³

2.2.3 Vibratory Bed

This type of bed uses an additional mechanical vibration to excite the particles more for increased entrainment with respect to stationary beds. Figure 2.7 presents an example of vibrating fluidized bed.



Figure 2.9: Vibrating Fluidized Bed¹⁴

2.3 GAS-SOLID FLOWS IN FLUIDIZED BED REACTORS

Depending on operating conditions, solids flow rate, gas flow rate, and system configuration, different types of flow regime ranging from fixed bed to pneumatic conveying are observed as fluid is passed through the bed of particles. Moreover, the quality of fluidization is significantly affected by the particle size distribution, particle shape, density, and restitution coefficient⁵.

2.3.1 Particle Selection

Based on particle size and particle density, Geldart in 1973 suggested a simple, four-grouped classification of solid particles to categorize the range of bed behavior. This classification of particles is known as Geldart's classification which is shown in Fig. 2.10. Though several other properties of solid such as angularity, composition, surface roughness may affect the fluidization quality, Geldart's classification chart can be used as an initial tool to analyze the fluidization quality of a specific gas-solid system.

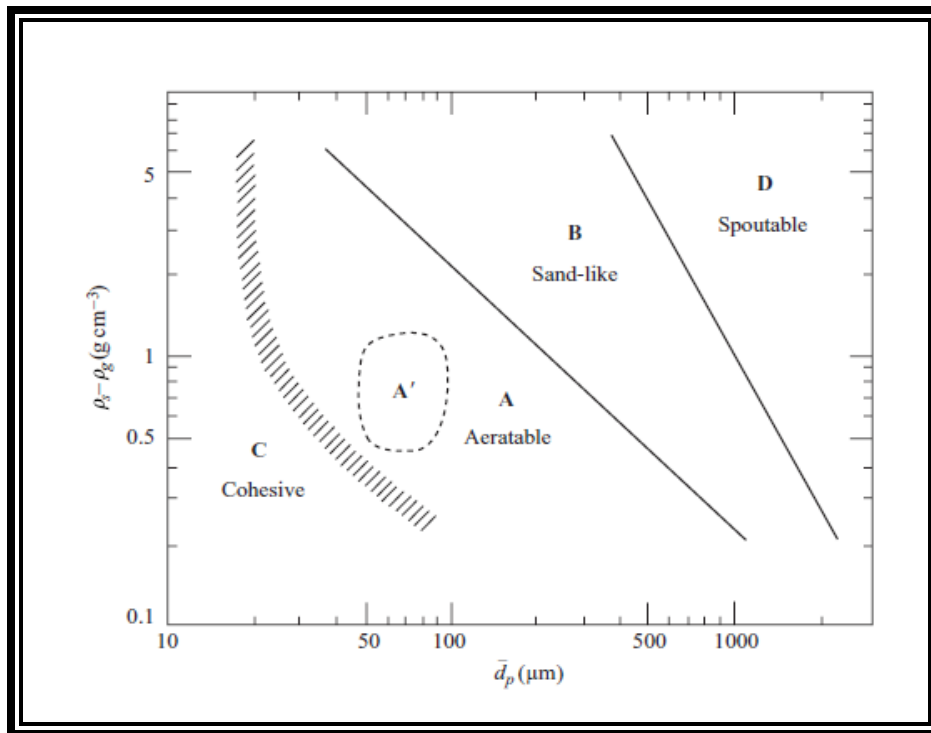


Figure 2.10: The Geldar's classification of particles⁵

Group A

Solid particles with smooth fluidization at low gas velocity and at higher velocity bubbling or turbulent fluidization, and having low particle density ($< \sim 1500 \text{ kgm}^{-3}$) or small mean particle size are included in this group. Due to decreased bulk density, beds from these particles usually expand by a factor of 2 to 3 at incipient fluidization. Fluid catalytic cracking processes use this class as catalysts.

Group B

This class contains solid particles whose size varies from $40 \mu\text{m}$ to $500 \mu\text{m}$, and whose density varies from 1400 kgm^{-3} to 4000 kgm^{-3} . These solids form bubbles which grow in size and fluidize vigorously; e.g. sand particles.

Group C

This group includes extremely fine and subsequently the most cohesive particles such as cement, flour, starch etc. With this class, normal fluidization is very difficult to achieve and since channeling takes place, it may require some external forces like mechanical agitation.

Group D

These solids are large and/or dense and usually processed in shallow beds or in the spouting mode. This group requires very high fluid energies and severe channeling or large exploding bubbles are typically associated with high levels of abrasion⁵.

2.3.2 Flow Regimes

When the velocity of fluid is low, the solid particles rest on the distributor and this regime is termed as the fixed bed regime. Some commonly encountered gas-solid flow regimes, and the relationship between these flow regimes, type of solids, and fluid velocity are presented in Figure 2.11.

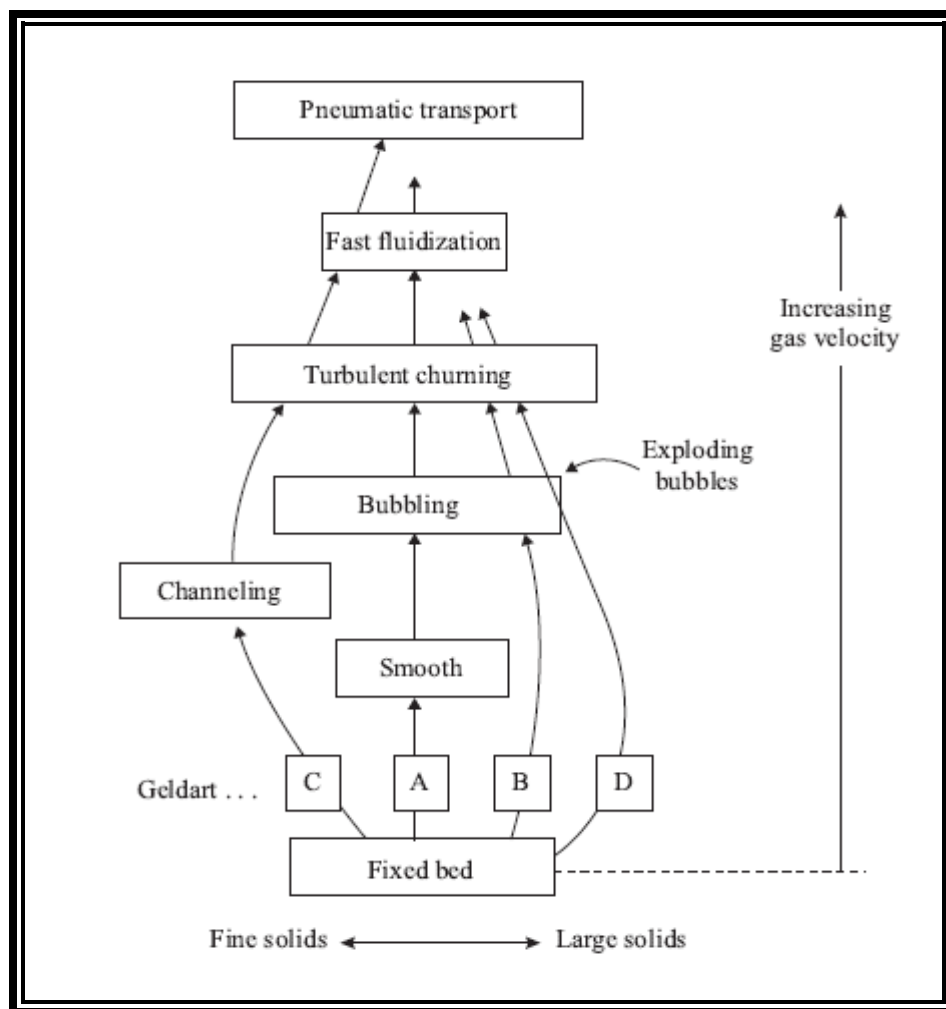


Figure 2.11: Progressive change in flow regimes with gas velocity⁵

With increasing the superficial gas velocity, minimum fluidization occurs where the bed starts to expand and all the particles get just suspended. Beyond the minimum fluidization velocity, smooth fluidization occurs for fine solid particles up to minimum bubbling velocity. As the superficial gas velocity is increased after the minimum bubbling velocity, bubbling starts, and the bed is said to be bubbling bed or heterogeneous fluidized bed. Gas bubbles generated in this regime coalesce and grow as they move upward through the bed.

For deep beds of small diameter, the bubbles from the bubbling fluidized bed grow large enough to spread across the diameter of the column. This is known as the slugging bed regime. In case of large diameter columns, if the gas superficial velocity is further increased, then turbulent motion of solid clusters and void of gas of different shape and size are observed instead of slugs, and this regime is named as turbulent fluidized bed regime. In the fast fluidization regime, gas-solid separators (cyclones) are used to capture the solid particles since the solid entrainment becomes very high. All the solids are transported out of the bed with increasing the superficial gas velocity beyond the fast fluidization regime, and termed as the pneumatic transport regime⁵.

Figure 2.12 shows a widely used regime map developed by Grace in 1986⁶. From the regime map it can be understood that for fine solids, class A and B of Geldart's classification, a bubbling bed exhibits stable operation over a wide range of operating conditions, and the operating range becomes narrow for larger particles, class D particles of Geldart's classification. Again, for smaller particles, bubbling starts when the gas superficial velocity becomes 3 to 8 times higher the minimum fluidization velocity and continues far beyond the terminal velocity whereas bubbling occurs immediately after the minimum fluidization velocity for larger particles⁶. From the regime map it can also be seen that fast fluidization is possible for small particles only, and it can happen at very high superficial gas velocity approximately at the velocity equal to thousand times the minimum fluidization velocity.

2.3.4 Bed Pressure Drop

The pressure drop across the bed can be calculated by following equation¹⁶,

$$\Delta p = \frac{M}{\rho_p A} (\rho_p - \rho_f) g \quad 2.1$$

Where M is the total mass of the particles ρ_p is the density of particles ρ_f is the density of fluid and A is the cross-sectional area of the bed.

If the fluid density is negligible compared to particle density, the equation can be rewritten as,

$$\Delta p = \frac{Mg}{A} \quad 2.2$$

Figure 2.12 shows the bed behavior in function of pressure drop across the bed and the superficial gas velocity.

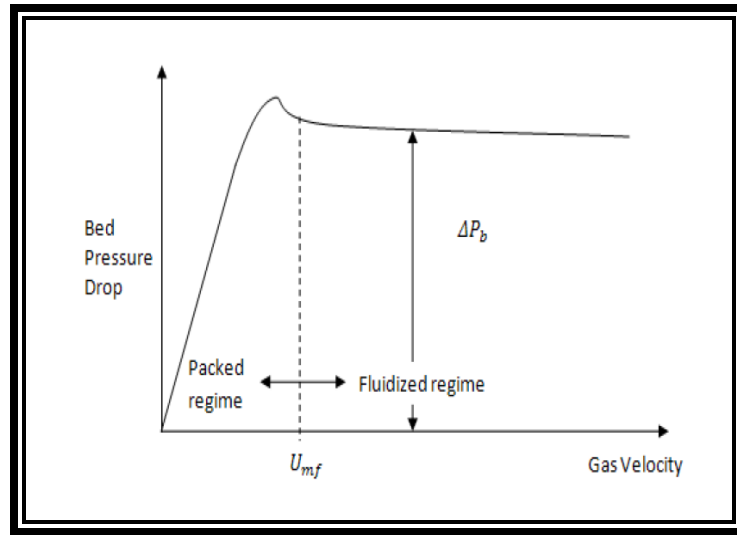


Figure 2.12: Bed Performance with respect to the gas velocity¹⁶

2.3.5 Minimum Fluidization Velocity

At the beginning, the bed is fixed with a certain height with no flow and zero pressure drops. As the superficial gas velocity is increased, the pressure drop is gradually increased while the bed remains fixed. With increasing the gas velocity, a point is reached where the bed starts expanding in height, solid particles get just suspended by upward flowing gas. The weight of the particles is counterbalanced by the frictional force between the particles and the gas⁵. At this point the fluidization starts, and the bed pressure drop starts to remain unchanged, and the superficial gas velocity at this point, is known to be minimum fluidization velocity and denoted as U_{mf} . Figure 2.13 shows the bed performance at minimum fluidization.

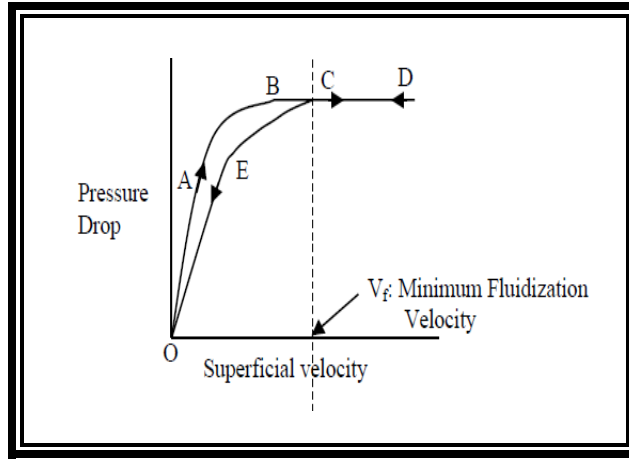


Figure 2.13: Bed behavior at minimum fluidization¹⁷

The commonly employed **Ergun equation** associated with the bed pressure drop is given below¹⁸.

$$f_p = \frac{150}{Re_p} + 1.75 \quad 2.3$$

Here, f_p is the friction factor for the packed bed and Re_p is the Reynolds number. Both of them are defined as follows.

$$f_p = \frac{\Delta p}{L} \frac{D_p}{\rho U_s^2} \left(\frac{\varepsilon^3}{1-\varepsilon} \right) \quad 2.4$$

$$Re_p = \frac{D_p U_s \rho}{(1-\varepsilon)\mu} \quad 2.5$$

Where,

Δp : Pressure Drop

L : Length of the Bed

D_p : Equivalent spherical diameter of the particle defined by,

$$D_p = 6 \frac{\text{Volume of the particle}}{\text{Surface area of the particle}} \quad 2.6$$

ρ : Density of the fluid

μ : Dynamic viscosity of fluid

U_s : Superficial velocity defined by,

$$U_s = \frac{Q}{A} \quad 2.7$$

Where Q is volumetric flow rate of the fluid and A is the cross-sectional area of the bed.

ε : Void fraction of the bed define by,

$$\varepsilon = \frac{\text{Void volume of the bed}}{\text{Total volume of the bed}} \quad 2.8$$

The minimum fluidization velocity can be calculated by balancing the upward force exerted on the bed and the net weight of the bed while ignoring the frictional force exerted on the wall of the bed by the flowing fluid⁹.

Upward force on the bed = $\Delta p A$

Volume of particles = $(1 - \varepsilon)AL$

Net weight of the particles = $(1 - \varepsilon)(\rho_p - \rho_f)ALg$

Where, g is the acceleration due to gravity.

Balancing the net weight of the particles and upward force on the bed,

$$\Delta p = (1 - \varepsilon)(\rho_p - \rho_f)Lg \quad 2.9$$

For a bed of small particles ($D_p \leq 0.1 \text{ mm}$) the flow conditions at the minimum fluidization velocity are such that the Reynolds number is relatively small ($Re \leq 10$). Hence, the Kozeny-Carman Equation which is applicable to the viscous flow regime can be used to establish the point of onset of fluidization, and the resulting equation for minimum fluidization velocity is given below.

$$U_{mf} = \frac{(\rho_p - \rho_f)gD_p^2 \varepsilon^3}{150\mu(1 - \varepsilon)} \quad 2.10$$

For larger particles ($D_p \geq 1 \text{ mm}$), the full Ergun equation must be used to calculate the minimum fluidization velocity due to dominating inertial effects. Again, void fraction for spherical particles can be used in a range between 0.40-0.45.

2.3.6 Terminal Velocity

At minimum fluidization velocity, the fluidization starts with keeping the bed pressure drop unchanged, and this condition continues until a point is reached where the differential pressure gets just higher the weight of the bed causing the solid particles to be carried away by the upward flowing gas from the bed. The superficial gas velocity at this point is termed as the terminal velocity or settling velocity. Considering smaller particles, the terminal velocity can be calculated using the Stokes law as follows¹⁷:

$$U_T = \frac{(\rho_p - \rho_f)gD_p^2}{18\mu} \quad 2.11$$

2.3.7 Full Fluidization

Figure 2.14 shows that initially the solid particles stay packed on the distributor with no pressure drop and no gas flow. With increasing the superficial gas velocity, the bed pressure drop also increases but the bed height remains fixed. This stage continues until point A after which the particles start to lose contact with each other. The particles become extremely loose at point B, and with further increase in velocity the bed starts expanding, i.e., minimum fluidization occurs at point F. While increasing the superficial gas velocity more, the bed continues expanding with constant bed pressure drop up to the point P where the particles are entrained by the fluid, i.e., reaches to the terminal velocity¹⁸. The region from minimum fluidization velocity to the terminal velocity region is referred to as the full fluidization region. Figure 2.15 shows the fluidized bed stages at different flow rates.

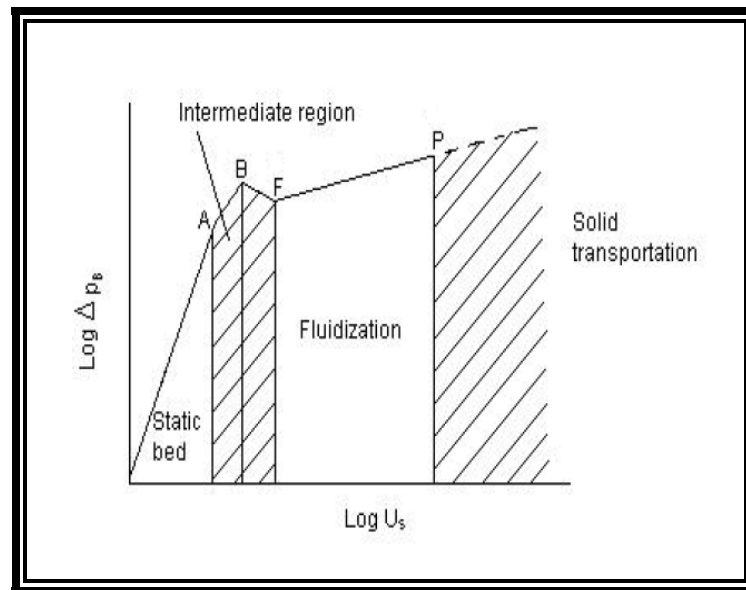


Figure 2.14: Pressure Drop in a Bubbling Fluidized Bed¹⁷

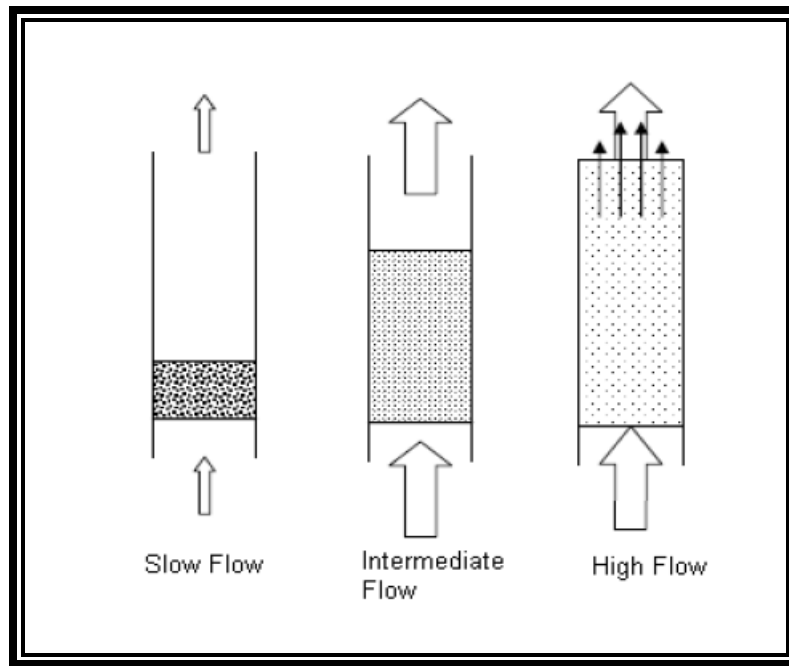


Figure 2.15: Bed Stages at Different Flow Rates¹⁹

The various regions characterizing the behavior of a bed are illustrated in Figure 2.16⁶. The rising portion of the plot is the region covered by the Ergun equation and the region where the bed pressure drop remains constant over a wide range of velocities is the bubbling fluidization region. After this section, fast fluidization and pneumatic transport regions are observed.

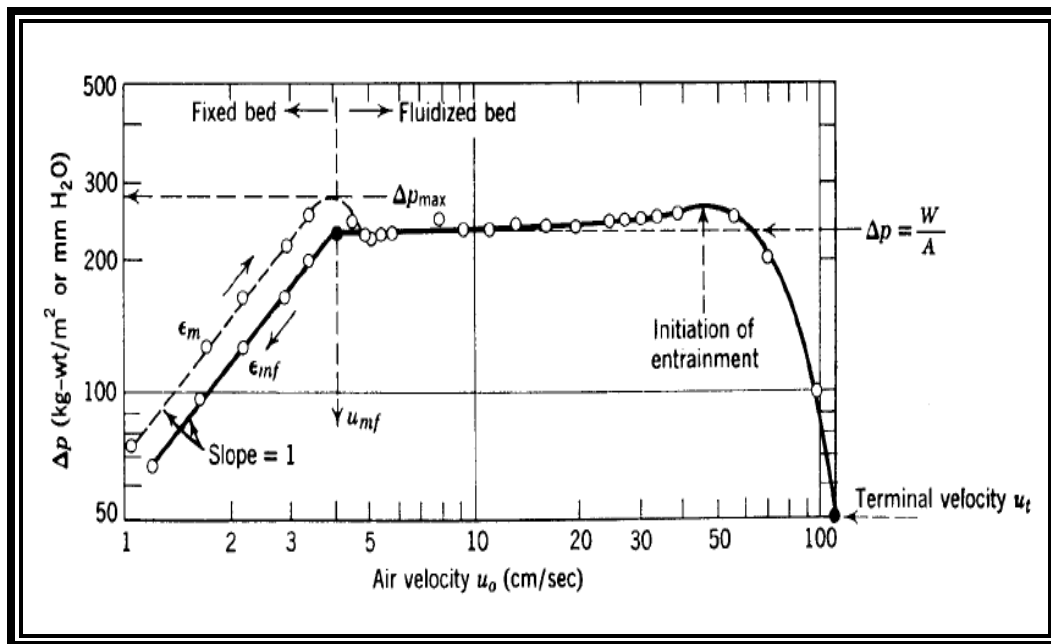


Figure 2.16: Behavior of a bed illustrating various regimes⁶

2.4 DRAG CORRELATIONS

When a particle moves in the upward direction along with the fluid, it experiences a fluid drag due to the relative velocities resisting its free fall under gravity. The force balance under steady condition is usually written as,

$$\text{Gravitational force} = \text{Buoyancy force} + \text{Drag force}$$

Figure 2.17 show how a particle moves in the direction of the fluid flow by opposing the effect of gravity with buoyancy force and fluid drag²⁰.

A wide range of choices exist to estimate drag coefficient for spherical particles. Some of them are presented in Table 2.2.

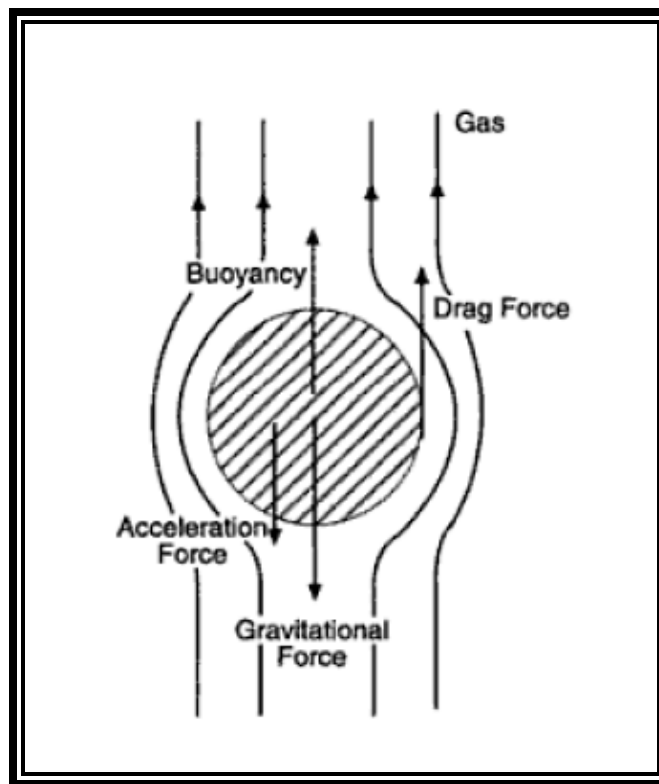


Figure 2.17: Force balance on a particle moving in an upward stream²¹

Table 2.2: Different drag correlations

Year	Author	Correlation	Reynolds number range	Eqn. No.
1948	Dallavale ²²	$C_D = (0.63 + 4.8 \text{Re}_p^{-0.5})^2$	$\text{Re}_p < 2 \times 10^5$	(2.12)
1954	Fair and Geyer ²³	$C_D = \frac{24}{R} + \frac{3}{\sqrt{R}} + 0.34$	$R < 1 \times 10^4$	(2.13)
1972	Ihme et al. ²⁴	$C_D = 24 / \text{Re}_p + 5.48 \text{Re}_p^{-0.573} + 0.36$	$\text{Re}_p < 800$	(2.14)
1978	Clift et. Al ²³	$C_D = \frac{24}{R} + \frac{3}{16}$ $C_D = \frac{24}{R} [1 + 0.1315R^{(0.82-0.05w)}]$ $C_D = \frac{24}{R} [1 + 0.1935R^{0.6305}]$ $\log C_D = 1.6435 - 1.1242w + 0.1558w^2$ $\log C_D = -2.4571 + 2.5558w - 0.9295w^2 + 0.1049w^3$ $\log C_D = -1.9181 + 0.6370w - 0.0636w^2$ $\log C_D = -4.3390 + 1.5809w - 0.1546w^2$ where $w = \log R$	$R < 0.01$ $0.01 \leq R \leq 20$ $20 \leq R \leq 260$ $260 \leq R \leq 1,500$ $1,500 \leq R \leq 1.2 \times 10^4$ $1.2 \times 10^4 \leq R \leq 4.4 \times 10^4$ $4.4 \times 10^4 \leq R \leq 3.38 \times 10^5$	(2.15)
1986	Flammer and Banks ²³	$C_D = \frac{24}{R} 10^E$ where $E = 0.261R^{0.369} - 0.105R^{0.431} - \frac{0.124}{1 + (\log R)^2}$	$R < 8.6 \times 10^4$	(2.16)
1986	Turton and Levenspiel ²³	$C_D = \frac{24}{R} (1 + 0.173R^{0.657}) + \frac{0.413}{1 + 16,300R^{-1.09}}$	$R < 2.6 \times 10^5$	(2.17)
1987	Khan and Richardson ²³	$C_D = (2.25R^{-0.31} + 0.36R^{0.06})^{3.45}$	$0.01 < R < 3 \times 10^5$	(2.18)
1989	Haider and Levenspiel ²⁵	For Spherical $u_* = \left(\frac{4}{3} \frac{\text{Re}}{C_D} \right)^{\frac{1}{5}} = U_T \left[\frac{\rho_f^2}{8\mu(\rho_s - \rho_f)} \right]^{\frac{1}{5}}$ $d_* = \left(\frac{4}{3} C_D \text{Re}^2 \right)^{\frac{1}{5}} = d \left[\frac{8\rho_f(\rho_s - \rho_f)}{\mu^2} \right]^{\frac{1}{5}}$ $u_* = \left[\frac{18}{d_*^2} + \frac{0.5909}{d_*^{2.5}} \right]^{-1}$ $C_D = \frac{24}{\text{Re}} (1 + 0.1806 \text{Re}^{0.6459}) + \frac{0.4251}{1 + \frac{6880.95}{\text{Re}}}$ For non-spherical $C_D = \frac{24}{\text{Re}} [1 + 8.1716 \exp(-4.0655 \phi)] \text{Re}^{0.0964 + 0.5565 \phi}$ $+ \frac{73.69 \text{Re} \exp(-5.748 \phi)}{\text{Re} + 5.378 \exp(6.2122 \phi)}$	$R < 2.6 \times 10^5$	(2.19)
1989	Syamlal and O'brien ²⁵	$F_{gs} = \frac{3\varepsilon_s \varepsilon_g \rho_g}{4U_T^2 d_p} C_{D-\text{sphere}} \vec{v}_s - \vec{v}_g $	$\frac{d_p \vec{v}_s - \vec{v}_g \rho_g}{\mu_g}$	(2.20)
1992	Gidaspow ²⁶	$F_{gs} = \begin{cases} \frac{3}{4} C_{D-\text{sphere}} \frac{\rho_g \varepsilon_g \varepsilon_s \vec{v}_s - \vec{v}_g }{d_p} \varepsilon_g^{-2.65}, & \varepsilon_g \geq 0.8 \\ \frac{150 \varepsilon_s (1 - \varepsilon_g) \mu_g}{\varepsilon_g d_p^2} + \frac{1.25 \rho_g \varepsilon_s \vec{v}_s - \vec{v}_g }{d_p}, & \varepsilon_g < 0.8 \end{cases}$ Where, $C_{D-\text{sphere}} = \frac{24}{\text{Re}} (1 + 0.15 \text{Re}^{0.687})$ $= 0.44$	$\text{Re} \leq 1000$ $\text{Re} > 1000$	(2.21)

The experimental particle drag coefficient and Reynolds number can be calculated from the following equations²⁷:

$$C_D = \frac{4}{3} \frac{gd}{U_T^2} \frac{(\rho_s - \rho_f)}{\rho_f} \quad 2.27$$

$$Re = \frac{du\rho_f}{\mu} \quad 2.28$$

Drag coefficient for several 2D and 3D shapes are included in Figure 2.18 and Figure 2.19










Shape		Drag Coefficient
Sphere		0.47
Half-sphere		0.42
Cone		0.50
Cube		1.05
Angled Cube		0.80
Long Cylinder		0.82
Short Cylinder		1.15
Streamlined Body		0.04
Streamlined Half-body		0.09

Figure 2.18: Measured Drag Coefficient²⁸

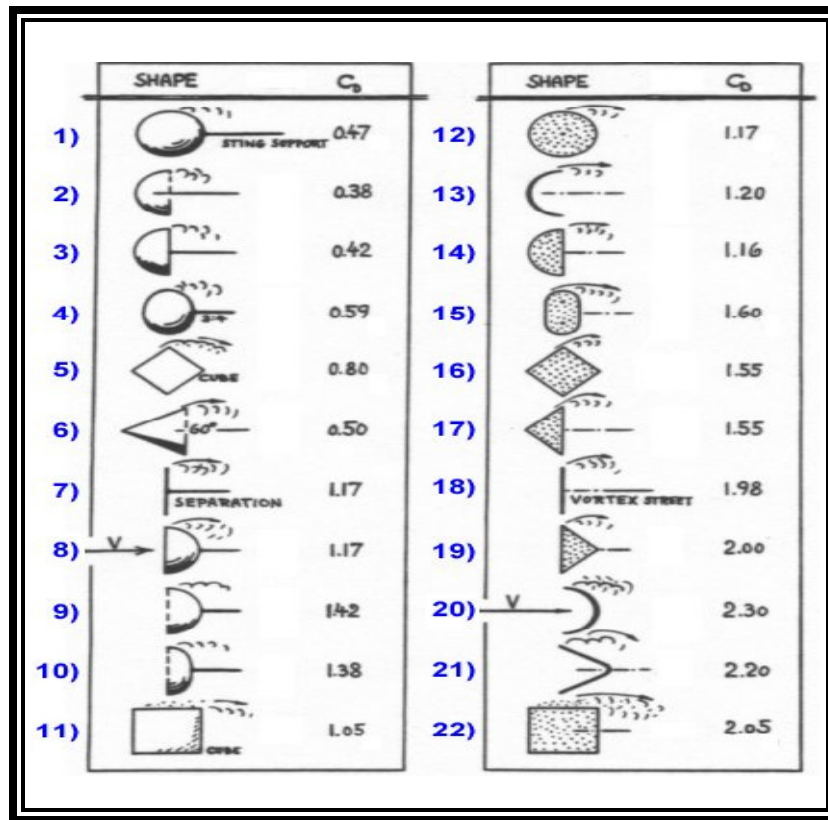


Figure 2.19: Drag coefficients of several simple 3D and 2D shapes²⁹

2.5 RESEARCH WORKS

Fluidized bed technology offers promising solution to fuel flexible combustion processes. Almost any combustible material varying from coal to municipal waste can be burned at high temperatures of 1400 to 1700 degrees F with controlling the pollutant emissions without any external expensive emission control technique¹. Fluidized bed reactors provide turbulent mixing of gas and solids by suspending the solid fuels on upward-flowing fluid which results in excellent heat transfer and chemical reactions during the combustion process.

Since a fluidized bed reactor offers enormous advantages, hence, a large amount of research works are devoted to this technology to develop fundamental ideas which will be useful for designing an efficient and reliable fluidized bed reactor. Most of the current research works are focusing on quantifying and explaining the phase interactions behavior of the fluidized bed. Extensive research works are going on to produce more reliable and accurate models of the inner movement and

characteristics of the bed so that the design of the bed can be more efficient, and the range of the fluidized bed will be expanded.

For a long period of time, researchers are working on this technology. In 1949 Ergun and Orning modeled a packed bed as a series of identical, straight, parallel channels³⁰. They developed a general equation which relates the bed pressure drop to gas flow. They showed that the ratio of pressure drop to superficial velocity is linearly related to the mass flow rate. After that Ergun introduced the particle mean size in the previous pressure drop calculations in 1952³¹. In 1971 Davidson and Harrison found that when the gas velocity has reached a value where the pressure drop is equal to the buoyant weight per unit area of the particles, minimum fluidization has been achieved. They also demonstrated that any further increase in the velocity will not have any effect in the pressure drop because the particles will rearrange so that the resistance to the flow is decreased³².

In 2006 a generalized slugging-bubbling fluidized bed reactor model was proposed to show the transition from bubbling to slugging fluidization³³. The ratio of bubble diameter to the column diameter was used to correlate the probability of different fluidization flow regimes. In 2007, Wu et. al. characterized the gas-solid flow dynamics under the ambient conditions by performing the statistical analysis of pressure fluctuations and X-ray computed tomography measurements³⁴. They used polyethylene resins as their test particles with a mean size of 677 μm . They used three columns of 10 cm, 20 cm, and 30 cm diameters and a static bed height of 40 cm for their analysis. They extracted the time-averaged voidage distribution, bubble phase area fraction, bubble diameter, and bubble number distribution varying with the bed heights.

Laverman et. al demonstrated the influence of particle raining through the roof of the bubbles on the time-averaged emulsion phase velocity profiles in a pseudo 2D fluidized bed filled with glass beads with a mean particle size distribution in the range of 400-600 μm ³⁵. Hilton et. al. reformulated the pressure-gradient force model. They modified the pressure correction method and then coupled to a discrete element model with non-spherical grains³⁶. The reactor model proposed by the Mahecha-Botero et al. was modified by Kumar and Srivastava under various operation conditions to maximize the CO conversion, Dimethyl Ether (DME) productivity, and to maximize the DME selectivity with respect to

methanol³⁷. After that they employed that modified model to simulate DME synthesis in a fluidized bed reactor.

From the Most literature of the past experimental and computational research works have been performed for the spherical particles whereas the particles are originally non-spherical in most of the fossil-fuel processes.

The Clean Coal Technology Program initiated the market entry of 1st generation pressurized fluidized bed using the stationary bubbling-bed technology with 1000 megawatts of capacity installed worldwide. These beds utilize low air velocities and steam generated from a heat exchanger to fluidize the solid fuels. The US Department of Energy is now focusing on developing more efficient, eco friendly, and fuel flexible fossil energy power plants with zero emission within the next 20 years¹. Motivated by these issues this thesis focuses on presenting the bed behavior and particle scale motion in a fluidized bed operated with both spherical and non-spherical particles.

Chapter 3: Technical Approach

This chapter aims to present the experimental equipments used to perform the hydrodynamic analysis of a fluidized bed. Apparatus used to perform the drag analysis are also included in this chapter. This chapter also focuses on providing a detailed description on data acquisition system and data analyzing equipments. The experimental methodology is also presented in this chapter. A list of instruments used, experiment operating conditions, experimental uncertainties and the test matrix are also presented in this chapter.

3.1 FLUIDIZED BED SYSTEMS

To achieve the goals of this thesis, two fluidized bed columns were employed to perform the experiments. Figure 3.1 (schematic diagram) and Figure 3.2 (original experimental setup) show the 1st generation fluidized bed. Figure 3.3 presents the 2nd generation fluidized bed system with the basic components.

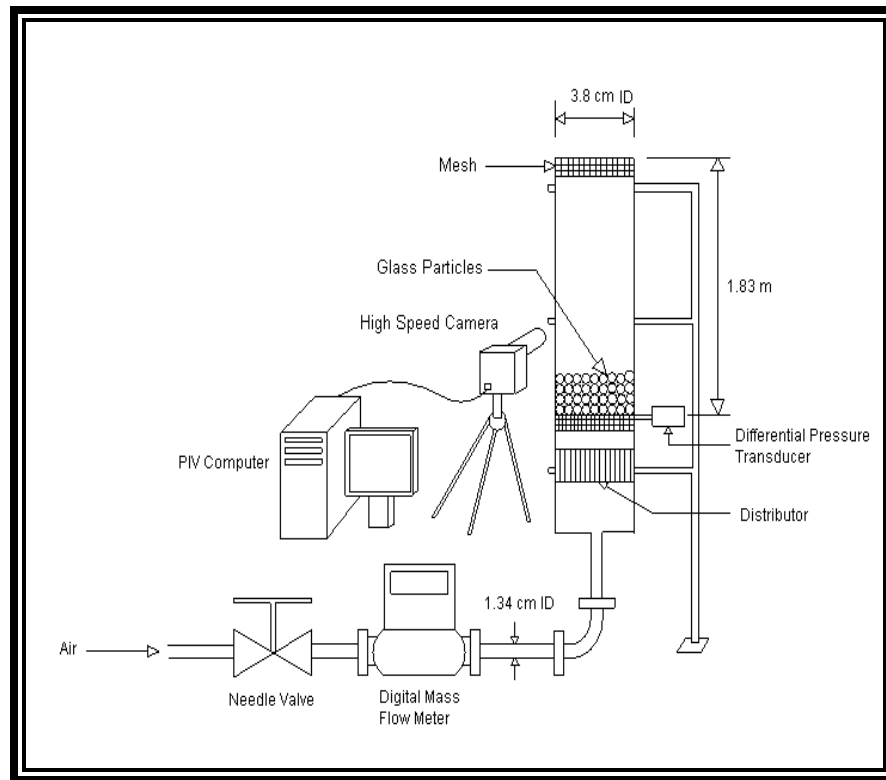


Figure 3.1: Schematic of the 1st generation fluidized bed

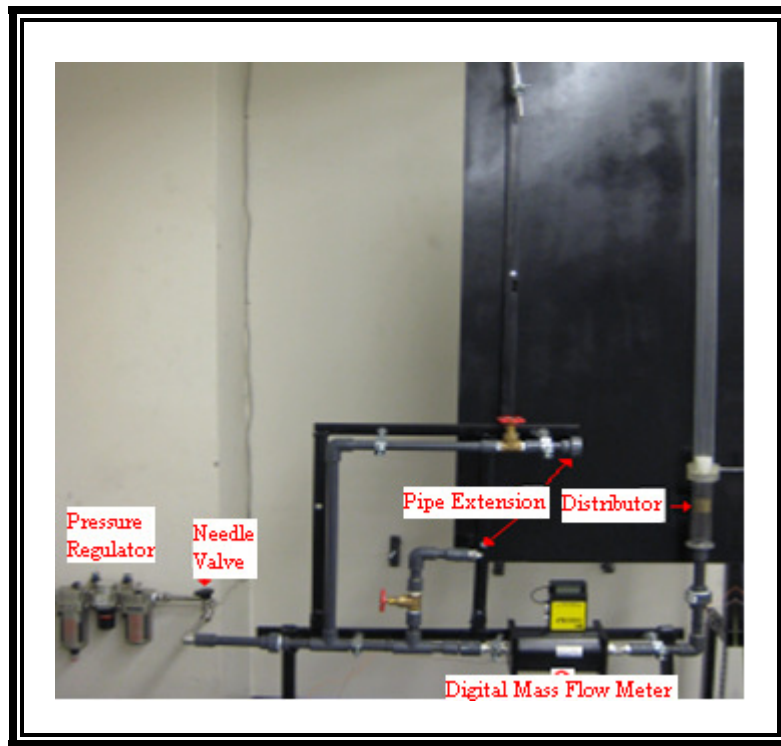


Figure 3.2: Experimental Setup of the 1st generation fluidized bed²¹

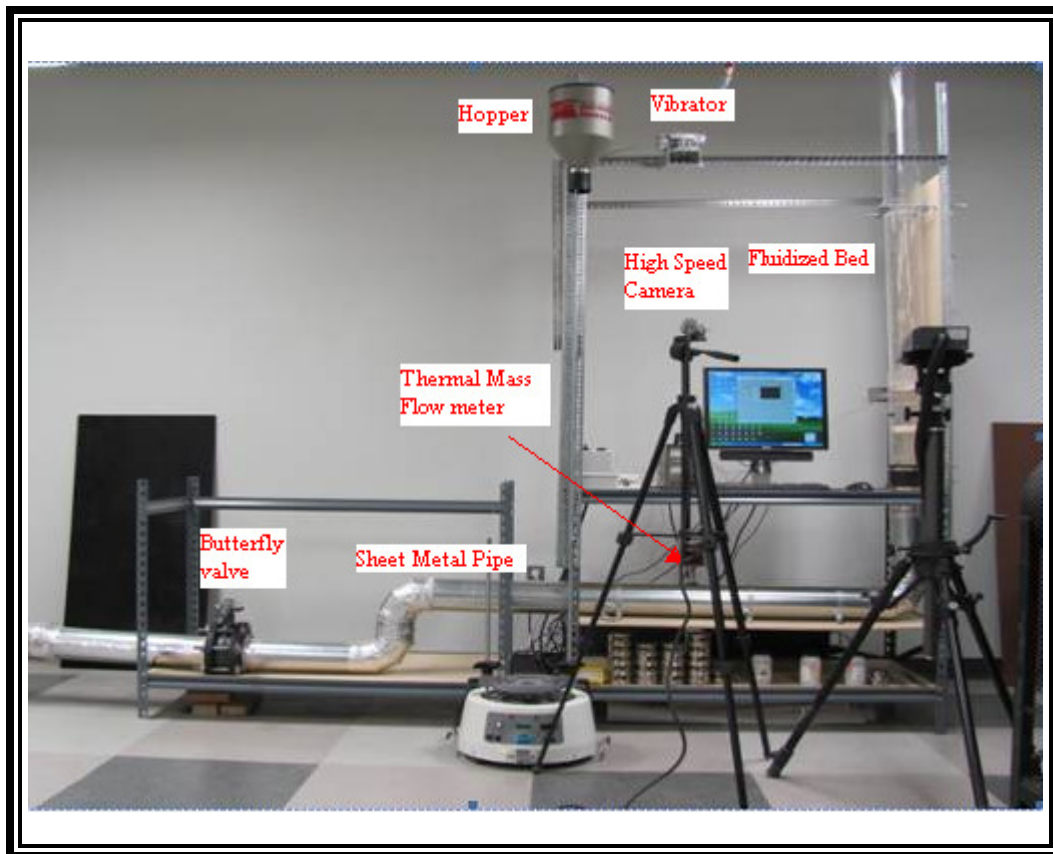


Figure 3.3: Experimental Setup of the 2nd generation fluidized bed

3.2 1ST GENERATION FLUIDIZED BED SYSTEM COMPONENTS

The 1st generation fluidized bed was built and tested to compare the effect of bed diameter on fluidization behavior of a bed, and to characterize the flow field and bed behavior of long shallow bed. The experimental apparatus used to achieve these goals are presented in the following sections.

3.2.1 Fluidized Bed Column

The 1st generation fluidized bed column was made of plexiglass tube with an outside diameter of 3.8 cm and a wall thickness of 0.318 cm. The tube was 183 cm in height.

3.2.2 Flow Straighter

Figure 3.5 presents a honeycomb shape distributor made of hexagonal brass tubes used in order to ensure the uniform flow within the column. Several 30.5 cm long brass tubes were cut into 2.5 cm length and glued together using Gorilla glue to prepare this distributor. This flow straighter was installed approximately 7.3 cm above the flow exit.

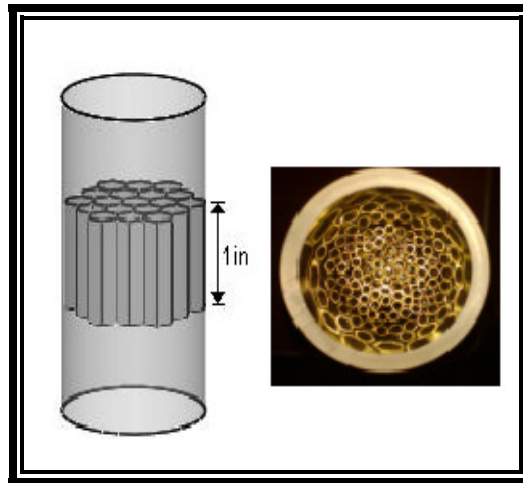


Figure 3.4: Honeycomb Shaped Distributor

3.2.3 Mesh Catch

A mesh catch made of brass screen with a nominal diameter of 0.425 mm was installed at the bottom of the bed and approximately at 7.32 cm above the distributor as shown in Figure 3.5 in order to prevent particles from falling back from the fluidized bed column. This screen was also used at the top

of the tube in order to prevent particles from being ejected out of the column at the fast fluidization regime.

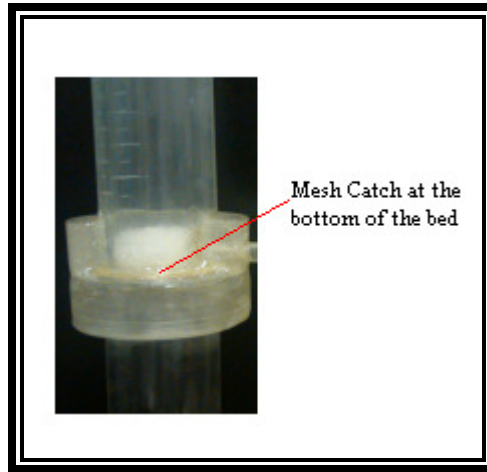


Figure 3.5: Mesh Catch

3.2.4 Compressor

For fluidization, air was supplied to the test section by a high pressure up to 125 PSIG, rotary type screw compressor having maximum discharge capacity of 97 CFM compressed air as shown in Figure 3.6.



Figure 3.6: Rotary Screw Air Compressor²¹

3.2.5 Fluid Supply System

The fluid delivery systems was comprised of Schedule 80 Polyvinyl Chloride (PVC) pipe with an inside diameter of 1.34 cm. All couplings and joints were securely glued with heavy duty PVC cement.

3.2.6 Needle valve

Figure 3.7 shows the 1/2 inch stainless steel integral bonnet needle valve with 0.73 coefficient of flow used to control the air flow to the test bed section. This valve includes Swagelok tube fittings with regulating stem.



Figure 3.7: SS Integral Bonnet Angle-Pattern Needle Valve³⁸

3.2.7 Digital Mass Flow Meter

To estimate the volumetric flow rate across the fluidized a digital mass flow meter was used. Figure 3.8 shows the linear type digital mass flow meter having 0 to 1000 SLPM flow range with 1.5 % FS accuracy.



Figure 3.8: Omega Digital Mass Flow Meter²¹

3.2.8 Pressure Regulator

Figure 3.9 shows a 0.05 to 0.85 MPa air filter, pressure regulator and lubricator. This regulator was used to maintain the line pressure of compressed air from the compressor at 0.28 MPa.



Figure 3.9: SMC AC40-N04C3-Z Air Filter, Pressure Regulator & Lubricator²¹

3.3 2ND GENERATION FLUIDIZED BED SYSTEM COMPONENTS

The 2nd generation fluidized bed was built and tested to compare the effect of bed diameter on fluidization behavior of a bed with the 1st generation bed, and to characterize the particle scale motion, to characterize the flow field and bed behavior with different flow regimes. The experimental apparatus used for this system are presented below.

3.3.1 Fluidized Bed Column

Figure 3.10 shows the column section from the experimental setup. The bottom section of the packed bed column was made of plexiglass tube with an outside diameter of 12.7 cm and a wall thickness of 0.318 cm. A quartz tube with an outside diameter of 12.0 cm and a wall thickness of 0.5 cm was inserted into the plexiglass tube section which is shown as the top part in Figure 3.10. The total tube height was approximately 183 cm. The quartz tube was used to attain a better optical access for the PIV analysis.



Figure 3.10: Fluidized Bed Section

3.3.2 Flow Straightener

The flow straightener used for this fluidized bed system was made of ABS plastic which was built in a rapid prototyping machine. Figure 3.1 shows the honeycomb shaped distributor located approximately 20.3 cm above the flow exit. The length of the distributor was 2.54 cm. Since, the blower is not a positive displacement type device; hence, to design this distributor the flow blockage ratio was determined so that it can resist the flow as less as possible. The blockage ratio (β) was found to be approximately 0.34, calculated using Eqn. (3.1). Here n is the total number of hexagons.

$$\beta = 1 - \frac{n \times \text{Cross sectional area of the hexagon}}{\text{Cross sectional area of the column}} \quad (3.1)$$

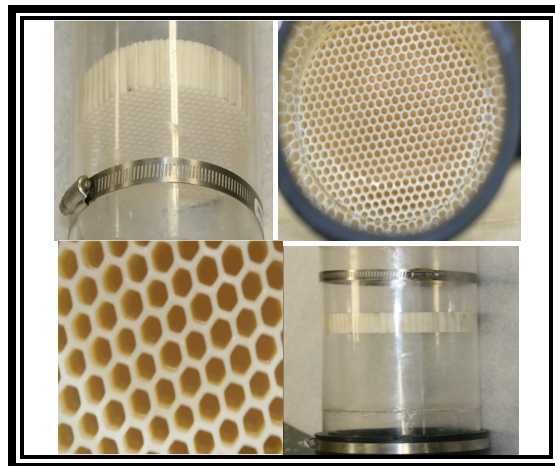


Figure 3.11: Flow distributor for 2nd generation bed

3.3.3 Mesh Catch

Figure 3.12 presents the mesh catch for the 2nd generation fluidized bed system with a nominal diameter of 0.053 mm which was installed about 25 cm above the flow exit from the piping. This was made from the brass screen. This mesh catch was also used at the top of the bed.

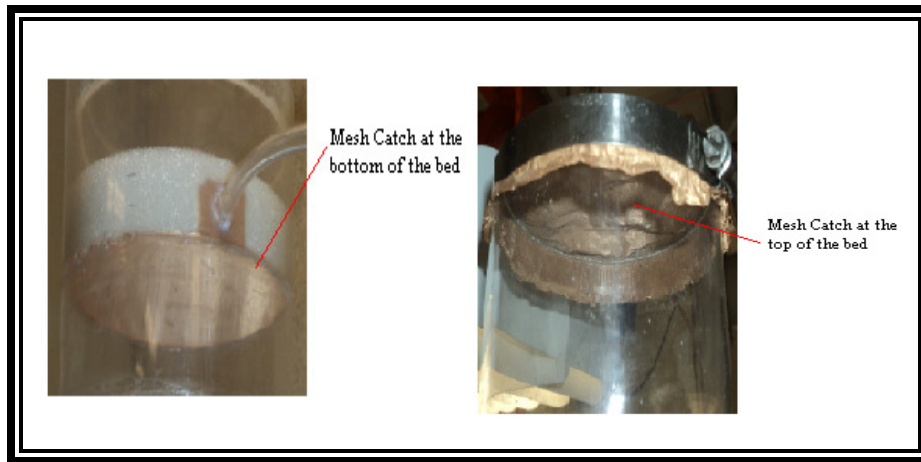


Figure 3.12: Mesh Catch for 12 cm Bed

3.3.4 Blower

Air was supplied to the bed section using a Grainger 5 HP high pressure blower with 1200 CFM air flow with 12 inch water column stagnation pressure shown in Figure 3.13. More information on the blower system can be found in Appendix B.

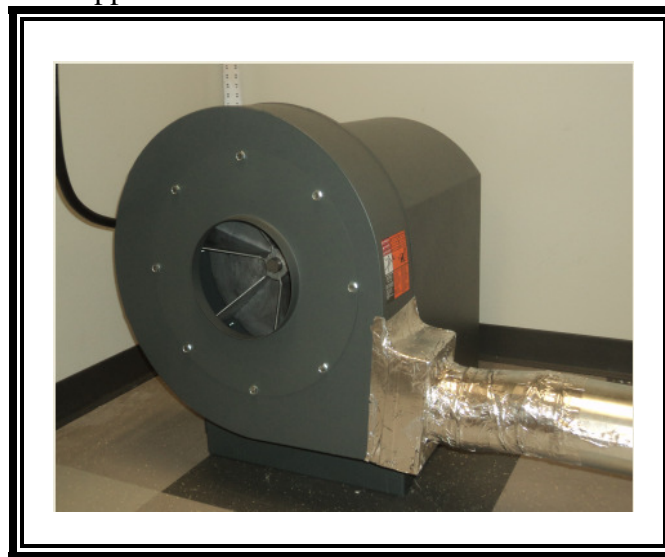


Figure 3.13: High Pressure Blower

3.3.5 Fluid Delivery System

The fluid delivery system was made from 12.7 cm diameter sheet metal pipe with three 90 degree elbows and a 12.7 × 17.8 cm rectangular to 10.2 cm duct reducer as shown in Figure 3.14. All joints were securely glued with high velocity duct sealant and on top of it duct tape. The complete pipe system was secured with saddles to resist from shaking at higher fluid velocities.

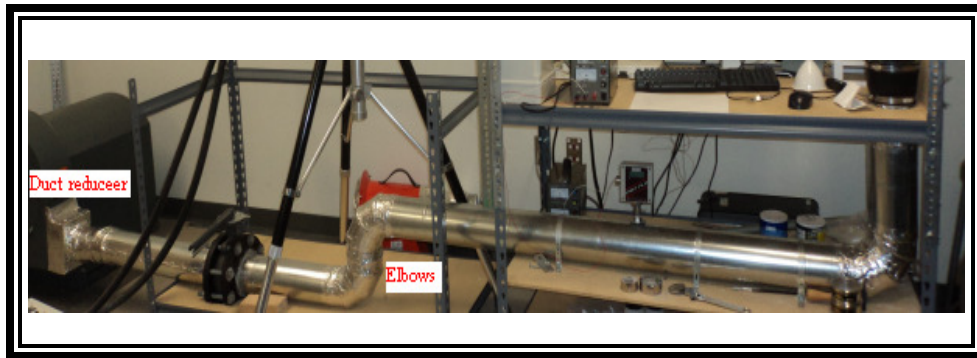


Figure 3.14: Fluid delivery system

3.3.6 Butterfly Valve

A 5 inch wafer style butterfly valve with 2 ¼ inch thick flange was chosen as the air flow controller for the other bed. The valve as shown in Figure 3.15 was made of cast iron with lever handle. It was rated for 200 PSI and a temperature range of -25 to 250 F.

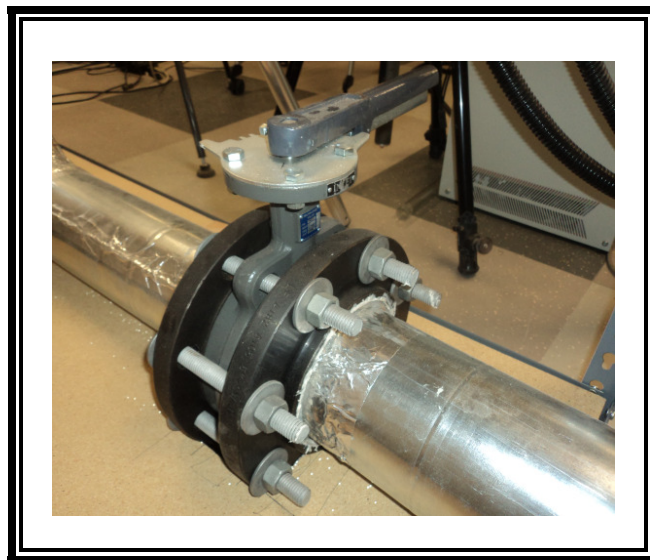


Figure 3.15: Wafer style butterfly valve

3.3.7 Thermal Mass Flow Meter

A smart insertion type high performance thermal mass flow meter with 200 millisecond response to change in flow rate, minimal flow blockage and low pressure drop and with a 2 ×12 backlit LCD display as shown in Figure 3.16 was used to estimate the volumetric flow rate across the bed. This flow meter was calibrated by the manufacturing company to the flow range of 0 to 4000 SLPM. A 20 VDC power using an external power supply was supplied to excite the flow meter as specified by the company.



Figure 3.16: Thermal Mass Flow Meter

3.4 PRESSURE MEASUREMENT

To estimate the pressure values a pressure transducer was used. Pressure drop across the bed for different gas superficial velocity was obtained from the DAQ as voltage output signals received from the differential pressure transducer. For each flow rate voltage output was measured at 100 Hz for twenty seconds and then the average of these voltage readings was taken. Pressure drop was determined from the correlation between the voltage output and the pressure rating provided by the transducer manufacturing company.

3.4.1 Differential Pressure Transducer

A six field-selectable differential with dust proof and splash proof enclosures shown in Figure 3.17 was used to estimate the pressure drop across the bed. It was connected to the bottom of the packed

bed with a tygon tube. A 53 micron mesh was used at the entry port of the tygon tube to restrain particles from entering into the tube.

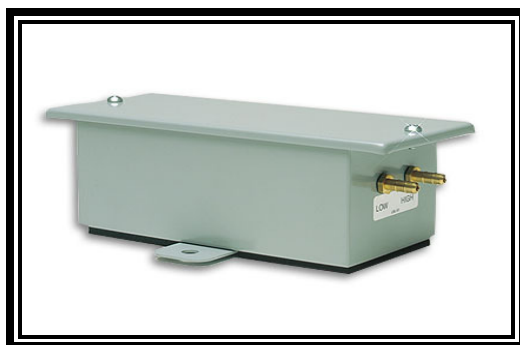


Figure 3.17: Omega PX277-30D5V Differential Pressure Transmitter

The wiring of the differential pressure transducer with the external power source and the data acquisition device is shown in Figure 3.19. The output configuration was set to unidirectional range with 0 to 5 VDC which resembles the pressure range of 0 to 3500 Pa as specified by the manual for this particular pressure transducer. The switch configuration for this output range is shown in Figure 3.20.

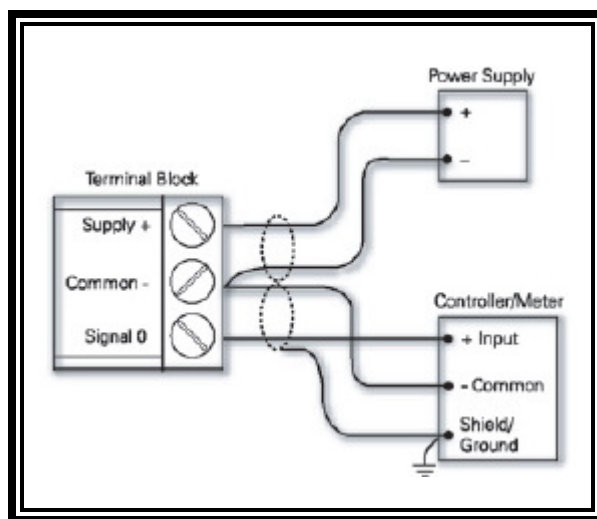


Figure 3.18: Wiring diagram for the pressure transducer³⁹

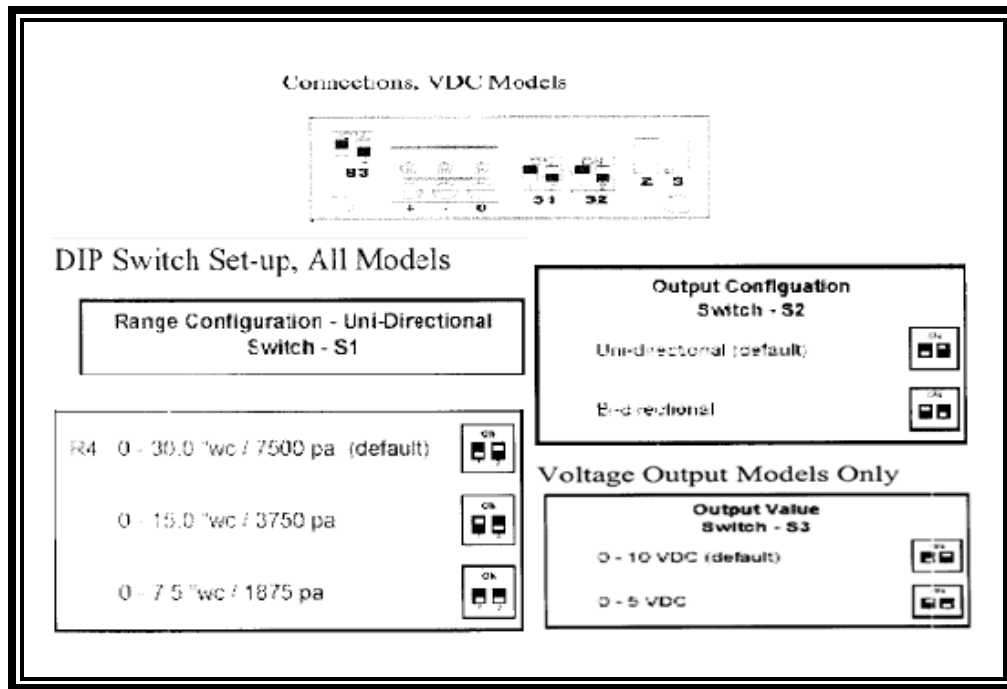


Figure 3.19: Switch configuration for the pressure transducer³⁹

3.4.2 External Power Supply

The 20 volt excitation power for the pressure transducer was supplied using an external power supply shown in Figure 3.18. This voltage was chosen by calibrating the transducer with respect to zero and maximum pressure output and then synchronizing the transducer at a point where the DAQ shows approximately zero voltage reading. The input power was selected from the range 12-40 volts specified by the manufacturer.



Figure 3.20: External Power Supply

3.5 DATA ACQUISITION

A data acquisition system was used for sampling signals to measure pressure drop from a differential pressure transducer and for converting the resulting signals into digital numeric values that was manipulated by the computer. The components of data acquisition system includes a sensor that converts physical parameters into electrical signals, a signal conditioning circuitry that converts electrical signals from the sensors into a form that can be converted into digital values, and an analog-to-digital converter that converts the conditioned electric signals into digital values.

3.5.1 Terminal Block

A National Instruments M series data acquisition device (DAQ) with SCC expansion slots and a 68 pin I/O connector was used to receive the voltage output signal from the differential pressure transducer. It was run in self powered mode. The terminal block used in this project is shown in Figure 3.21.



Figure 3.21: National Instruments Data Acquisition Device (DAQ)

3.5.2 LabVIEW

A National Instruments graphically programmed virtual instrument LabVIEW 8.2 that offers unrivaled integration with hardware devices and data visualization facility was used in this project to collect digital signals from the terminal block and to store it in the computer memory. The front panel and block diagram used in this project are shown in Figure 3.22.

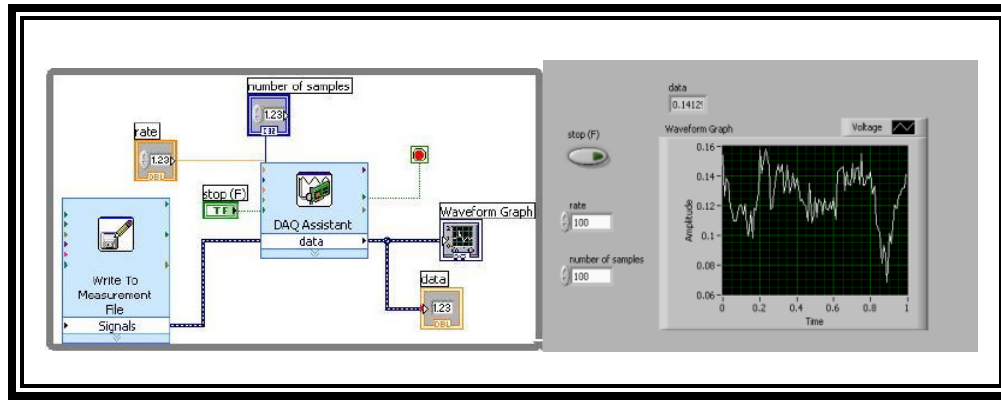


Figure 3.22: LabVIEW Virtual Instrument File

3.5.3 Digital Manometer

An Omega HHP 4252 digital display manometer (Figure 3.23) capable of measuring differential pressure and positive or negative gauge pressure was used to measure the bed pressure drop for the 2nd generation fluidized bed system. The accuracy of the manometer used was $\pm 0.3\%$ FS with a range of 0-2 psi. The results with this manometer were compared with the results from the differential pressure transducer also. This device was used because the resolution of it is 0.001 psi.



Figure 3.23: Omega HHP 4252 Digital Manometer

3.6 HIGH SPEED IMAGING

The particle behavior at the gas terminal velocity was captured using a Super 10K high speed camera (Figure 3.24) with 512×480 pixel CCD remote camera head to get a fundamental idea about the flow field of the particles with respect to fluid flow. 500 fps frame rate was used to capture these images. An example of these high speed imaging is presented in Figure 3.26. The minimum frame rate of this camera is 250 fps at full resolution 512×480 and its maximum frame rate is 10,000 fps.



Figure 3.24: FASTCAM Super 10K High Speed Camera

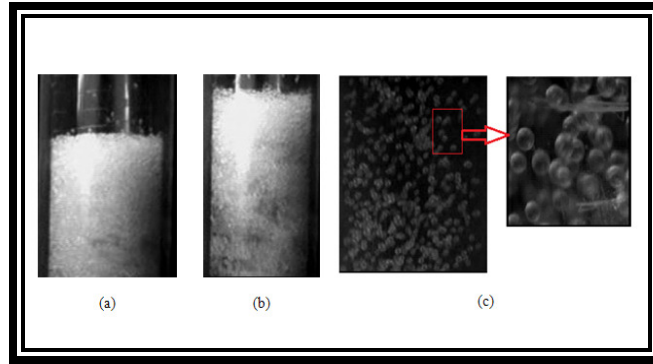


Figure 3.25: High speed particle motion captured at (a) minimum fluidization velocity, (b) transition and (c) full fluidization showing zoomed portion of the test section⁴⁰

3.7 MATPIV

The fundamental PIV analysis was performed using the MatPIV toolbox available to run with the MatLab. This technique uses the pattern matching technique from the images by creating a two dimensional plane. It then provides the flow field information such as velocity, vorticity, and streamlines. This analysis was applied to perform the flow field analysis of 1st generation fluidized bed. To attain these results several steps were followed from reading the images to finding the results.

3.7.1 Image Format

Two images at a time step of 1/500 sec was selected and stored for the PIV analysis. Since these images were in the RGB format and MatPIV works only with the intensity images, hence, the images were converted into the gray scale images. The MatPIV command to read these images and to change the image format is follows:

```
Image_1 = imread ('FILE NAME.FORMAT NAME')
```

```
Image_11 = rgb2gray (Image_1)
```

Figure 3.26 shows the pixel region of an image before image format changing and Figure 3.27 shows the pixel region of the image after the format change.

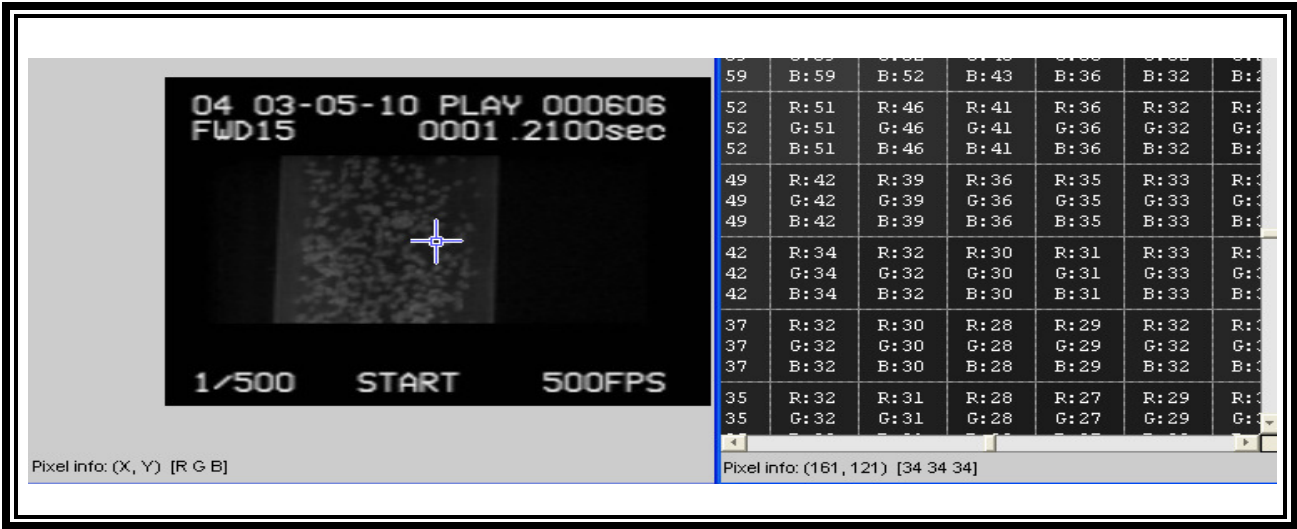


Figure 3.26: Pixel region of RGB image



Figure 3.27: Pixel region of Gray scale image

3.7.2 Image Contrast

The image contrast adjustment is required to get the particles detectable by the MatPIV software. The MatLab command for image contrast adjustment toolbar is:

```
Image_111 = imcontrast(Image_11)
```

The difference after the image contrast adjustment is illustrated in Figure 3.28 and Figure 3.29.

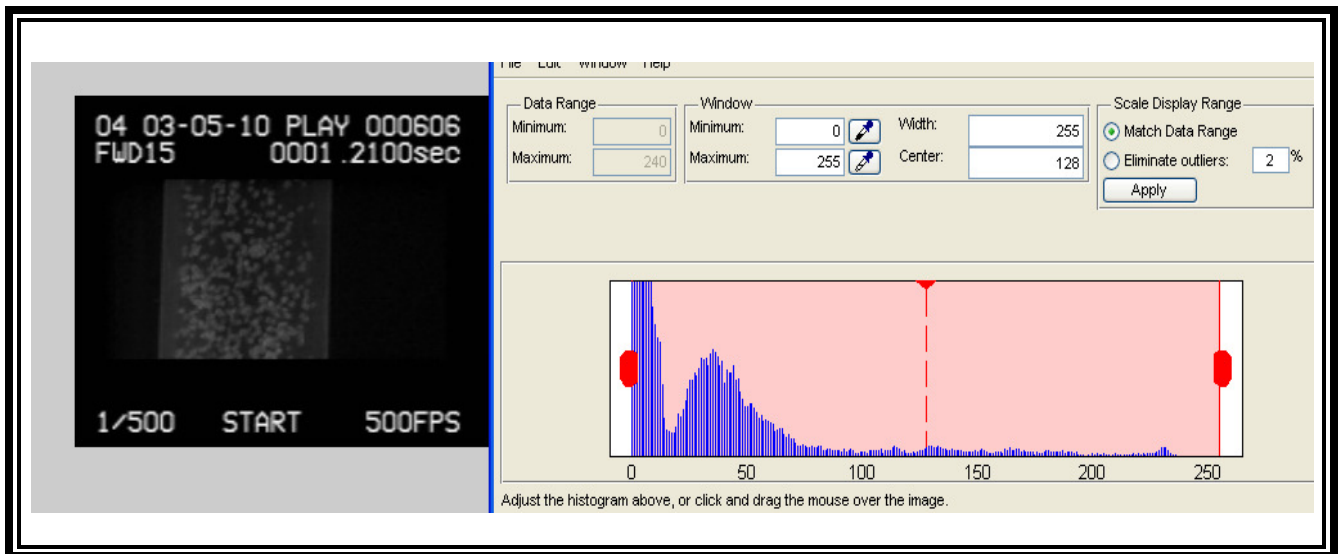


Figure 3.28: Gray scale image with initial contrast

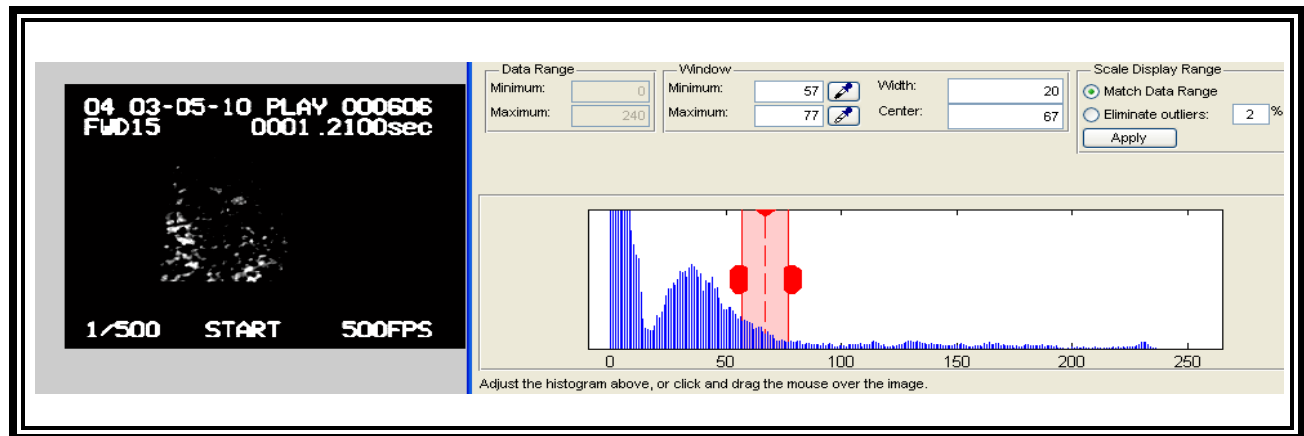


Figure 3.29: Gray scale image with final contrast

3.7.3 Coordinate System

To begin analyzing the images with the MatPIV, the first step is to transform the local camera coordinates to the physical world coordinates where the world coordinate might be defined by distinguishable dots or the regular grids. Figure 3.30 shows the regular grid used in this project where each dot is 1 cm apart. The command for the mapping of coordinate system is:

```
definewoco('frame.tif')
```

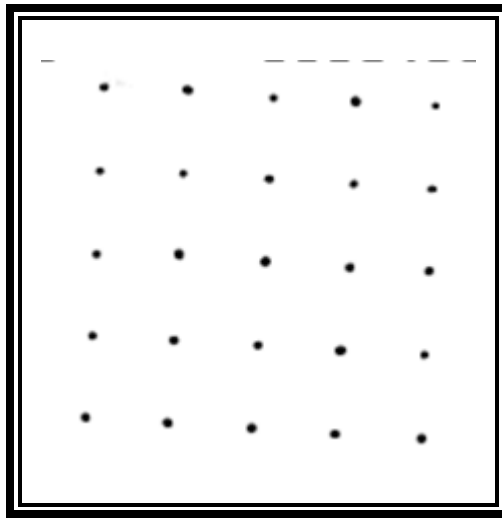


Figure 3.30: World Coordinate System

3.7.4 Image Masking

By defining a polygon in the image that should be excluded from the calculations, masking out a region of the flow is performed. It saves the calculation time. Figure 3.31 shows an image after masking. The Matlab command for this purpose:

```
mask('Image_111.tif','worldco.mat')
```

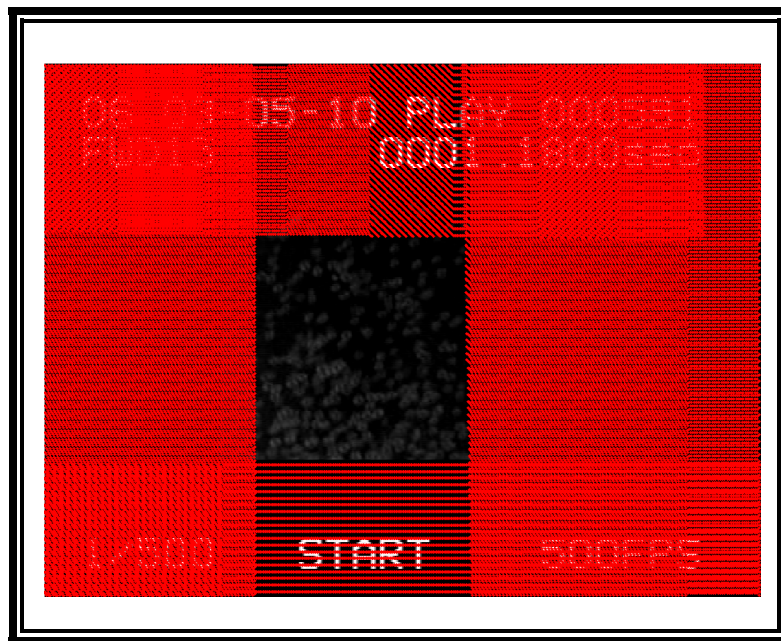


Figure 3.31: Masking out the region

3.7.5 Noise Filtering

In order to remove the so called spurious vectors from the velocity data, several filtering including signal-to-noise ratio, peak height, global filter and local filters are applied. The Matlab commands for these filtering are as follows:

```
[x,y,u,v,snr,pkh] = matpiv('Image_111.tif','Image_222.tif',[64 64;64 64;32 32;16 16;16 16],0.002,0.5,'multin','worldco.mat','polymask.mat')  
[su,sv] = snrfilt(x,y,u,v,snr,1.3)  
[pu,pv] = pkhfilt(x,y,su,sv,pkh,0.5)  
[gu,gv] = globfilt(x,y,pu,pv,3)  
[mu,mv] = localfilt(x,y,gu,gv,'median',3,'polymask.mat')  
[fu,fv] = naninterp(mu,mv,'linear','polymask.mat',x,y)
```

3.7.6 Integral and Differential Quantities

To calculate the velocity vectors, velocity magnitude, vorticity, streamlines, the following MatLab commands are used:

```
quiver(x(1:4:end),y(1:4:end),fu(1:4:end),fv(1:4:end), 2) ;axis tight  
quiver(x(1:1:end),y(1:1:end),fu(1:1:end),fv(1:1:end), 2) ;axis tight  
w = magnitude(x,y,gu,fv)  
polar(x,y,w), shading flat, colorbar  
W = vorticity(x,y,fu,fv,'circulation')  
pcolor(x(2:end-1),y(2:end-1),w), shading flat, colorbar  
h = streamline(x,y,fu,fv,2)
```

3.8 PIV (PARTICLE IMAGE VELOCIMETRY)

A Dantec Dynamics PIV system consisting of a 4 mJ 5 Amp laser with a synchronizer and a CCD camera system as shown in Figure 3.32 was used to obtain the instantaneous velocity measurements of test particles in the fluidized bed. An example of the captured images at 750 Hz frame rate is shown in Figure 3.33.



Figure 3.32: PIV System

To analyze the PIV data, Dynamic Studio provided by Dantec Dynamics V-3.14 was used. It includes different correlations for the PIV analysis. The images from the CCD camera were stored for the analysis and then after applying the auto correlation technique all the images were analyzed. From the analysis, the software performed, some statistical flow field information such as velocity vectors, average velocity, mean velocity, standard deviation, and correlation coefficient were obtained. This technique was applied for the 2nd generation particle scale motion analysis.

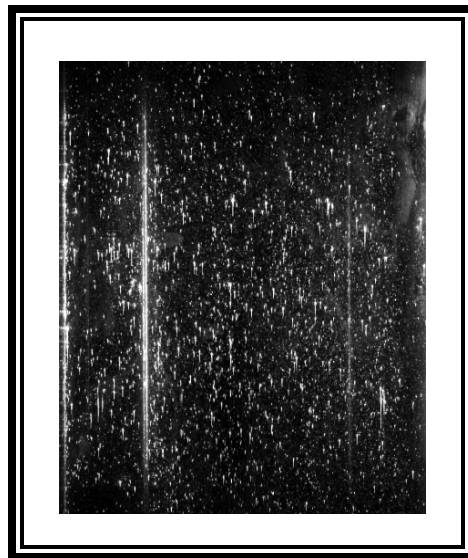


Figure 3.33: High speed image for PIV analysis

3.9 PARTICLE PRODUCTION

To produce the non-spherical test particles a compression machine and to analyze the size of the particles sieves were used. To measure the particle weight a precision balance was used.

3.9.1 Hydraulic Compressor

Figure 3.34 presents a CRAVER 3851 hydraulic compressor used to crush spherical particles into non-spherical particles at high pressure. The maximum capacity of the compressor is 24,000 pounds.

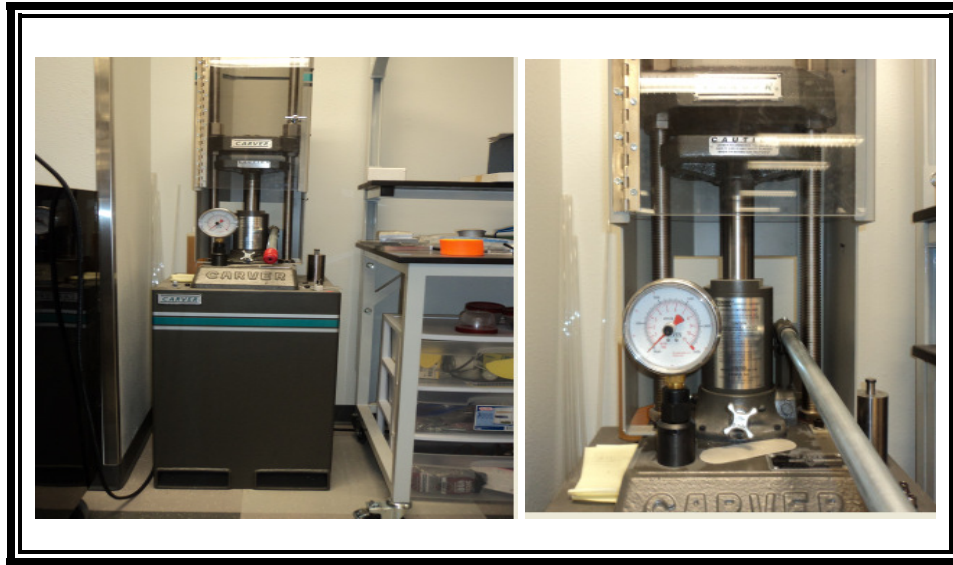


Figure 3.34: Hydraulic compressor

3.9.2 Die and Punch

A 2 inch diameter die and punch system was used to insert the spherical particles into the compressor to crush them. The die and the punch were made of stainless steel capable of withstanding high compression pressure. Figure 3.35 shows the die and punch used in this project.



Figure 3.35: Die and Punch

3.9.3 Precision Balance

Figure 3.36 presents the Mettler Toledo ML303E precision balance used to measure the particle weight with accuracy up to 0.001 gm.



Figure 3.36: Precision Balance

3.9.4 Sieve Shaker and Sieves

Figure 3.37 shows the Octagon Digital 110 volts, single phase, and 60 Hz frequency sieve shaker with sieves used to mount the sieves and shake them for obtaining particle size distribution. The sieve sizes used to determine the particle size are: 53, 63, 75, 90, 106, 125, 150, 355, 400, 500, 600, 710, and 850, 1180, and 2000 μm .

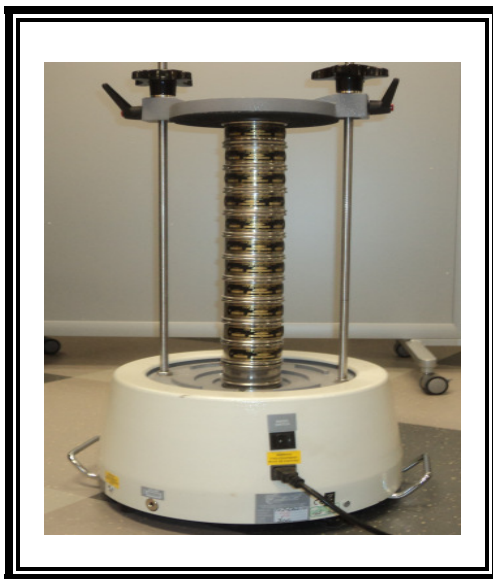


Figure 3.37: Sieve Shaker and Sieves

3.10 DRAG ANALYSIS

The drag coefficient analysis was performed for non-spherical particles with known sphericity for both single particles and multiple particles. Figure 3.38 shows the schematic of drag analyzing equipments.

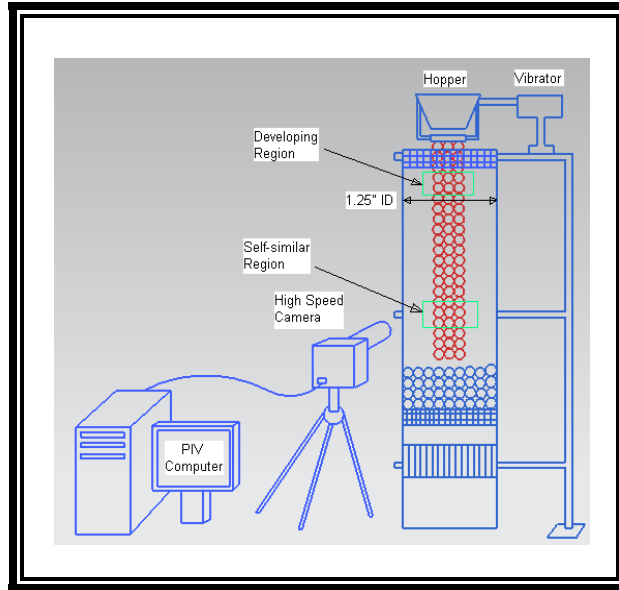


Figure 3.38: Schematic of drag analyzing equipments

3.10.1 Microscopic Video Camera

Sphericity of non-spherical particles plays an important role on the drag for of a free falling particle. A microscopic video camera was used to capture the particle images to obtain the particle nominal diameter for the sphericity analysis Figure 3.39 presents the microscopic video camera used for the sphericity analysis.



Figure 3.39: Dino Capture Microscopic Video Camera

3.10.2 Dino Capture Software

Dino Capture 2.0 was synchronized with microscopic video camera to analyze the particle diameters that are in micron scales.

3.10.3 Hopper

To introduce the drag test particles into the bed a 5600A overhead hopper made from stainless steel and having the maximum discharge height of 15 1/4 inches and capacity of 1/4 cubic feet was used. Figure 3.40 shows the hopper used for the current drag analysis.



Figure 3.40: Hopper

3.10.4 High Speed Camera

A Dantec Dynamics 5 kHz high speed camera Phantom (Figure 3.41) was used to capture the particle movement for the drag analysis.



Figure 3.41: Dantec High Speed Camera

3.10.5 Methodology

The initial terminal velocity achieved by the particles was calculated using Eqn. (3.2)⁴¹:

$$V_t = \sqrt{\frac{4 g d (\rho_s - \rho_f)}{3 \rho_f C_D}} \quad (3.2)$$

Where V_t is the terminal velocity, d is the mean diameter of the solid particles, ρ_s is the density of the solid particles, ρ_f is the density of fluid, and C_D is the drag coefficient.

The distance from top of the bed to the point where a particle is supposed to reach the terminal velocity was calculated using Eqn. (3.3) where H is the distance traveled by a single free falling particle.

$$H = \frac{V_t^2}{2 g} \quad (3.3)$$

The particles were introduced into the bed through a hopper mounted above the bed. The 500 KHz camera was used to capture the particle motion in the free falling stream using 3100 fps frame rate. Figure 3.42 shows the vertical motion and Figure 3.43 shows the horizontal and inclined motion of a single rice grain captured using the high speed camera. Using the phantom software the starting and ending point of the free falling particles in the camera frame and the time required to travel that distance by a single particle were determined.

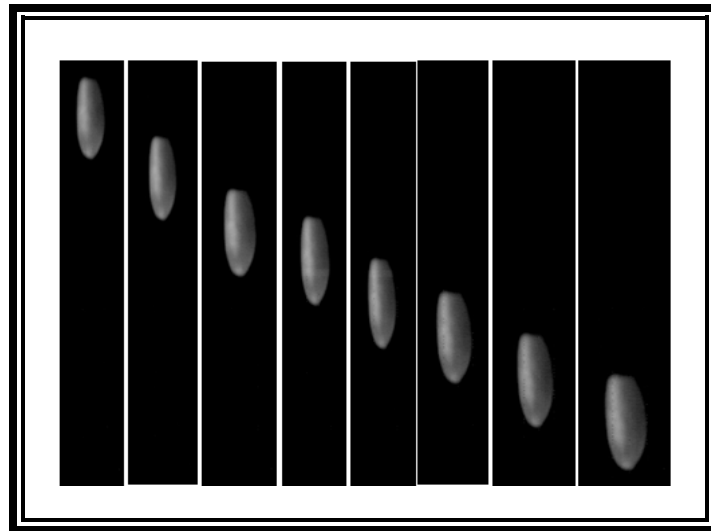


Figure 3.42: Vertical motion of a single free falling rice grain

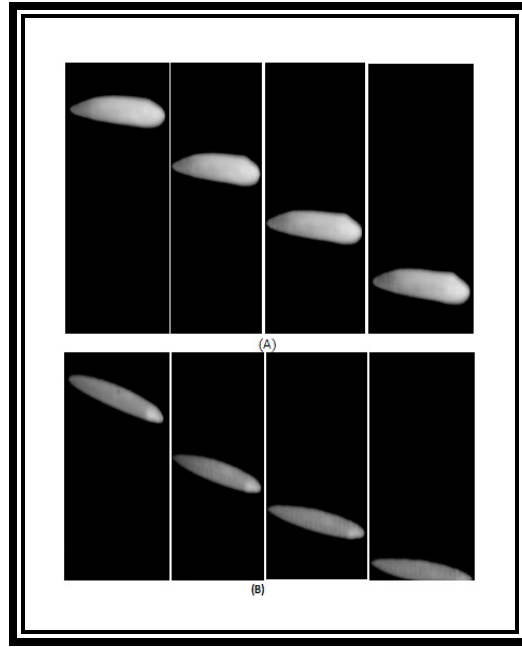


Figure 3.43: (A) Horizontal motion and (B) Inclined motion of a free falling rice grain

The final particle terminal velocity was then obtained using Eqn. (3.4):

$$V_t = \frac{\Delta s}{\Delta t} \quad (3.4)$$

Where, Δs is the distance travelled and Δt is the time required.

Finally, the experimental drag coefficient was calculated using Eqn. (3.4) and then compared with Eqn. (2.19).

$$C_D = \frac{4}{3} \frac{g d (\rho_s - \rho_f)}{\rho_f V_t^2} \quad (3.5)$$

3.11 TEST MATRIX

To perform the experiments presented in this thesis, several initial objectives were completed which were:

1. To obtain bed behavior characterization with spherical and non-spherical particles for the 1st generation fluidized bed.
2. To design and develop the 2nd generation fluidized bed.
3. To perform the drag analysis for a single particle with known dimension and sphericity.

Table 3.1(a) shows the test matrix for pressure measurements and Table 3.1(b) presents the test matrix for drag analysis.

Table 3.1(a): Test Matrix (Pressure Measurement)

Fluidized Bed	Particle Size	Particle Shape	Bed Height (cm)	Measured Parameters
1 st generation bed	1 mm	Spherical	5	Volumetric flow rate, Bed pressure drop
	600-850 μm	Non-spherical	5	
2 nd generation bed	1 mm	Spherical	2, 2.5, 3, 3.5, 4, 5	
	150-2000 μm	Non-spherical	2, 2.5, 3	

Table 3.1(b): Test Matrix (Drag Measurement)

Particle Size (μm)	Particle Sphericity	Measured Parameters
500-600	0.51-0.55, 0.56-0.60, 0.61-0.65, 0.66-0.70	Terminal velocity, Drag coefficient
600-710	0.51-0.55, 0.56-0.60, 0.61-0.65, 0.66-0.70	
710-850	0.51-0.55, 0.56-0.60, 0.61-0.65, 0.66-0.70	
850-1180	0.51-0.55, 0.56-0.60, 0.61-0.65, 0.66-0.70	
1180-2000	0.51-0.55, 0.56-0.60, 0.61-0.65, 0.66-0.70	

3.12 INSTRUMENTS USED

Table 3.2 summarizes the instruments used for the current study.

Table 3.2: List of instruments used for the current study

Instruments	Manufacturer/Model No.
Air Filter, Pressure Regulator & Lubrication	SMC AC40-N043-Z
Air Compressor	INGERSOLL-RA ND SSR-EP25
Digital Mass Flow meter	Omega FMA 1845
High Speed Camera	PHOTRON FASTCAM-Super 10K
Power Supply	LOKO DPS-3050
Differential Pressure Transducer	Omega PX277-30D5V
Needle Valve	Swagelok SS-1RS8
Blower	Grainger 7AV38
Hydraulic compressor	CRAVER M3851-0
Sieve Shaker	Octagon Digital 6242-10
PIV Laser	Litron LPU450
High Speed Camera	Dantec Dynamics
Thermal mass flow meter	Sierra Instruments # 620S-L04-M1-M2()-EN2-V4-DD-0
Butterfly valve	Grainger Item # 1JBF9, MILWAUKEE Butterfly Valve
DAQ	National Instruments NI-SCC68
Precision balance	Mettler Toledo ML303E

3.13 OPERATING CONDITIONS

The experiment operating conditions are stated in Table 3.3

Table 3.3: Operating Conditions

Parameters	1 st generation bed	2 nd generation bed
Bed Diameter (OD)	3.8 cm	12 cm
Air flow rate range (lit/m)	0-200	0-3000
Ambient Temperature	295 K	295 K
Ambient Pressure	101 KPa	101 KPa

3.14 EXPERIMENTAL UNCERTAINTIES

The measurement accuracy results for the 2nd generation bed at 5 cm static bed height with 1 mm spherical particles without honeycomb are presented in Table 3.4. Table 3.5 shows the error analysis results for the 1st generation bed at a static bed height of 5 cm operated with spherical particles and Table 3.6 shows the results with non-spherical particles.

Table 3.4: Accuracy results for 2nd generation bed ($U_s = 1.73$ m/s)

Mean Pressure (Pa)	623.78 Pa	
Random Error (Pa)	11.28 Pa	1.81%
Bias Error (Pa)	37.5 Pa	6.01%
Total Error (Pa)	38.67 Pa	6.20%

Table 3.5: Accuracy results for 1st generation bed with spherical particles ($U_s = 0.89$ m/s)

Mean Pressure (Pa)	627.02 Pa	
Random Error (Pa)	7.07 Pa	1.13%
Bias Error (Pa)	37.5 Pa	5.98%
Total Error (Pa)	38.16 Pa	6.09%

Table 3.6: Accuracy results for 1st generation bed with non-spherical particles ($U_s = 0.92$ m/s)

Mean Pressure	486.60 Pa	
Random Error	8.34 Pa	1.71%
Bias Error	37.5 Pa	7.71%
Total Error	38.42 Pa	7.89%

Chapter 4: Results and Discussions

This chapter focuses on presenting the experimental results to show the hydrodynamic behavior of a fluidized bed including the bed pressure drop with respect to gas superficial velocity, flow field vectors, particle scale motion, and different bed regimes. This chapter also includes the drag analysis results performed with non-spherical particles with known dimensions and known sphericity. The drag analysis results are shown for both single and multiple particles.

4.1 RESULTS FROM 1ST GENERATION FLUIDIZED BED

The 1st generation fluidized bed was analyzed initially to generate a fundamental idea of bed behavior, bed pressure drop, particle scale motion and was then applied to design and develop the 2nd generation fluidized bed. This section summarizes the results obtained from the 1st generation bed.

4.1.1 Results for Spherical Particles

The spherical particles (Figure 4.1) used for the 1st generation fluidized bed system were 1mm borosilicate glass beads with a sphericity variation of $\pm 10\%$ specified by the manufacturer and a density of 2230 kg/m^3 . Table 4.1 summarizes the physical properties of borosilicate glass particles. According to the Geldart classification of particles for air at ambient conditions (Fig. 2.11), the 1 mm spherical particles can be classified as Geldart group D. Here the gas density was used as the air density 1.21 kg/m^3 .



Figure 4.1: Spherical glass beads

Table 4.1: Physical properties of borosilicate glass particles⁴²

Physical Properties	
SiO ₂ = 80.6%	Coefficient of expansion (20°C–300°C) 3.3 x 10 ⁻⁶ K ⁻¹
B ₂ O ₃ = 13.0%	Density 2.23g/cm ³
Na ₂ O = 4.0%	Refractive index (Sodium D line) 1.474
Al ₂ O ₃ = 2.3%	Dielectric constant (1MHz, 20°C) 4.6
Optical Information	Specific heat (20°C) 750J/kg°C
Refractive index (Sodium D line) = 1.474	Thermal conductivity (20°C) 1.14W/m°C
Visible light transmission, 2mm thick glass = 92%	Poisson's Ratio (25°C – 400°C) 0.2
Visible light transmission, 5mm thick glass = 91%	Young's Modulus (25°C) 6400 kg/mm ²

Bed Pressure Drop

Each pressure drop value was calculated by averaging about 2000 readings for each flow rate. This volumetric flow rate was converted to gas superficial velocity using Eqn. (2.7). The mean pressure obtained for each flow rate was then used to map the differential pressure drop vs. superficial gas velocity. Figure 4.2 presents the bed pressure drop curve at a static bed height of 5 cm operated with spherical particles.

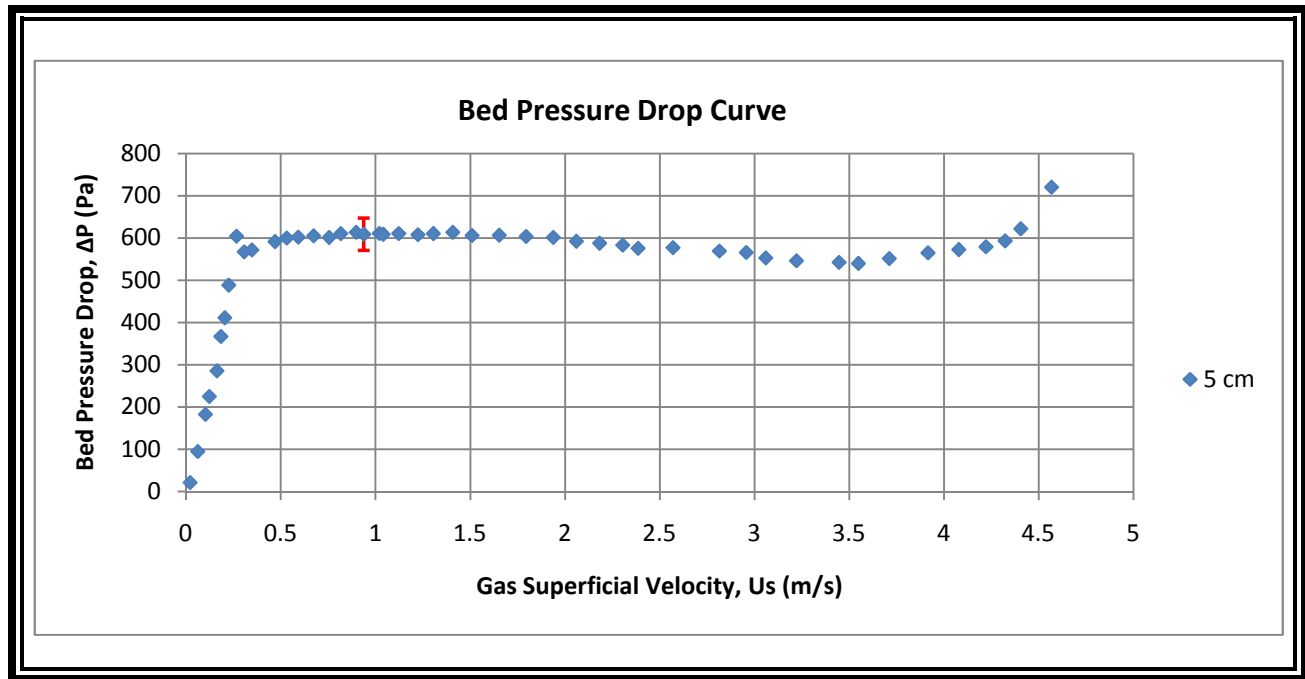


Figure 4.2: Bed (1st Gen) performance curve with spherical particles

A small hump just after the minimum fluidization can be observed in this graph. This may result from the interlocking of particles.

Non-uniform or aggregative fluidization with large bubbling can be observed at higher gas superficial velocity. Since in long, narrow fluidized beds, bubbles coalesce and try to cover the entire cross-section of the column, the slug of fluidized solid particles collapse the slug of gas and causes the solid particles fall back. This behavior of bed causes the non-uniform fluidization of particles i.e., larger fluctuations in pressure drop at higher superficial velocities⁴³.

MatPIV Results

Two images from the Super 10K high speed camera were selected at a time step of 0.002 second at the gas terminal velocity and then were analyzed with a MatPIV algorithm to obtain the flow field vector. The images after the image formatting and adjusting the contrast are presented in Figure 4.3.

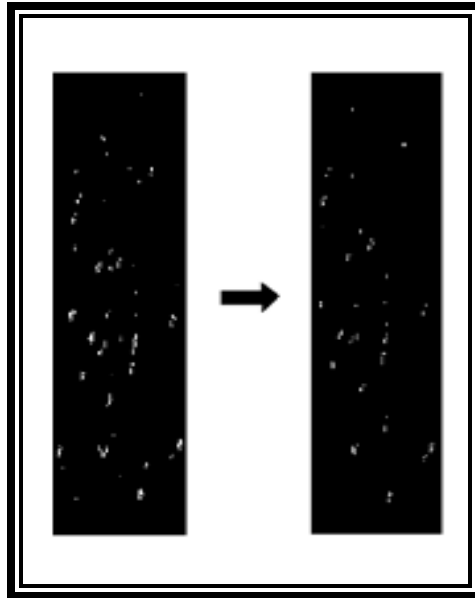


Figure 4.3: Images for MatPIV analysis for spherical Particles

Figure 4.4 shows the filtered and interpolated flow field vectors. Since it is difficult to trace the particle movement in a 3D plane, hence, the missing vectors were replaced using a nearest neighbor interpolation by the MatPIV⁴⁴. Magnitude of velocities in this flow field is presented in Figure 4.5 for spherical particles.

It can be seen from the figures that most of the spherical particles are in the velocity range of 0 to 40 cm/s. Vorticity magnitude is also presented in Figure 4.6.

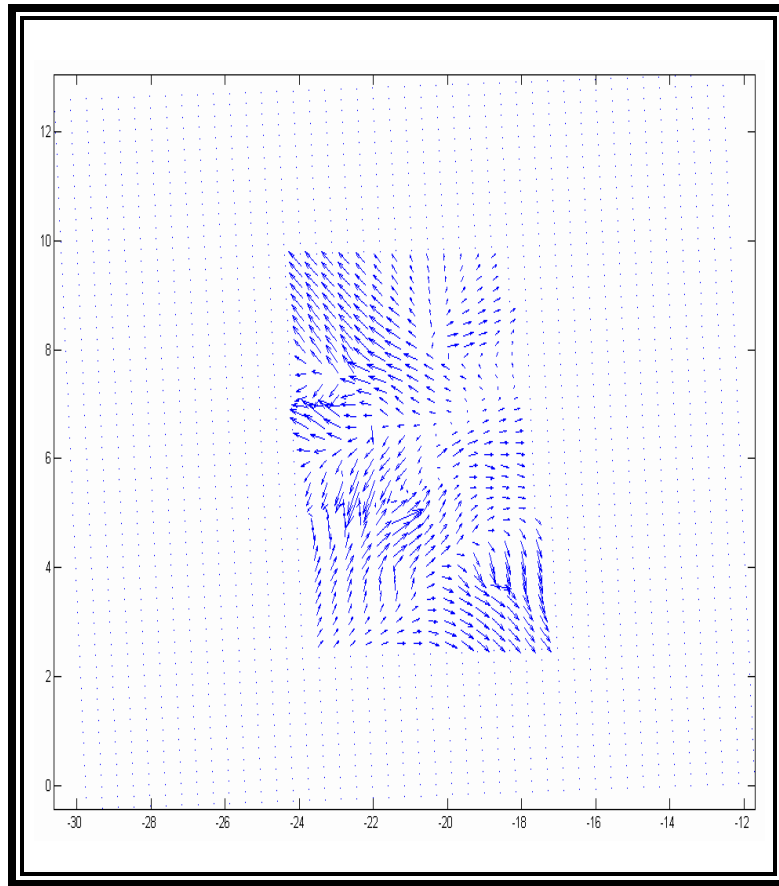


Figure 4.4: Instantaneous flow field vector with spherical particles (1st Gen.)

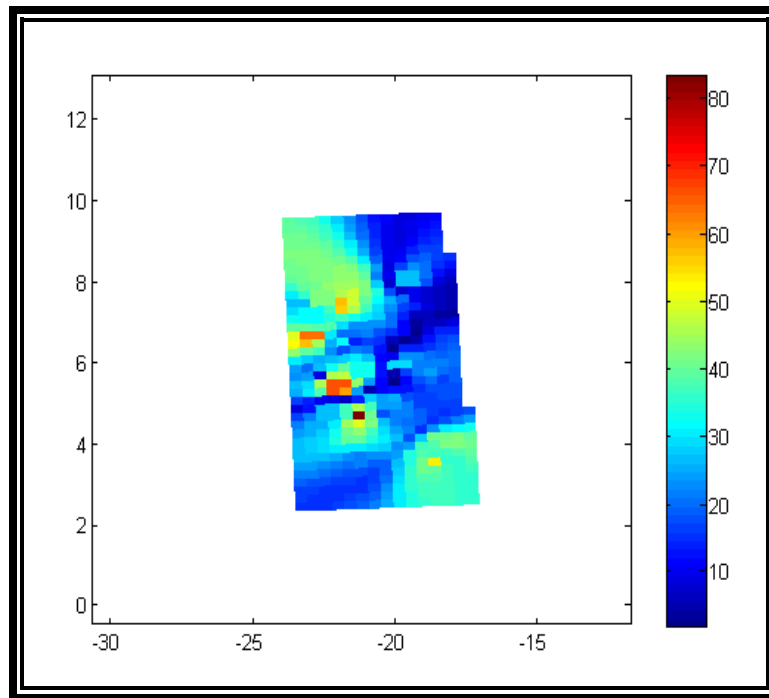


Figure 4.5: Instantaneous velocity magnitude with spherical particles (1st Gen.)

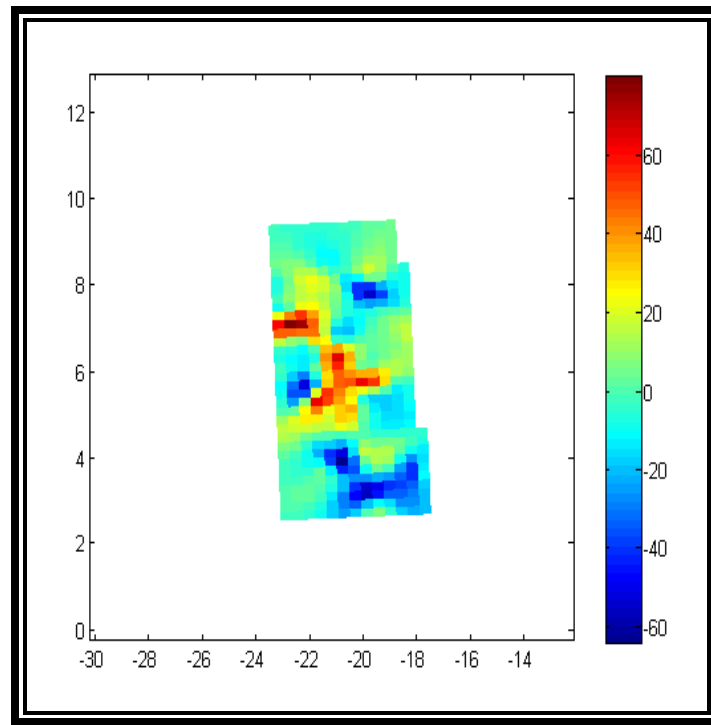


Figure 4.6: Instantaneous vorticity with spherical particles (1st Gen.)

Bed Behavior

Figure 4.7 shows the bed expansion with a static bed height of 5 cm at minimum fluidization velocity for spherical particles accompanied by channeling at the sides of the bed.

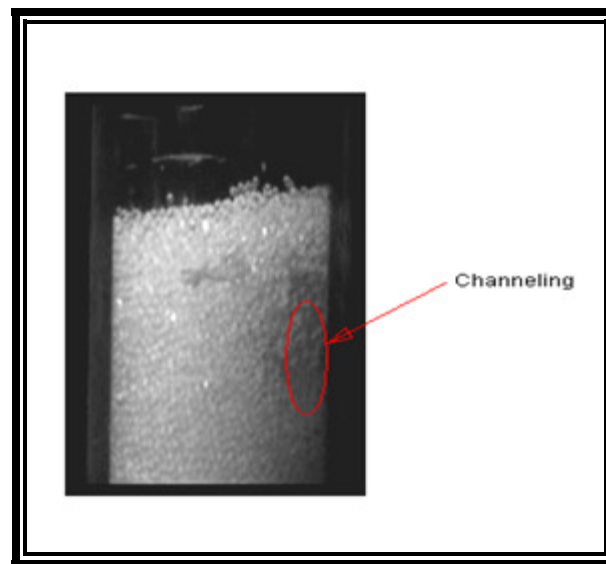


Figure 4.7: Bed expansion at U_{mf} with channeling (spherical particles)

As the superficial gas velocity is increased, bubble grows bigger and spreads throughout the bed. On the other hand, the particles due to gravity interact with the up going bubbles and hence, the bubbles collapse. For this reason fluctuations in the pressure drop from minimum fluidization to full fluidization region are observed. An example of this effect at higher gas velocity is presented in Figure 4.8. This also causes non-uniform distribution of fluid which results localized defluidization and particle agglomeration.

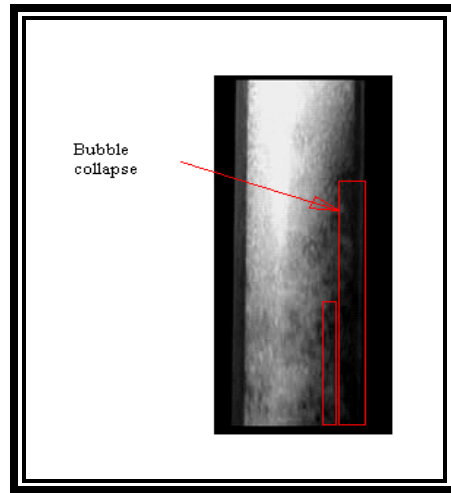


Figure 4.8: Bubble collapse for spherical particles

4.1.2 Results for Non-Spherical Particles

The non-spherical particles were obtained by crushing the 6 mm borosilicate glass beads using the hydraulic compression machine as mentioned earlier. Figure 4.9 shows the magnified image of non-spherical particles used for the experiments.

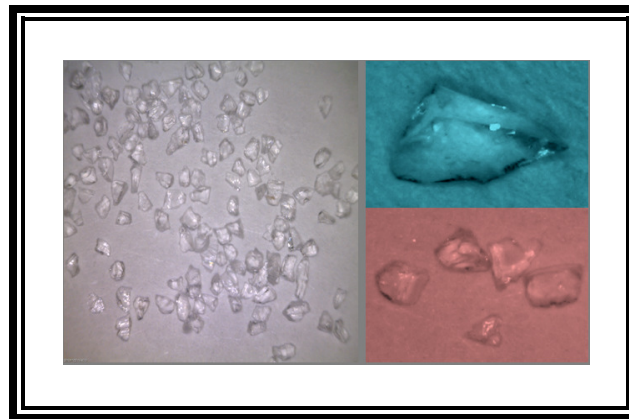


Figure 4.9: Non-spherical glass particles

Since the non-spherical particles were produced by crushing the 6 mm spherical borosilicate glass beads, hence, the non-spherical particle properties were also used as those for spherical glass beads for all the calculations. According to the Geldart classification of particles for air at ambient conditions (Fig. 2.11), the non-spherical particles can be classified as Geldart group D.

Particle Size

To obtain the particle size distribution for non-spherical particles, sieve test technique was applied. Figure 4.10 presents the sieve test results for non-spherical particle size distribution. It can be mentioned from the sieve test analysis results that the non-spherical particles used in this experiment were in the range of 600-850 μm with mean particle size of 717 μm .

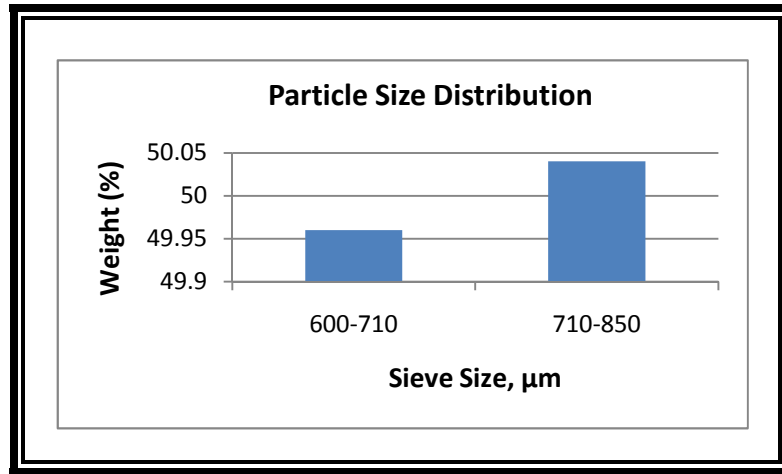


Figure 4.10: Particle size distribution

The mean particle diameter was calculated from the following Eqn. (4.1):

$$\text{Mean Diameter} = \frac{\sum \text{Weight Percent} \times \text{Average Sieve Size}}{\sum \text{Weight Percent}} \quad (4.1)$$

Particle Sphericity

Sphericity analysis of non-spherical particles used for 3.8 cm bed was initially performed for a number of individual particles using Eqn. (4.2) as specified in Krumbein (1941) method⁴⁵.

$$\varphi = \sqrt[3]{\frac{b \cdot c}{a^2}} \quad (4.2)$$

Where Krumbein defined the volume of a particle in terms of a triaxial ellipsoid having three diameters a , b , and c , where, ' a ' is greater than ' b ' is greater than ' c '.

The particle sphericity was found in the range of 0.61 to 0.88.

Bed Pressure Drop

Figure 4.11 presents the bed pressure drop curve at static bed height of 5 cm operated with non-spherical particles. Since a fluidized bed, the distributor is designed considering the particles as spherical hence, for non-spherical particles, the hump showing the non-uniform fluidization is larger.

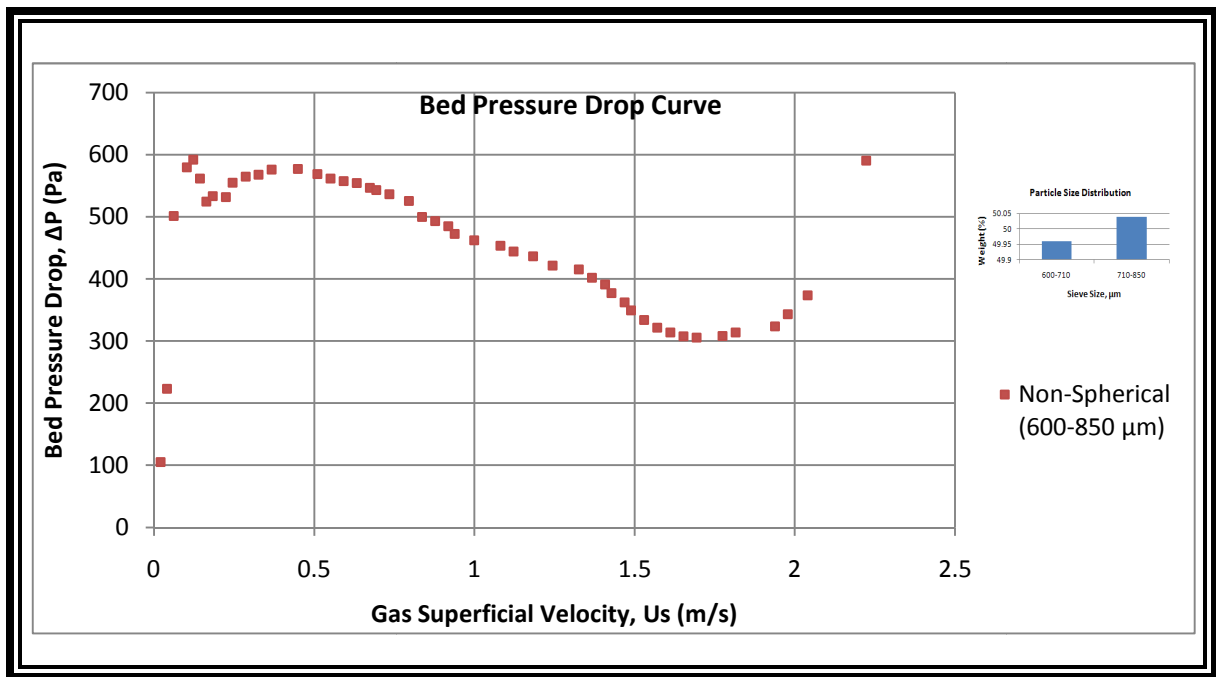


Figure 4.11: Bed (1st Gen) performance curve with non-spherical particles

MatPIV Results

Figure 4.12 shows two images after formatting selected to perform the MatPIV analysis at a time step of 0.002 sec. Flow field vectors are shown in Figure 4.13 and Figure 4.14 presents the velocity magnitudes with non-spherical particles. It can be seen from the figures that most of the non-spherical particles are in the range of 0-20 cm/s. Vorticity magnitudes are also presented in Figure 4.15.

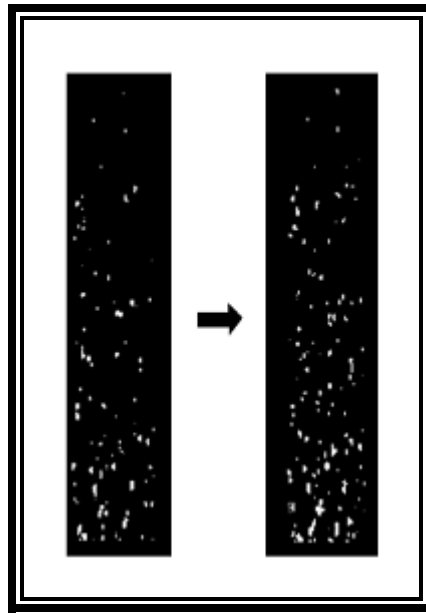


Figure 4.12: MatPIV images for non-spherical particles

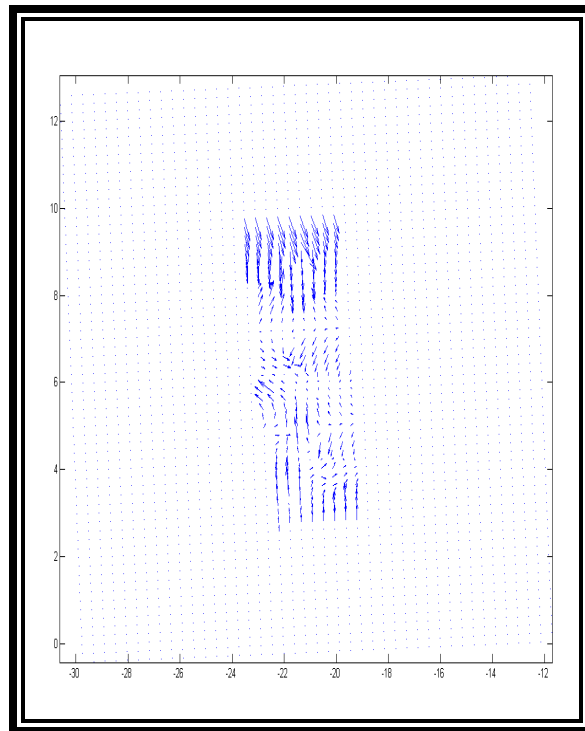


Figure 4.13: Instantaneous flow field vector with non-spherical particles (1st Gen.)

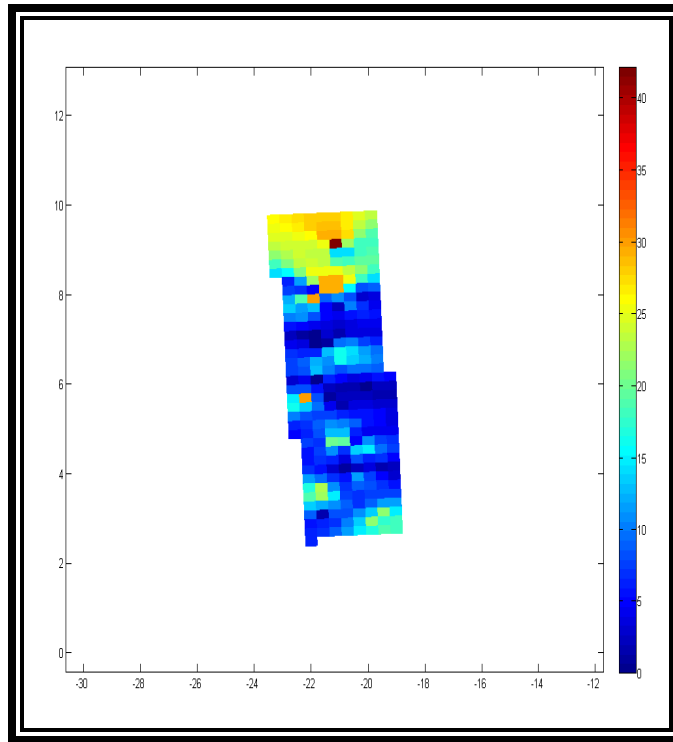


Figure 4.14: Instantaneous velocity magnitude with non-spherical particles (1st Gen.)

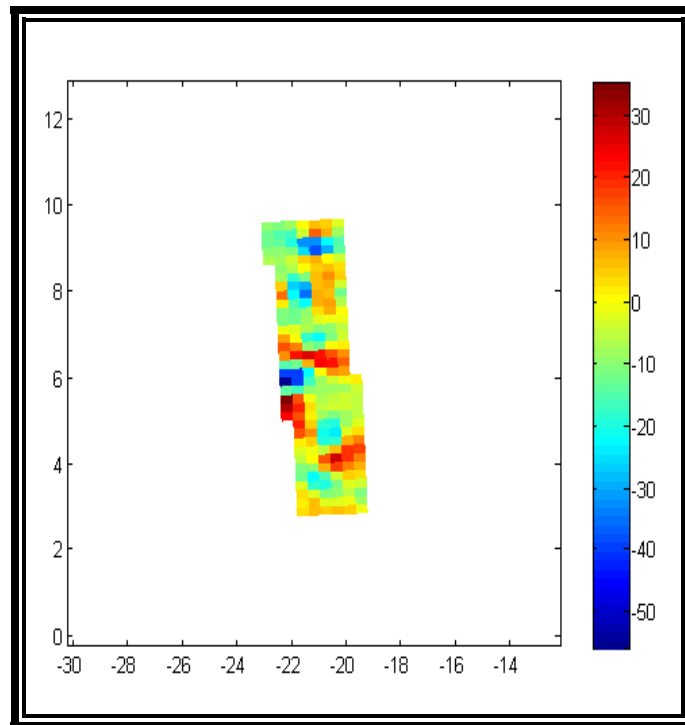


Figure 4.15: Instantaneous vorticity with non-spherical particles (1st Gen.)

Bed Behavior

Figure 4.16 shows the bed expansion of 1st generation fluidized bed with a static bed height of 5 cm at minimum fluidization velocity for non-spherical particles accompanied by channeling at the sides of the bed.

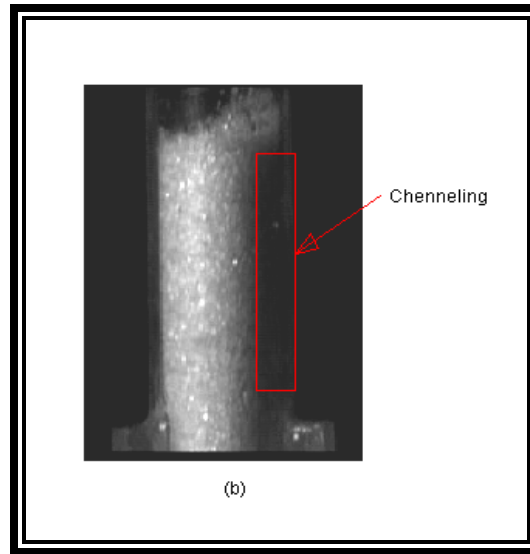


Figure 4.16: Bed expansion at U_{mf} with channeling non-spherical particles

It can be observed from the figure that the channeling for non-spherical particles is larger than that of the spherical particles as shown earlier when the particles start fluidizing. The bubble collapse at higher gas velocity is also shown in Figure 4.17. An electrostatic buildup, shown in Figure 4.18, due to less moisture content in the supplied air was also observed in this work.

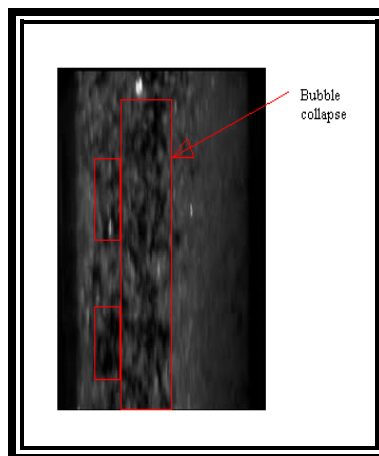


Figure 4.17: Bubble collapse for non-spherical particles

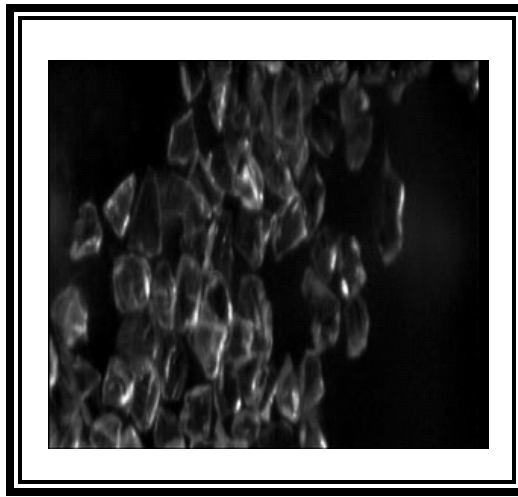


Figure 4.18: Particles stacked to the column due to electrostatic buildup

4.1.3 Effect of Particle Sphericity

Figure 4.19 presents the bed pressure drop curve for 1st generation bed at a static bed height of 5 cm operated with both spherical and non-spherical particles. From the graph it can be observed that the minimum fluidization and the full fluidization occur much earlier for the non-spherical particles than the spherical particles. This is due to the fact that the non-spherical particles are smaller in size and due to sphericity, these particles do not stack together to make a packed bed. Hence, larger non-uniform fluidization region is observed for the non-spherical particles.

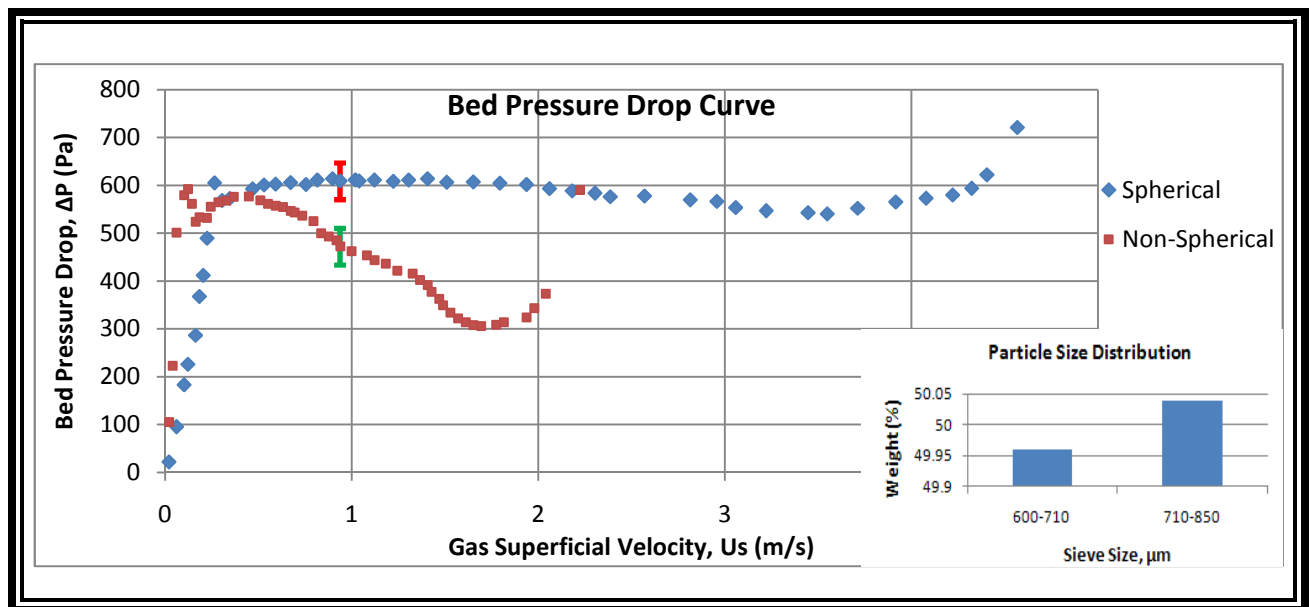


Figure 4.19: Bed (1st Gen) performance curve with spherical and non-spherical particles

4.1.4 Analytical and Experimental Pressure Drop Comparison

Experimental bed pressure drop at minimum fluidization velocity was validated by calculating the analytical pressure drop using the Eqn. (2.2). Table 4.2 shows the comparison between analytical and experimental pressure drop at minimum fluidization for both spherical and non-spherical particles.

Table 4.2: Analytical and Experimental pressure drop variance (1st Gen)

	Analytical Pressure Drop (Pa)	Experimental Pressure Drop (Pa)	% Deviation
Spherical Particles	682	605	11.3
Non-spherical particles	679	592	12.8

4.1.5 Analytical and Experimental U_{mf} Comparison

Minimum fluidization velocity was analytically determined by using Eqn. (2.10). The void fraction, sphericity, and particle diameter for spherical particles were set as 0.42, 0.9, and 1 mm respectively and respectively 0.42, 0.6, and 717.57 μm for non-spherical particles. Table 4.3 shows a comparison between analytical and experimental minimum fluidization velocity for 3.8 cm bed. Since the analytical U_{mf} derived from the Ergun equation never considers the bed height, hence, the analytical U_{mf} seems to be constant with respect to the bed heights which show deviation from the experimental results.

Table 4.3: Analytical and Experimental U_{mf} Variance (1st Gen)

	Analytical U_{mf} (m/s)	Experimental U_{mf} (m/s)
Spherical Particles	0.514	0.270
Non-spherical particles	0.173	0.120

4.2 RESULTS FROM 2ND GENERATION FLUIDIZED BED

Based on the results of 1st generation bed, the 2nd generation fluidized bed was designed and developed and then analyzed initially to generate the bed behavior, bed pressure drop, particle scale motion. This section summarizes the results obtained from the 2nd generation bed.

4.2.1 Results for Spherical Particles

The spherical particles used for this bed are the same as those used for the 1st generation bed, 1 mm borosilicate glass beads. The experimental results obtained for the 1st generation bed operated with spherical particles are presented in the following sections.

Bed Pressure Drop

Figure 4.20 presents the bed pressure drop curve at a static bed height of 5 cm operated with spherical glass beads where the results were obtained using the pressure transducer. From the graph it can be seen that the bed pressure drop keeps increasing after the minimum fluidization condition rather than remaining constant as specified in the literature. One reason for that might be the bed height. Since, a bed is designed for a specific static bed height, a specific type of flow distributor; hence, used bed height and the flow straighter might not be a better choice for this bed. This might have generated the non-uniform fluidization across the bed. Also, after the full fluidization, since, a mesh catch was used, particles were not able to escape from the bed, hence, the bed pressure drop keeps increasing after the maximum fluidization rather than decreasing as specified in the literature (Figure 2.16). To validate the results for the digital manometer, a comparative graph including the results with digital manometer and the pressure transducer is presented in this figure.

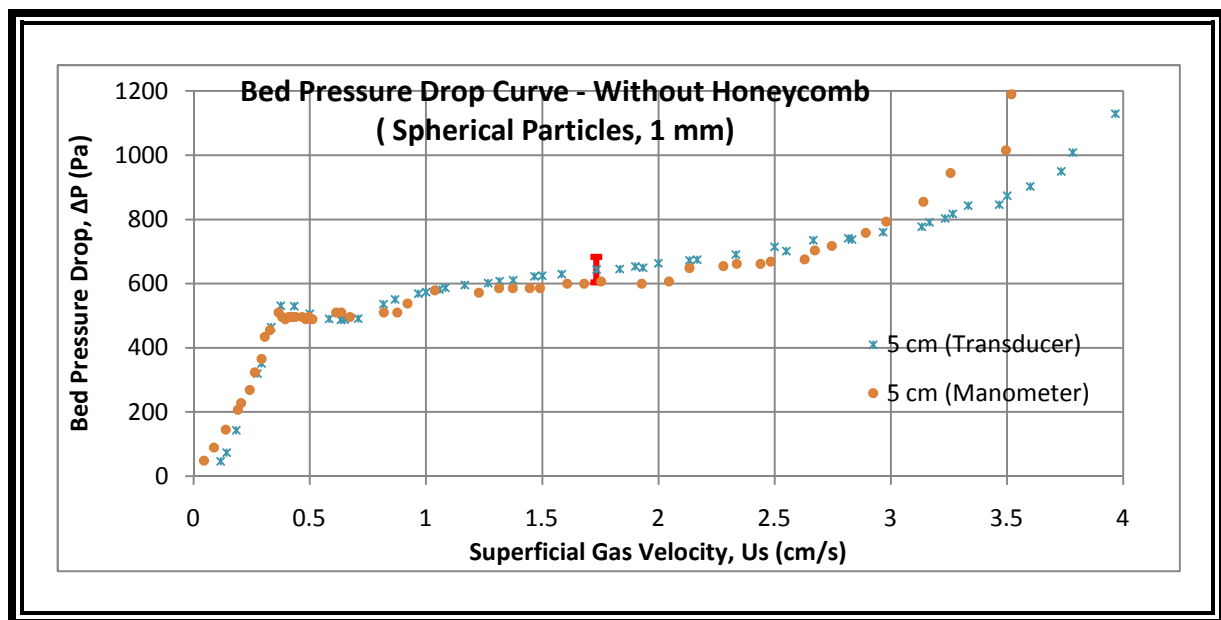


Figure 4.20: Bed (2nd Gen) performance curve with spherical particles

Effect of Bed Height

The bed performance curve for the 2nd generation bed operated with spherical particles at different bed heights without the flow straightener is shown in Figure 4.21. These results were taken with the digital manometer.

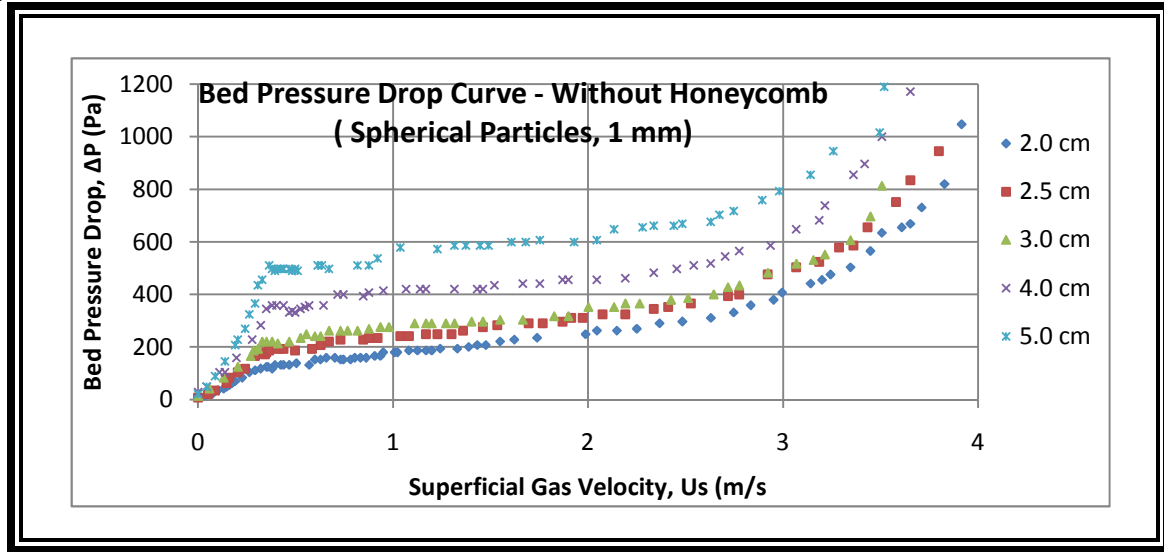


Figure 4.21: Bed (2nd Gen) performance curve at different bed heights (without honeycomb)

It can be seen from the graphs that the bed starts showing better performance after 3 cm bed height. Also, with increasing the bed height the pressure drop value increases. The rising section for each height is seen due to the mesh catch used at the top of the bed. Figure 4.22 presents the bed pressure drop curve using the honeycomb for spherical particles.

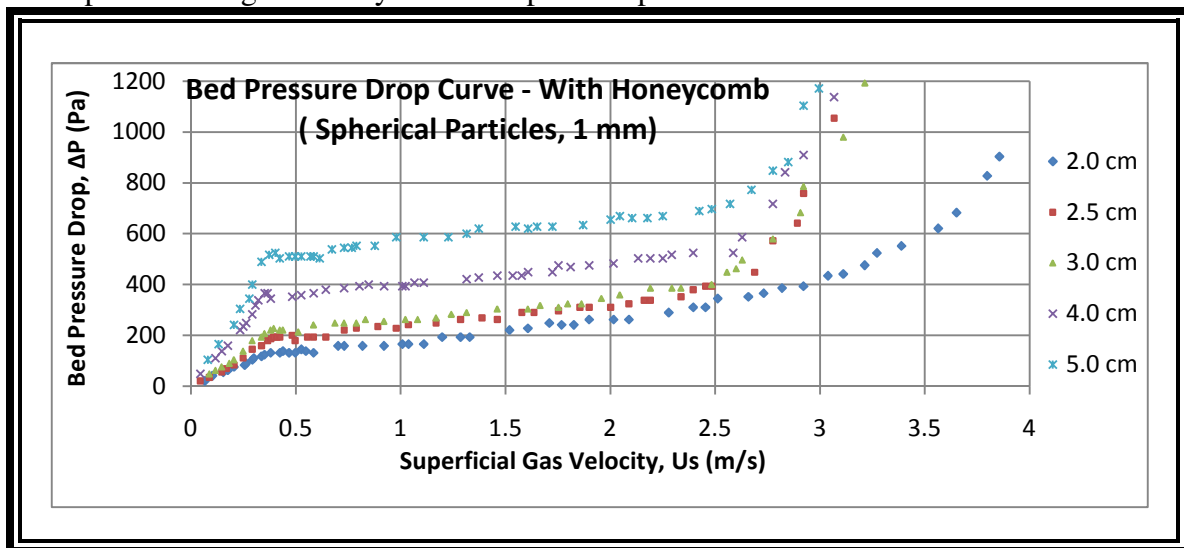


Figure 4.22: Bed (2nd Gen) performance curve at different bed heights (with honeycomb)

Effect of Flow Blockage Ratio

The effect of flow blockage ratio analysis was performed by running the experiments without using a flow straighter and with using a honeycomb shaped flow distributor. The bed pressure drop curves for the 2nd generation bed operated with spherical particles at different bed heights with and without using the honeycomb flow straightener are presented from Figure 4.23 to Figure 4.27. These results show that a slight difference in pressure drop is present in the bed which means the flow straightener was able to make the flow uniform a very small amount, especially after the minimum fluidization region. Ideally the flow straightener was supposed to make the flow uniform for which the bed pressure drop from the minimum fluidization region to the maximum fluidization region was supposed to be approximately constant. From these curves, it could be inferred that the flow straightener might required to be redesigned and repositioned to get better results. On the other hand the problem associated with the very fine honeycomb shaped flow straightener is that it might create huge pressure drop across its orifices for which the performance of the blower might get degraded. It might create a back pressure to the flow since the blower is not a positive displacement type machine. Hence, the flow distributor is supposed to be designed optimally. This thesis presents the results with only one distributor at only one position.

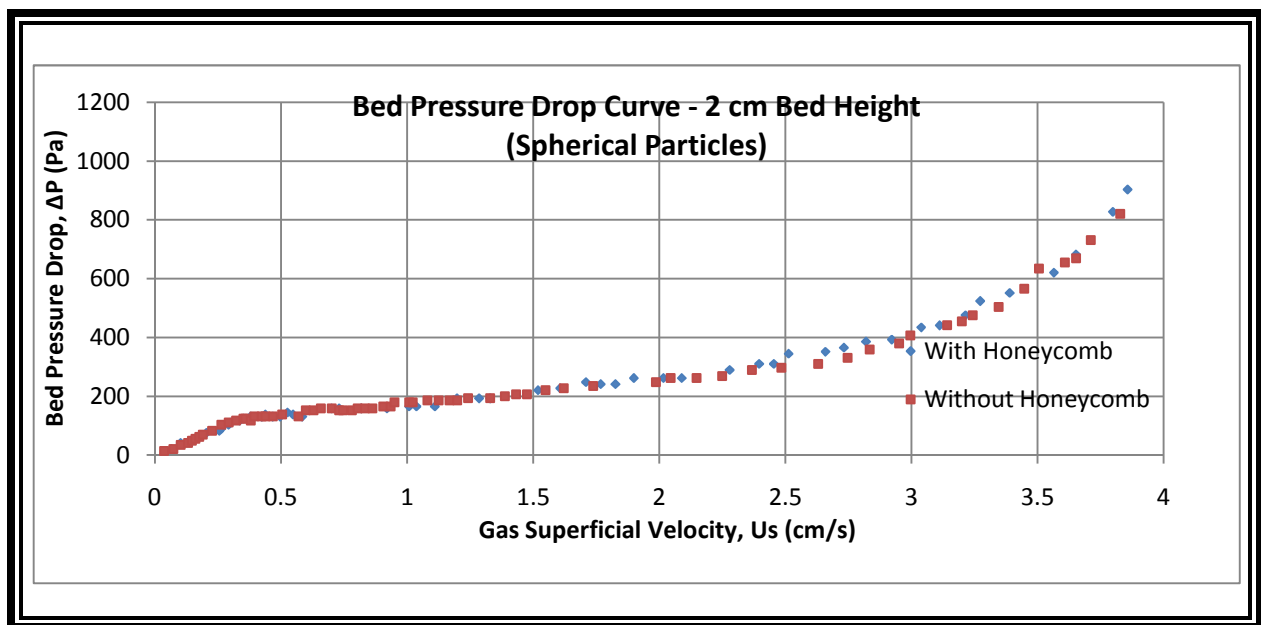


Figure 4.23: Bed (2nd Gen) performance curve with and without the honeycomb (2cm Bed)

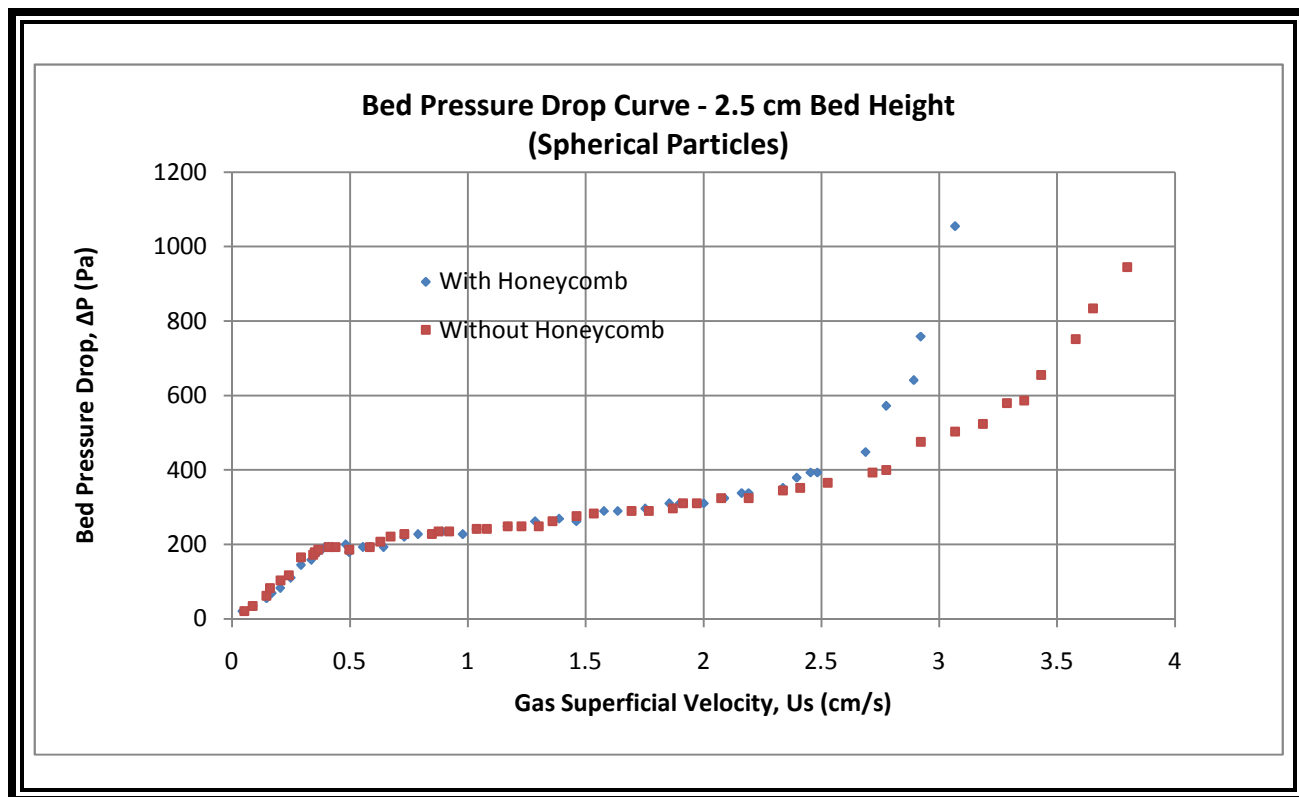


Figure 4.24: Bed (2nd Gen) performance curve with and without the honeycomb (2.5cm Bed)

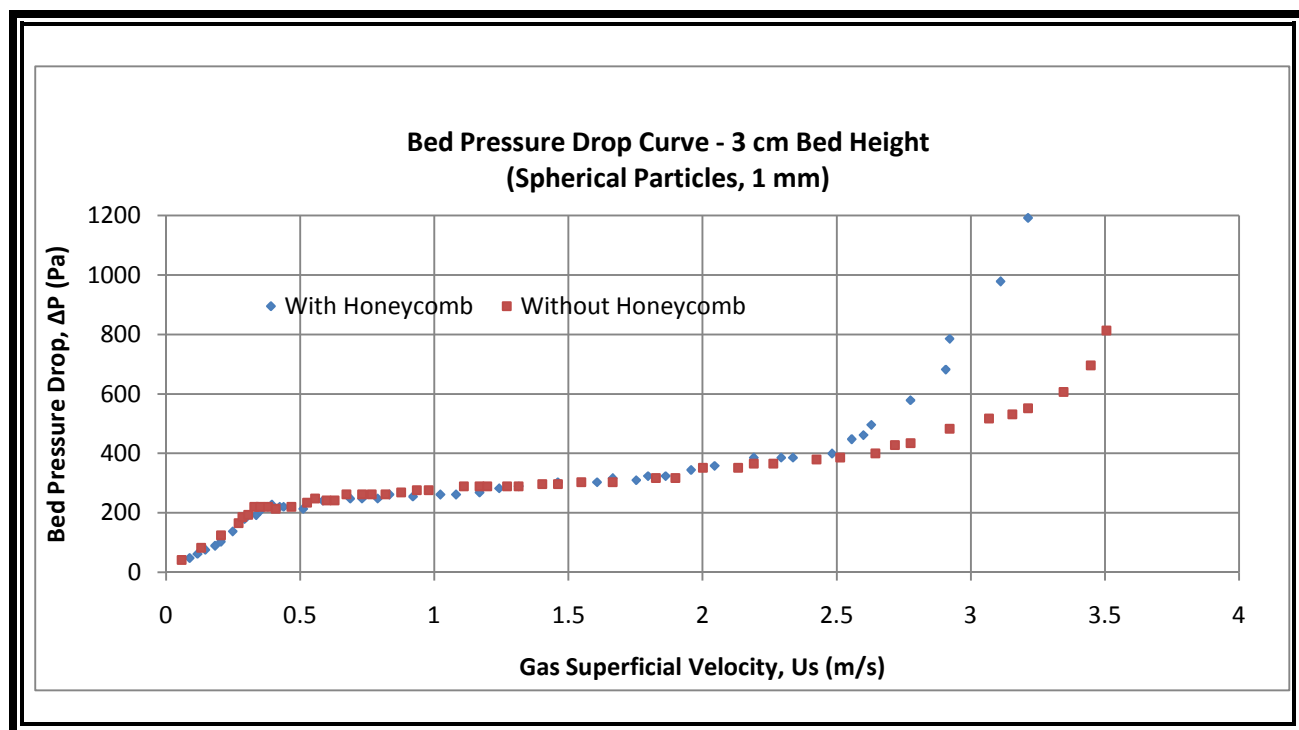


Figure 4.25: Bed (2nd Gen) performance curve with and without the honeycomb (3cm Bed)

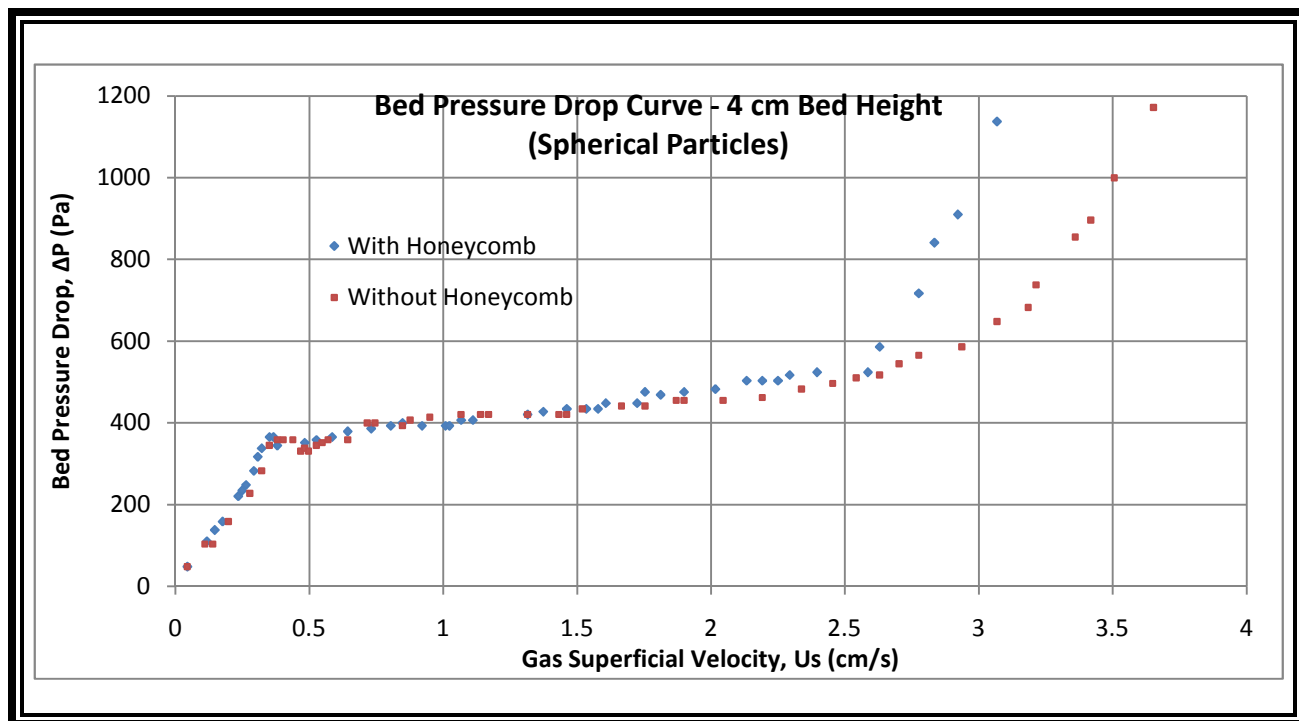


Figure 4.26: Bed (2nd Gen) performance curve with and without the honeycomb (4cm Bed)

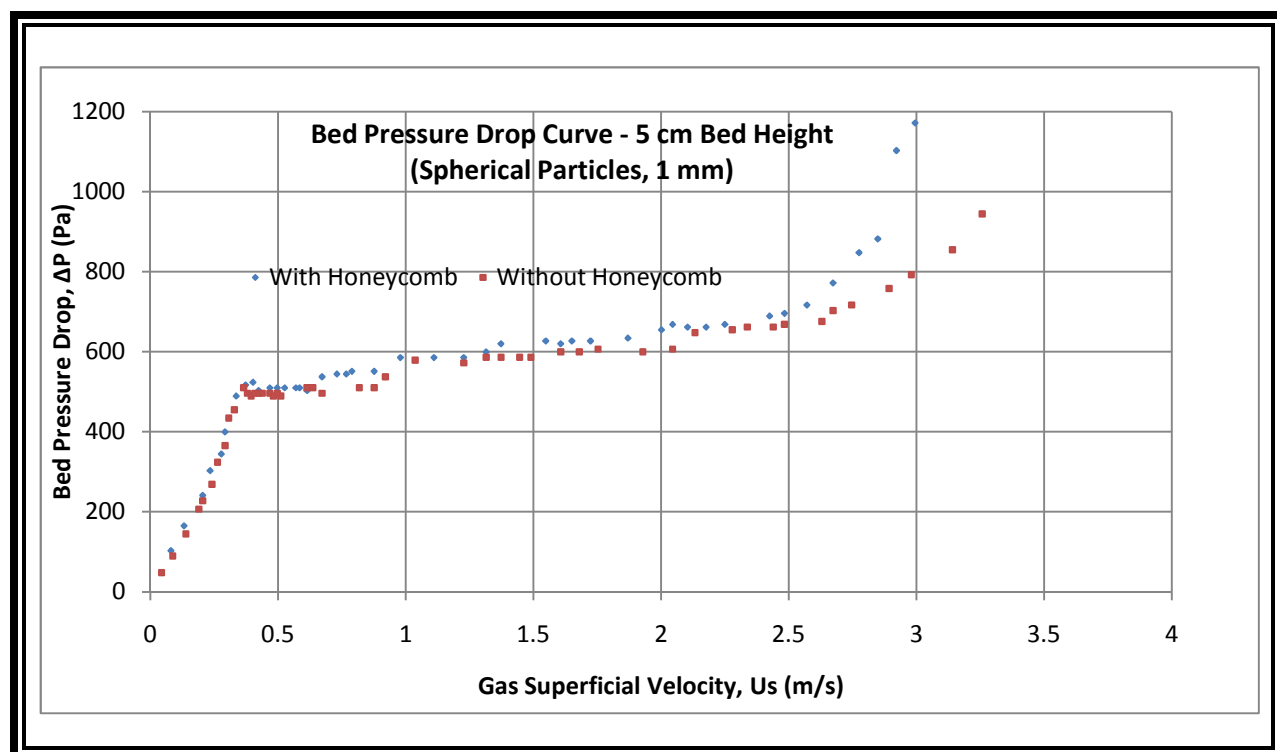


Figure 4.27: Bed (2nd Gen) performance curve with and without the honeycomb (5cm Bed)

Analytical and Experimental Pressure Drop Comparison

Table 4.4 compares the experimental pressure drop with the analytical pressure drop values at different bed heights without the honeycomb distributor along the flow field. It can be seen from this table that with increasing the static bed height the pressure drop variance keeps decreasing and at 5 cm bed height the bed pressure drop shows some deviation which might be expected in the real life fluidized bed operations.

Table 4.4: Analytical and Experimental pressure drop variance (2nd Gen)

Bed Height (cm)	Analytical Pressure Drop (Pa)	Experimental Pressure Drop (Pa)	% Deviation
2.0	291	200	31.3
2.5	321	250	22.1
3.0	352	300	14.7
4.0	538	460	14.5
5.0	685	600	12.4

Analytical and Experimental U_{mf} Comparison

Table 4.5 shows a comparison between analytical and experimental minimum fluidization velocity for the 2nd generation bed at different static bed heights and without the honeycomb.

Table 4.5: Analytical and Experimental U_{mf} variance (2nd Gen)

Bed Height (cm)	Analytical U_{mf} (m/s)	Experimental U_{mf} (m/s)
2.0	0.63	0.50
2.5	0.57	0.370
3.0	0.58	0.390
4.0	0.56	0.425
5.0	0.59	0.430

PIV Results

PIV analysis was performed for the 2nd generation fluidized bed with 1 mm spherical glass beads at 3 cm and 5 cm static bed heights. Using the CCD camera, 62 images were recorded and stored at the frequency of 62 Hz. Then scaling was done using a cm scale for the physical coordinate system. The total interrogation area was in local coordinate system 4096 pixel \times 4096 pixel and in global coordinate system 2 cm \times 2 cm. The images were taken at approximately 40 cm above the bottom (the position of

the bottom mesh screen) of the bed. After applying the auto correlation technique, flow field vectors, vorticity were extracted at an interval of 100 ms. Average velocity vector with mean particle velocity, standard deviation and correlation factors were also extracted from the PIV analysis using the Dantec Dynamic Studio software. Figure 4.28 (a) shows the 1 mm spherical particle image taken for the PIV analysis at a bed height of 3 cm and (b) shows a zoomed section of the flow field. Figure 4.29 presents two consecutive flow field vectors at an interval of 100 ms showing the change in vectors with respect to time for 3 cm bed height. Figure 4.30 shows the average velocity vector, mean particle velocity, standard deviation, and auto correlation factor analyzed from the flow field vectors. Two consecutive instantaneous vorticity magnitudes at an interval of 100 ms are also presented in Figure 4.31. These results are for the 3 cm bed height. The results for the 5 cm bed height are presented from Figure 4.32 to 4.34.

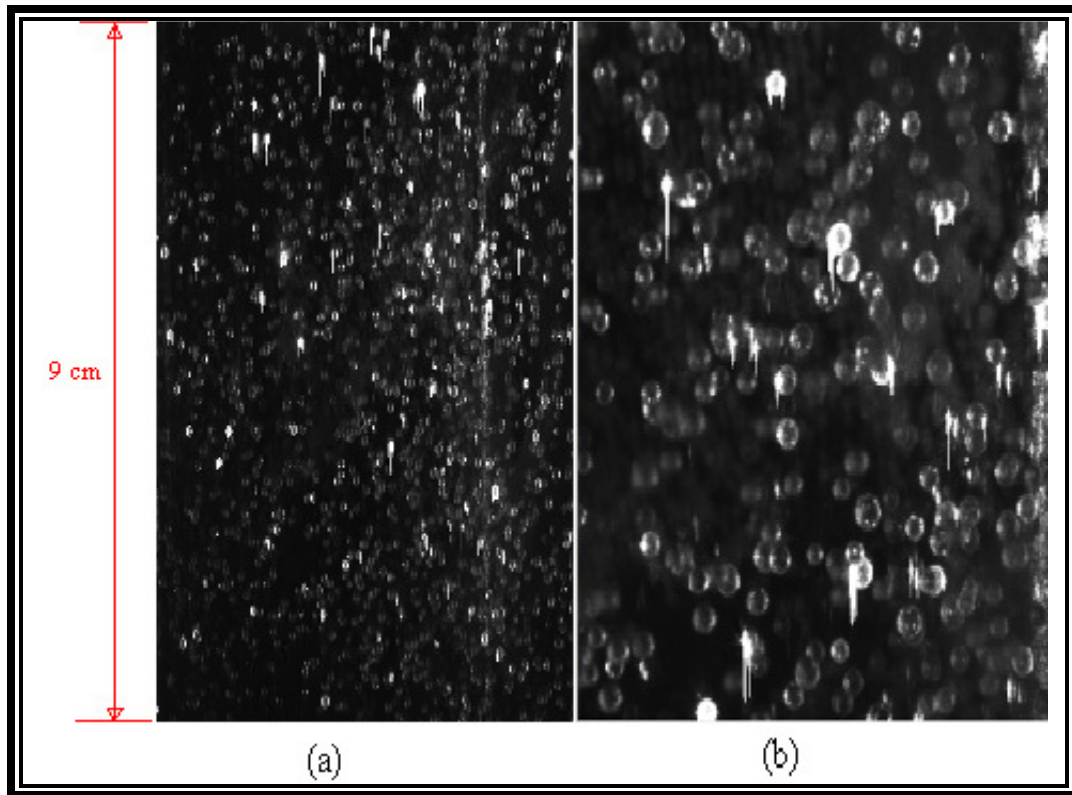


Figure 4.28: (a) Particle image for PIV analysis showing (b) a zoomed section

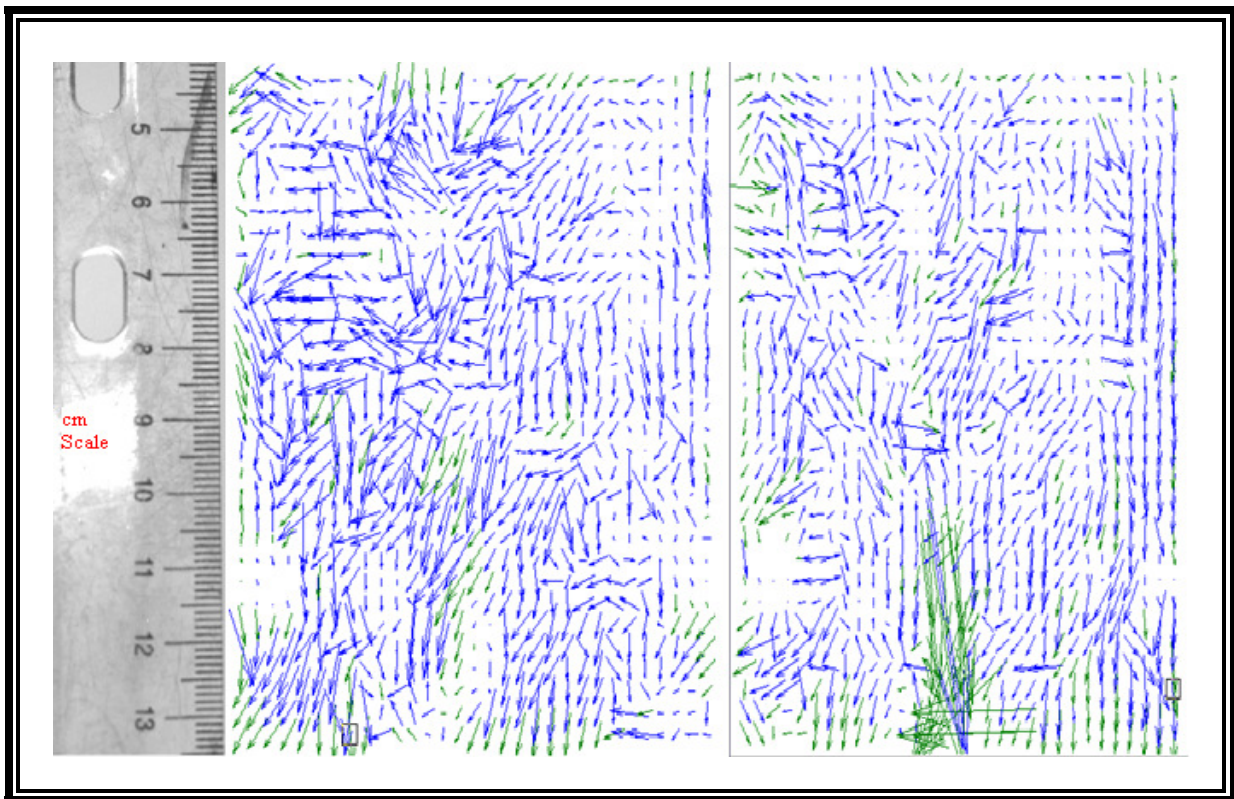


Figure 4.29: Instantaneous flow field vector for 3 cm bed height (2nd Gen)

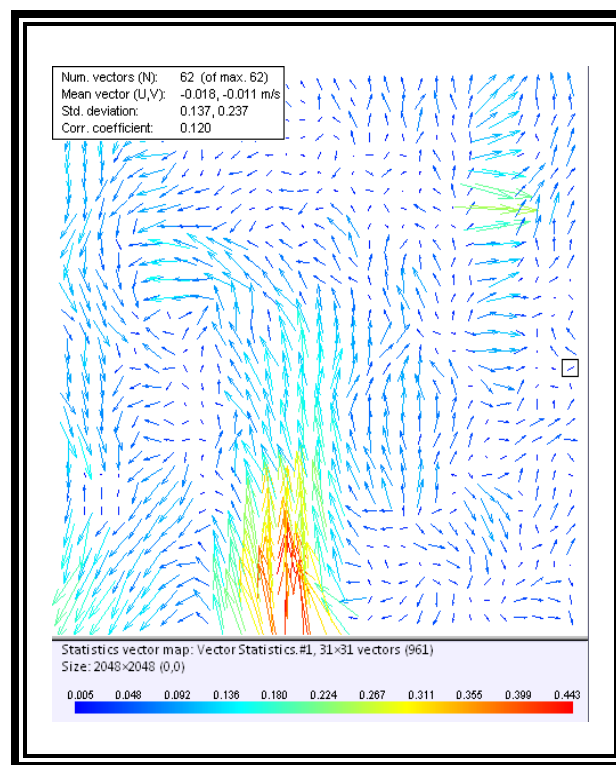


Figure 4.30: Average flow field vector at 3 cm bed height (2nd Gen)

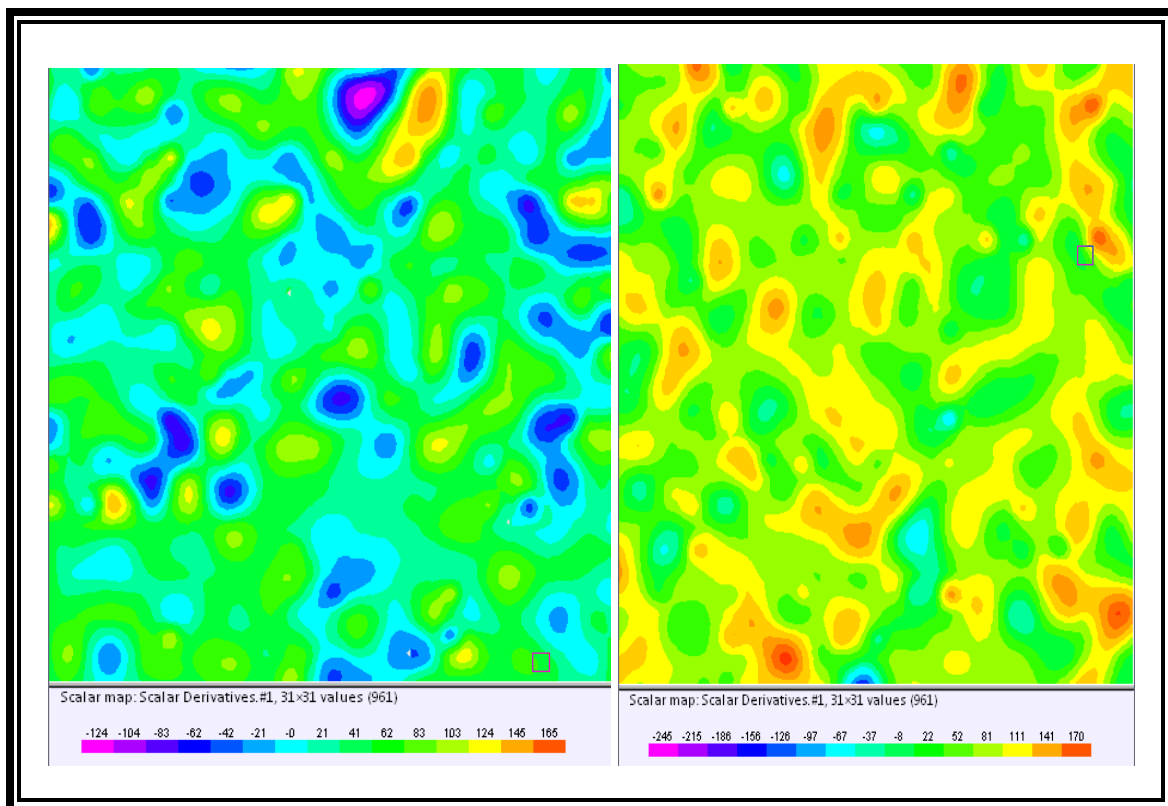


Figure 4.31: Instantaneous vorticity at 3cm bed height (2nd Gen)

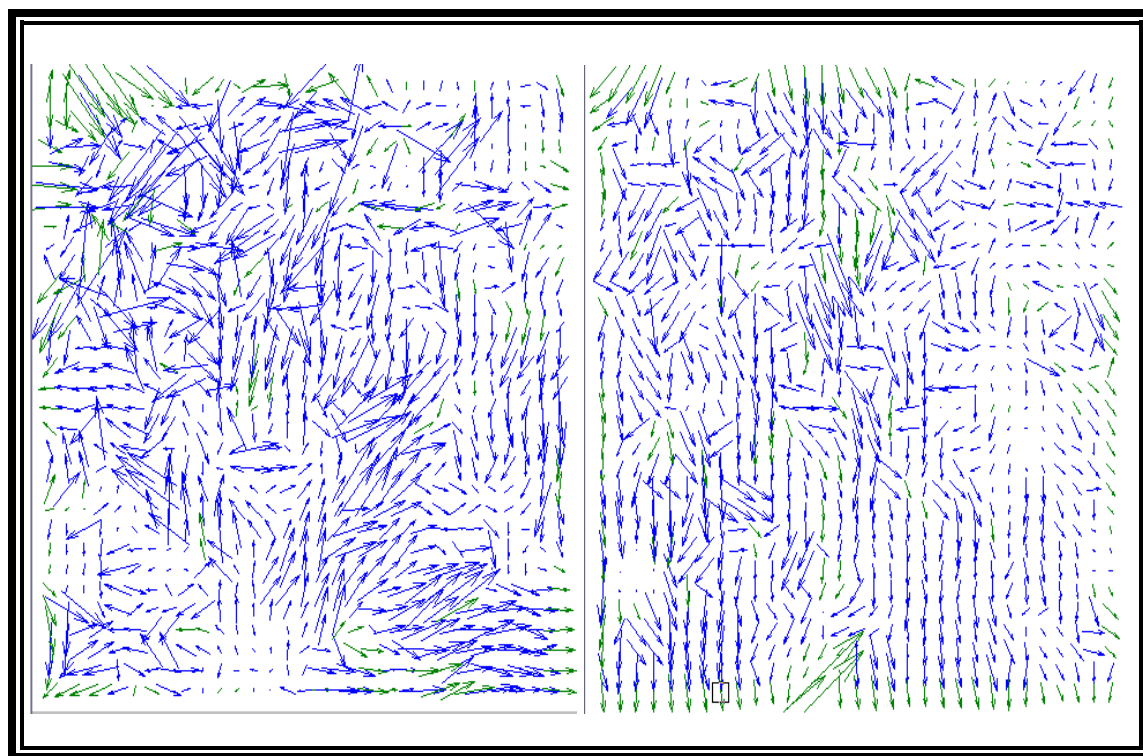


Figure 4.32: Instantaneous flow field vector at 5 cm bed height (2nd Gen)

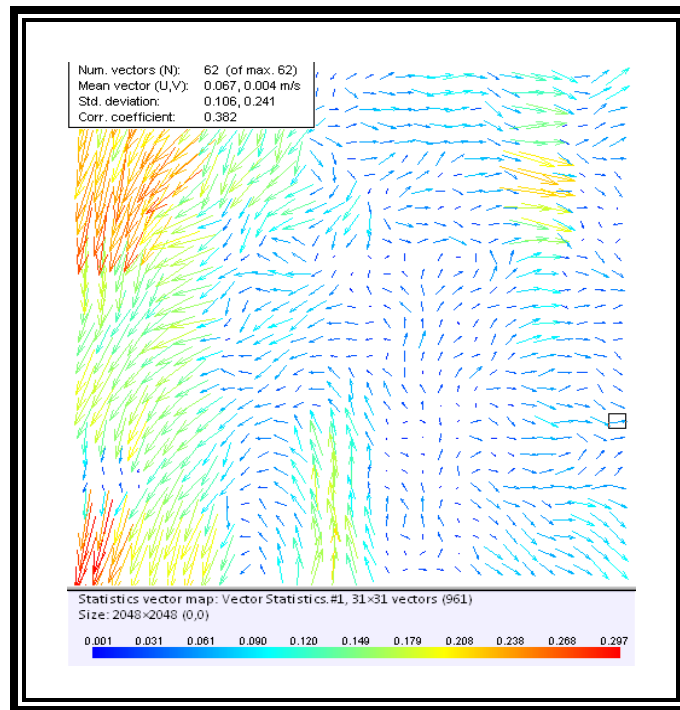


Figure 4.33: Average flow field vector at 5 cm bed height (2nd Gen)

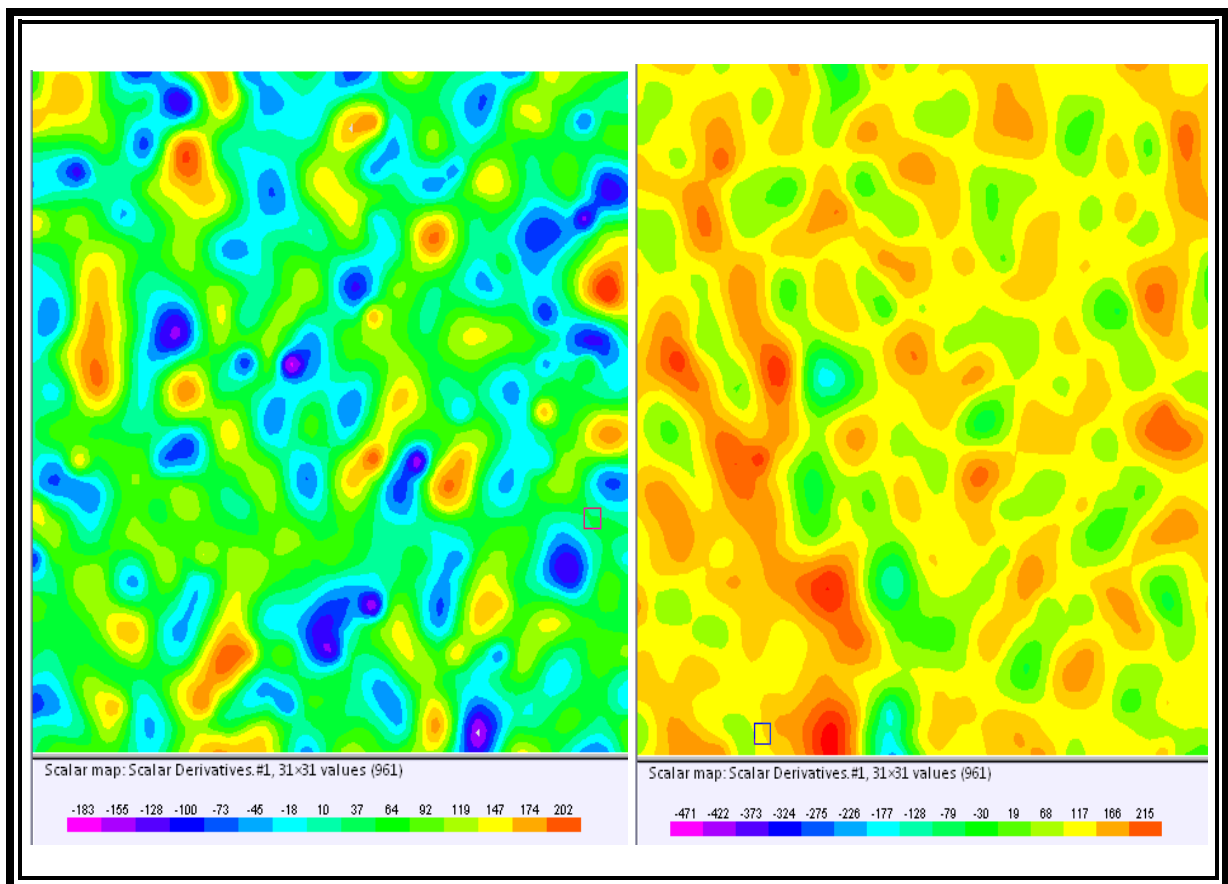


Figure 4.34: Instantaneous vorticity at 5 cm bed height (2nd Gen)

Bed Behavior

Different flow regimes are also observed while fluidizing the particles with air flow. Figure 4.35 shows the fixed bed regime for the 2nd generation bed operated with 1 mm spherical particles at a static bed height of 5 cm.

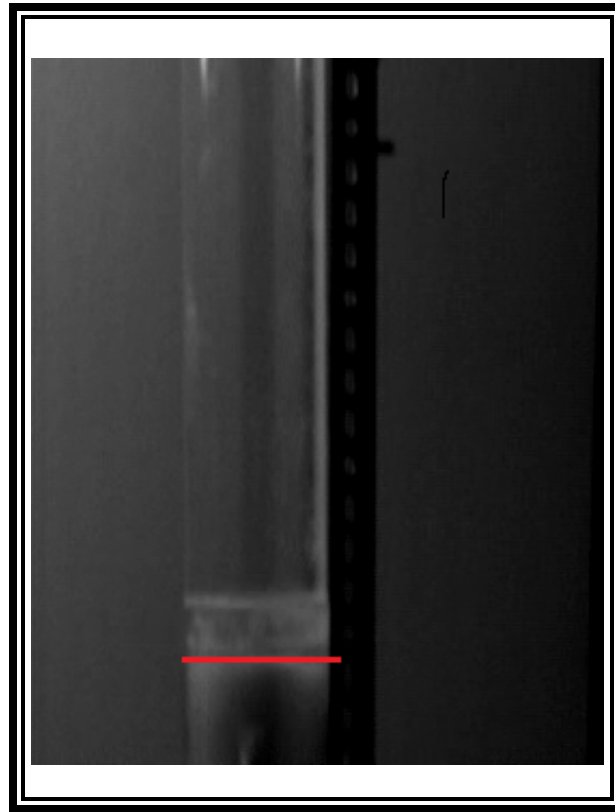


Figure 4.35: Fixed bed regime (2nd Gen)

The bed behavior at minimum fluidization is shown in Figure 4.36. At this point the bed starts expanding with all the particles just gets suspending. Due non-uniform flow distribution of fluid the bed expands from a side of column wall. As the superficial gas velocity is increased after the minimum bubbling velocity, bubbling starts, and the gas bubbles generated in this regime coalesce and grow as they move upward through the bed. The bubbling bed regime is presented in Figure 4.37.

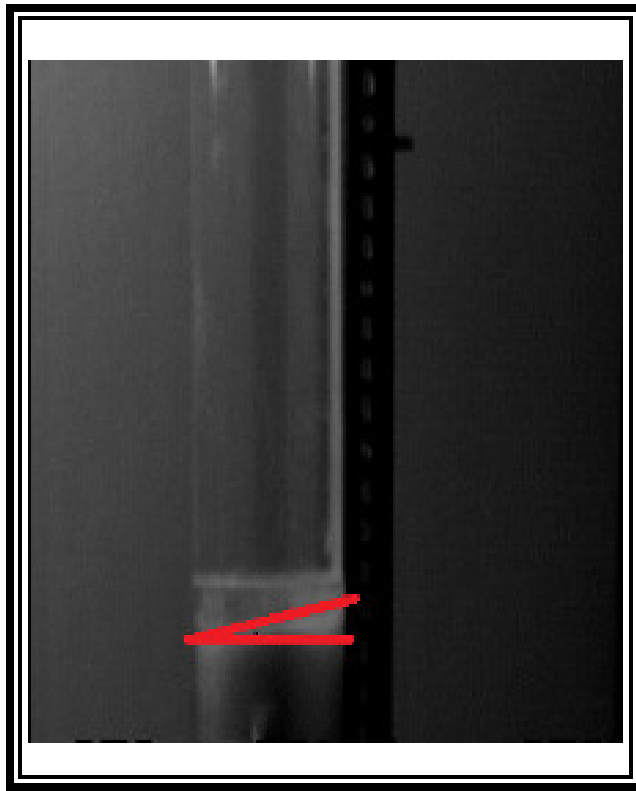


Figure 4.36: Bed (2nd Gen) at U_{mf}

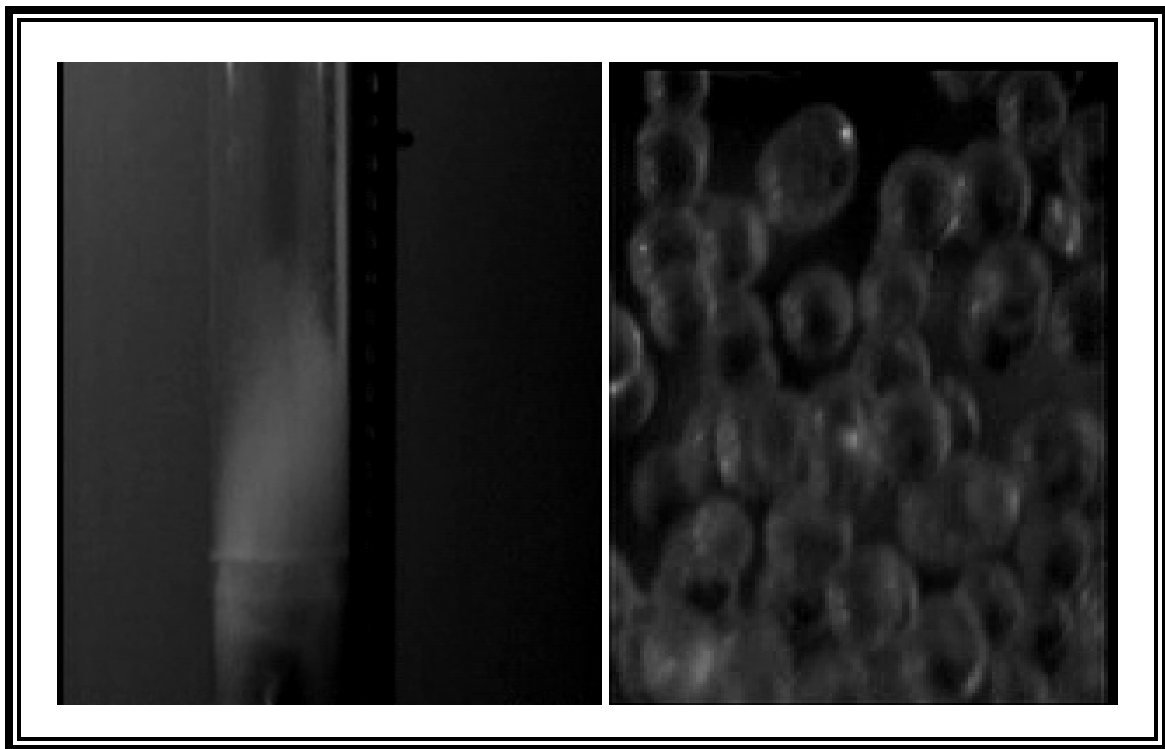


Figure 4.37: Bubbling bed regime (2nd Gen)

With increasing the gas velocity further the bubbles keep growing large enough to spread across the diameter of the column, and after a certain point the turbulent motion of solids cluster and gas void of different shape and size are observed which is termed as the turbulent fluidized bed regime. Figure 4.38 shows the turbulent churning regimes.

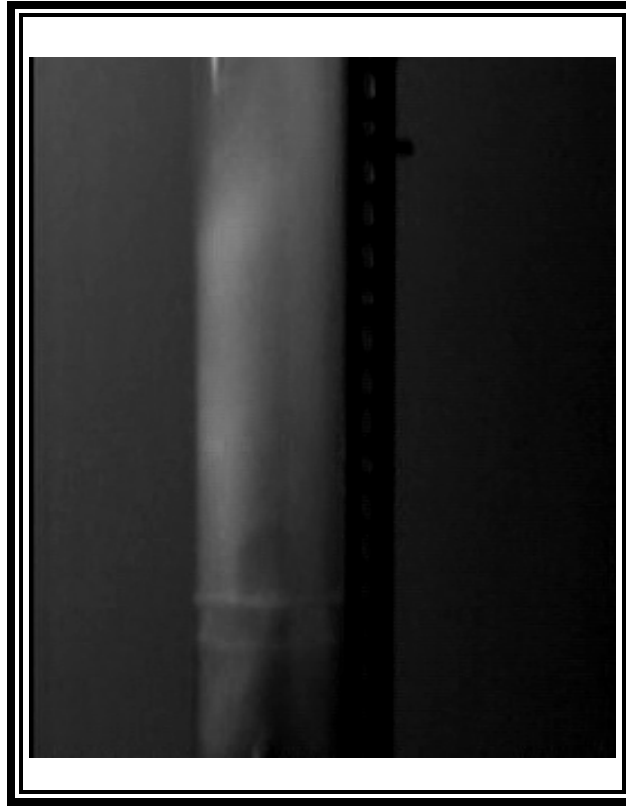


Figure 4.38: Turbulent churning regime (2nd Gen)

Since the particles were restrained to escape from the column using a mesh catch at the top, hence, the fast fluidization and pneumatic transport regimes were not possible to capture for the current study.

4.2.2 Results for Non-Spherical Particles

The non-spherical particles used for this bed were crushed from 6 mm glass beads. The experimental results obtained for the 2nd generation bed operated with non-spherical particles are presented in the following sections.

Particle Size Distribution

The sieve test analysis was applied to estimate the non-spherical particle size distribution. The particle size distribution used for this bed is shown in Figure 4.39. The distribution shows that the non-spherical particles were in the range of 150-2000 μm with mean particle size of 680 μm .

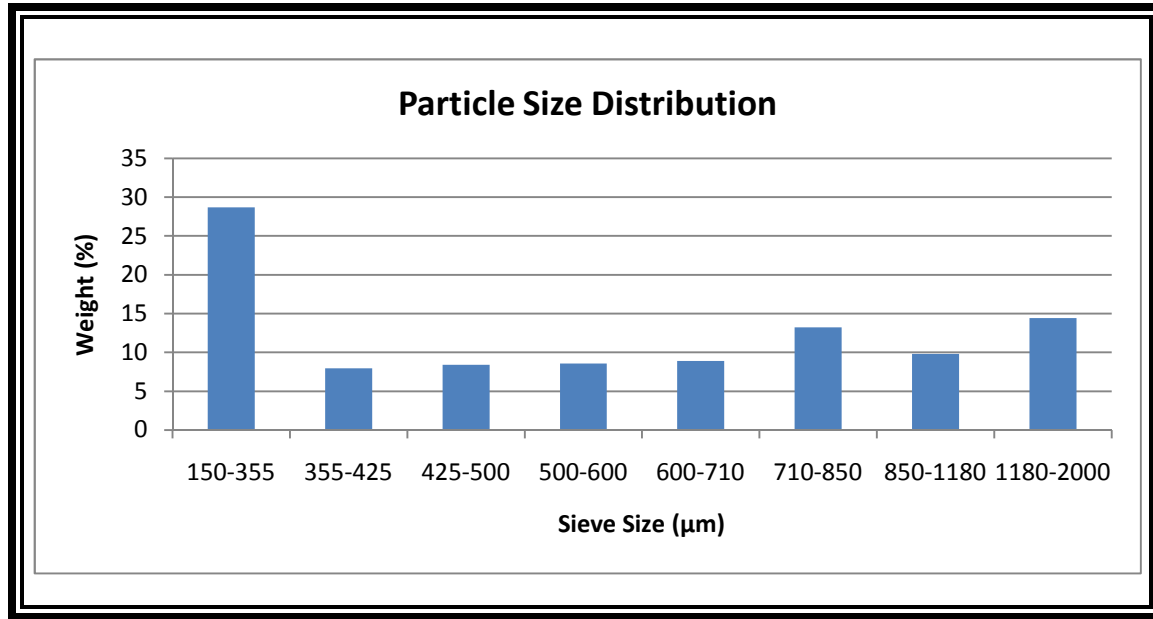


Figure 4.39: Particle size distribution for 12 cm bed

Particle Sphericity

To make the particle sphericity analysis more reliable and convenient another method was implemented in case of particles used for the 2nd generation fluidized bed instead of the previous method applied earlier for the 1st generation fluidized bed. Eqn. (4.3) was used in this case⁴⁵:

$$\phi = \frac{d}{a} \quad (4.3)$$

Where d is the nominal diameter of the particle and a is the longest diameter of the particle circumscribing a sphere.

The nominal diameter of the particles was estimated from the sieve test analysis and the longest length circumscribing a sphere was determined using the microscopic video camera and the Dino Capture software. This software has a built-in circumscribing circle drawing capability with respect to its local coordinate which was then transformed into the physical coordinate using a calibration scale.

The sphericity was found to be in the range of 0.35 to 0.75. Using this method particles were categorized according to its sphericity range for the drag analysis. An example of sphericity analysis is shown below.

For a particular non-spherical particle shown in Figure 4.40, the nominal diameter was 0.78 mm. The longest diameter was found to be 3.81 mm in the software's local coordinate and with magnification factor of 20. This result is shown in Figure 4.41. The correction factor to convert this local coordinate value into physical one was determined using a scale with known dimension as shown in Figure 4.42. Here physical 1 mm represents to local 2.87 mm. Then the sphericity was calculated using Eqn. (4.3) and was found to be 0.59.



Figure 4.40: Particle for sphericity analysis

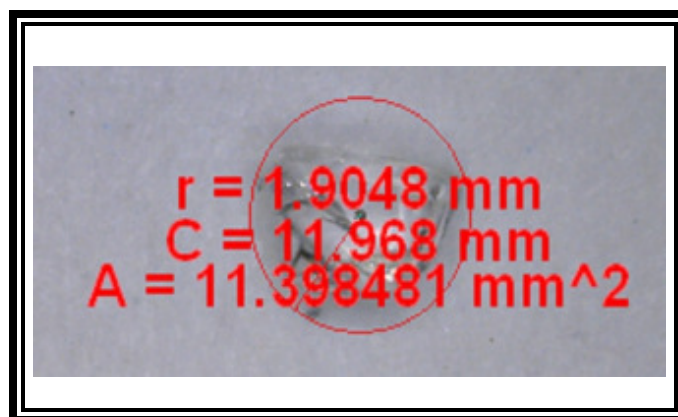


Figure 4.41: Particle longest diameter tracking

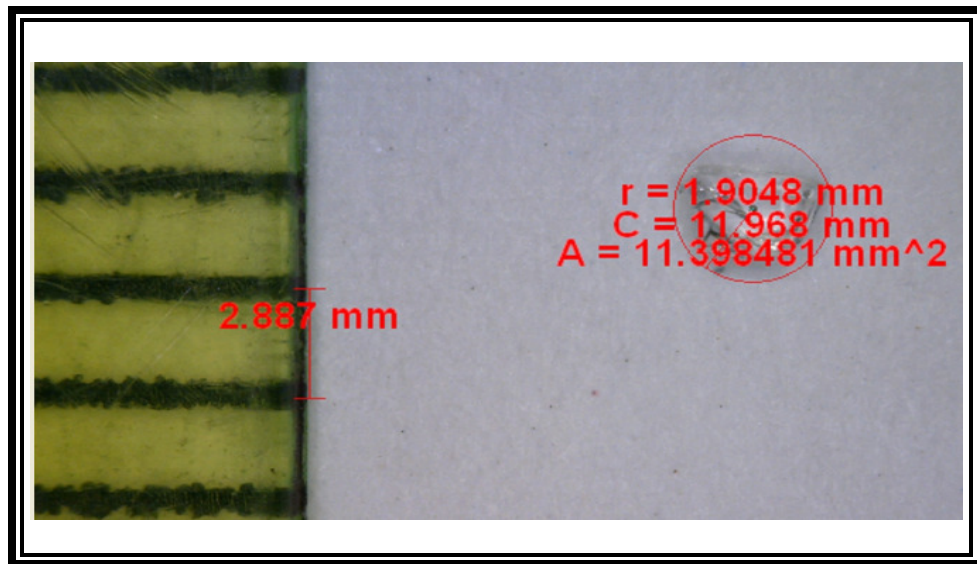


Figure 4.42: Correction factor measurement

Particle Classification

According to the Geldart classification of particles for air at ambient conditions (Fig. 2.10), the non-spherical particles can be classified as Geldart group D. Here the gas density was used as the air density 1.21 kg/m^3 . The grouping is shown in Figure 4.43.

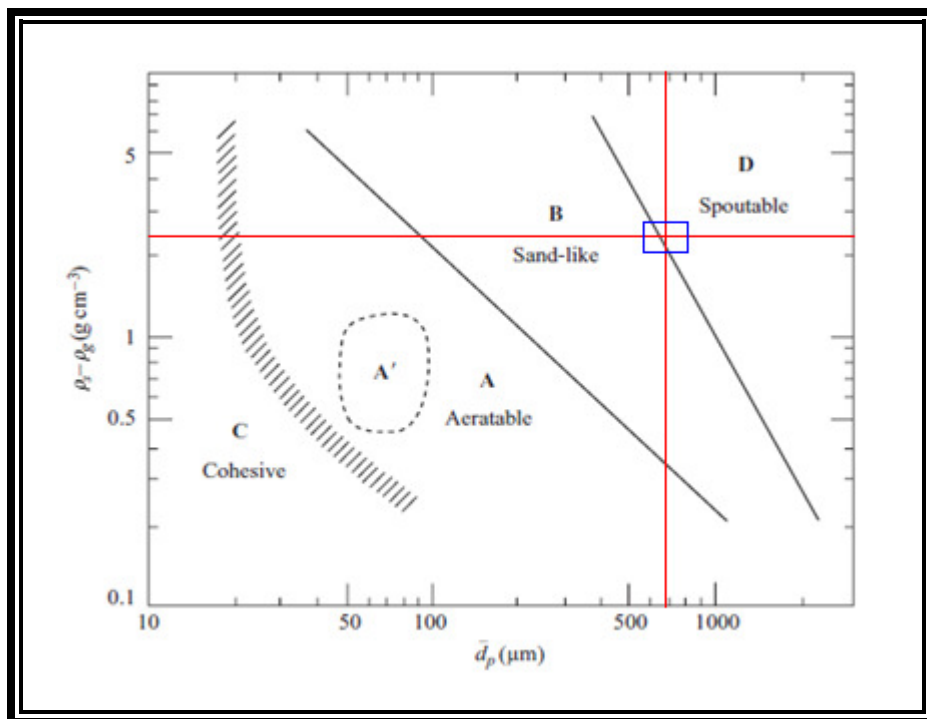


Figure 4.43: Particle classification

Bed Pressure Drop

Figure 4.44 shows the bed pressure drop without honeycomb for non-spherical particles with increasing the gas superficial velocity. From the figure it can be observed that the bed starts expanding after 0.15 m/s gas superficial velocity. Since the particle size used in this experiment consists of a wide range of particles with approximately 30% fine powder, the fine powders start expanding earlier than the other larger particles. Hence, a complete unusual fluidization behavior of the bed is observed in this case.

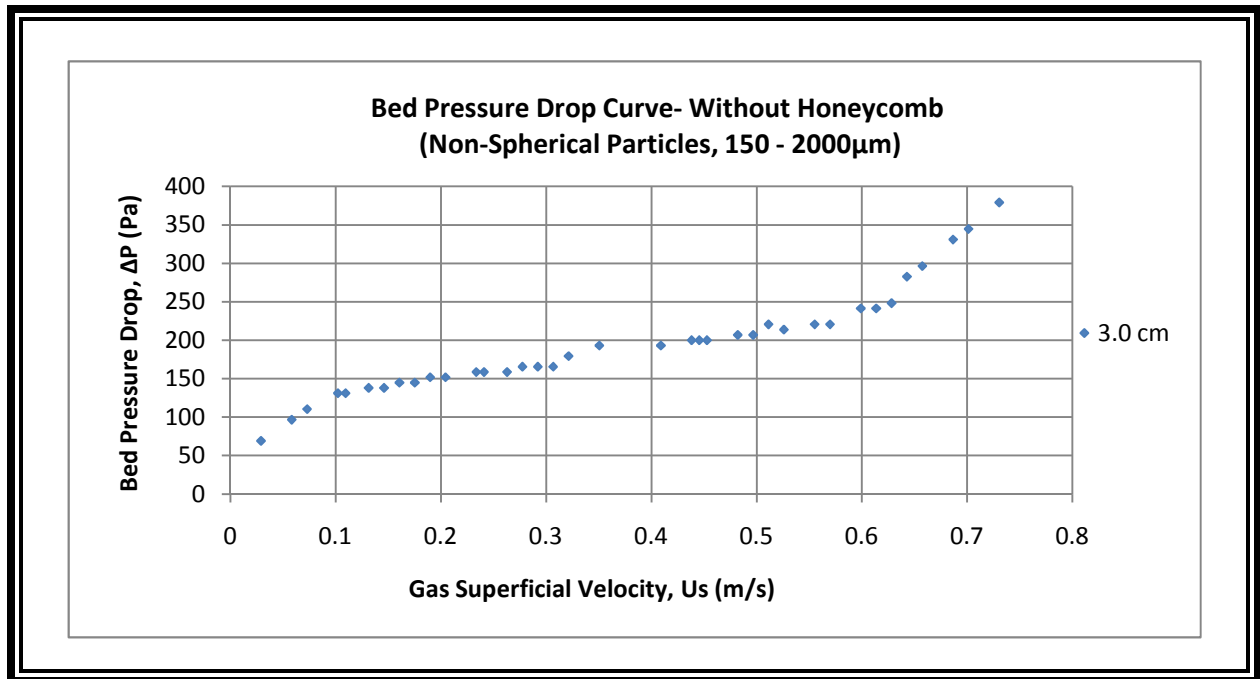


Figure 4.44: Bed (2nd Gen) performance curve with non-spherical particles

Effect of Bed Height

Figure 4.45 and Figure 4.46 shows the bed pressure drop at different bed heights without and with the honeycomb respectively. Since the non-spherical particles are composed with approximately 30% powders in the range of 150-355 µm, the bed behavior is not evident like the spherical particles. Even due to a very low pressure drop initially, and since, the pressure transducer sensitivity is in a very large range, hence, the pressure drop measurements before the minimum fluidization does not seem to make a better impression on the characterization of bed behavior with non-spherical particles.

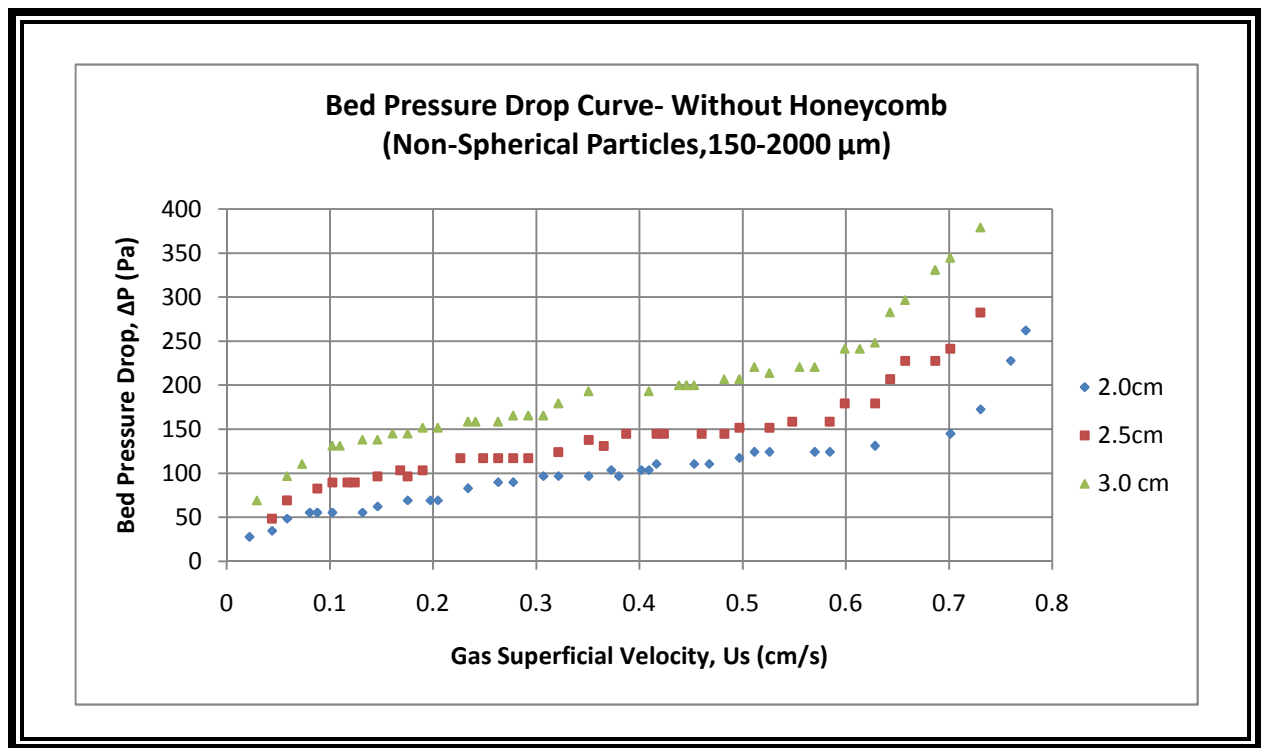


Figure 4.45: Bed (2nd Gen) performance curve at different bed heights (without honeycomb)

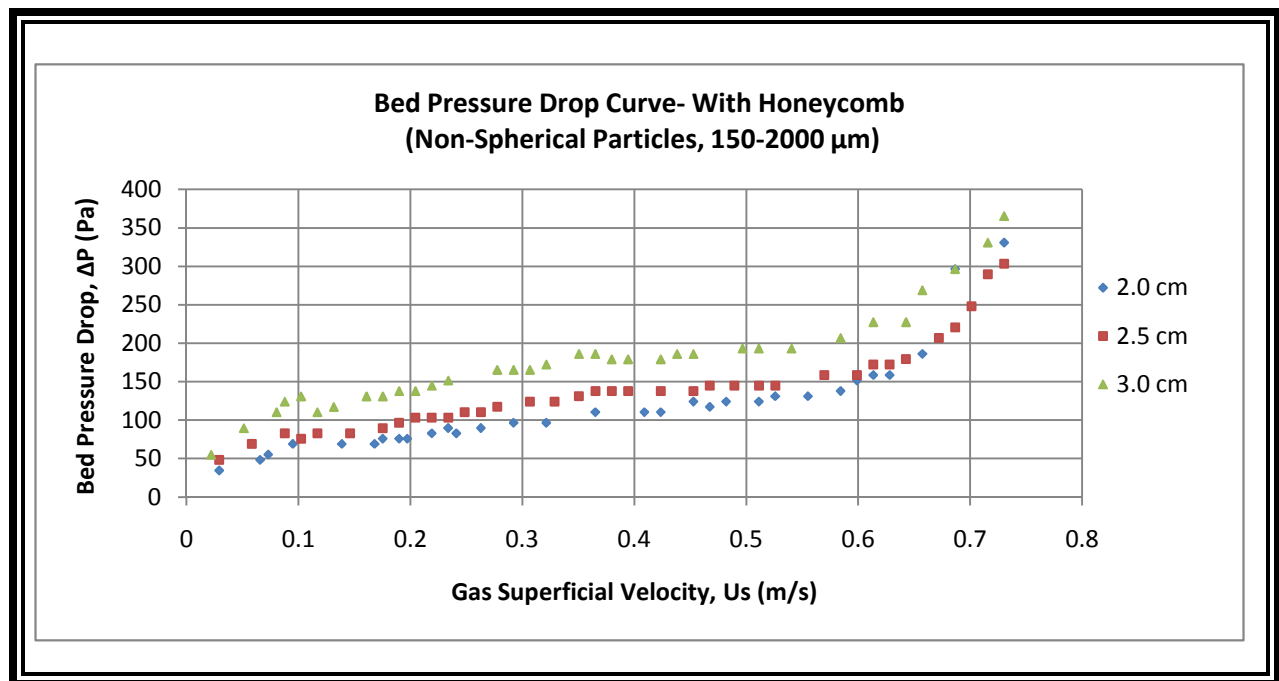


Figure 4.46: Bed (2nd Gen) performance curve at different bed heights (with honeycomb)

Effect of Blockage Ratio

Figure 4.47 presents the bed pressure drop with increasing the gas superficial velocity at a static bed height of 2.5 cm operated with non-spherical particles with and without the honeycomb. From this graph it can be clearly seen that though initially the flow rate is increasing the pressure drop is not increased that much which is too obvious for the curve with honeycomb. Hence, it concludes that for non-spherical particles used in this experiment, the flow distributor is creating much more pressure drop across its orifices. That might be a reason for not getting any response from the pressure sensor in the initial region. Another reason lies here that the pressure transducer sensitivity is in a larger range 0 to 3750 Pa. With this range and accuracy of $\pm 1\%$, the differential pressure transducer is not supposed to provide very good measurements at the lower pressure drop values. Hence, no data points are seen at the initial region. Figure 4.48 shows the same result at a static bed height of 3 cm. For the 3 cm bed case, the minimum fluidization, hump sections are at least visible whereas for the 2.5 cm bed, these points are impossible to recognize.

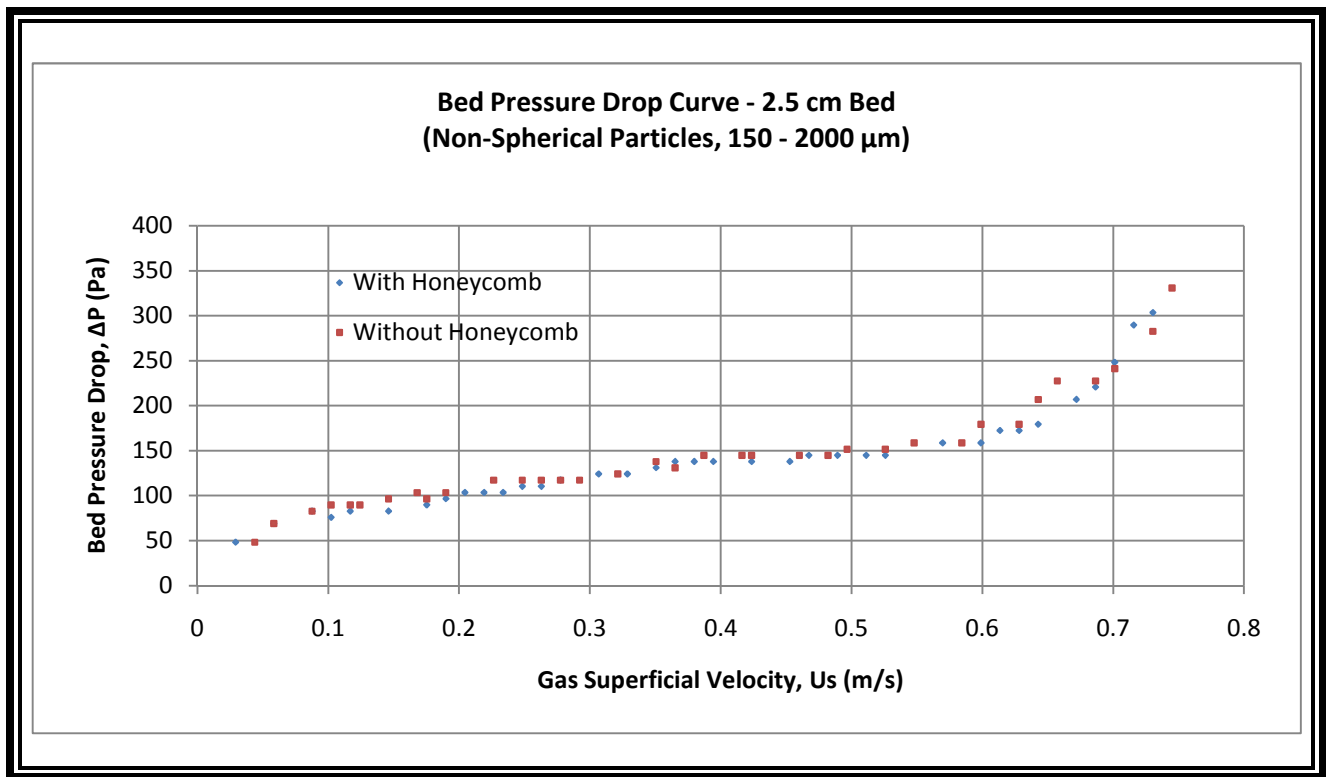


Figure 4.47: Bed (2nd Gen) performance curve with and without the honeycomb (2.5 cm Bed)

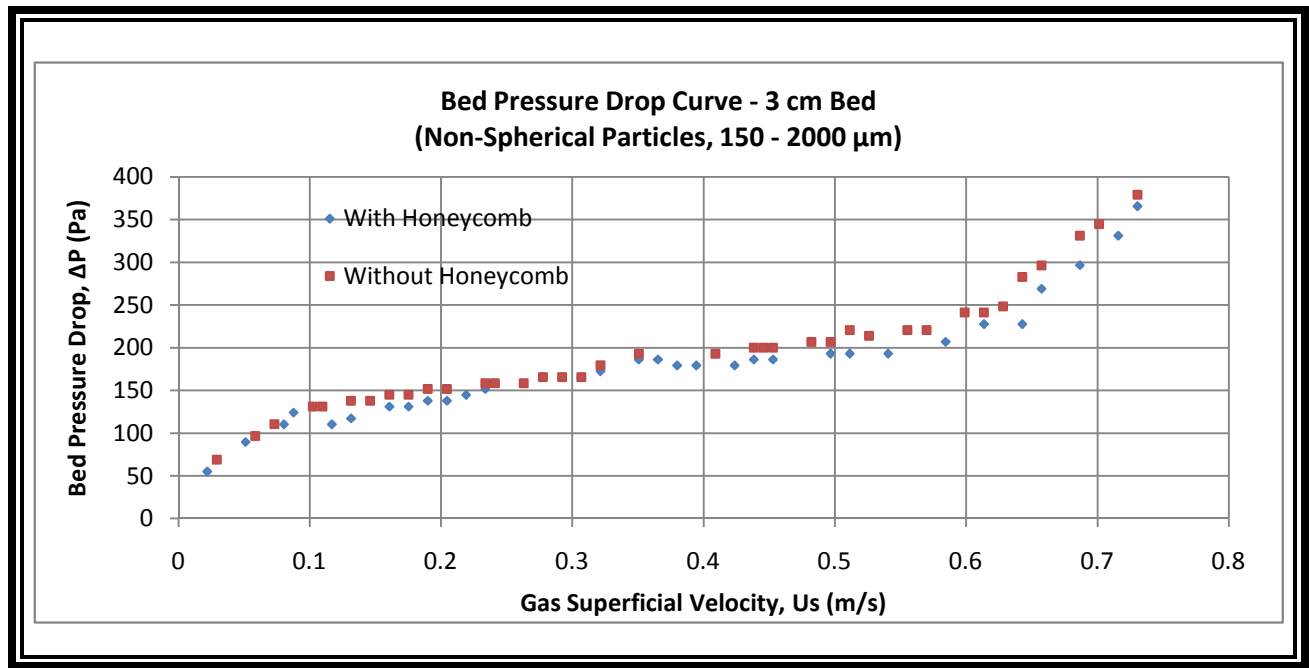


Figure 4.48: Bed (2nd Gen) performance curve with and without the honeycomb (3 cm Bed)

PIV Results

Figure 4.49 presents the flow field vector for 150-2000 μm particles at a static bed height of 3 cm at the gas superficial velocity. Figure 4.50 shows the average velocity vector and Figure 4.51 presents the vorticity of non-spherical particles. The interrogation area for this PIV system was 1024 pixel \times 1024 pixel in local coordinate or in global coordinate 5 mm \times 5 mm.

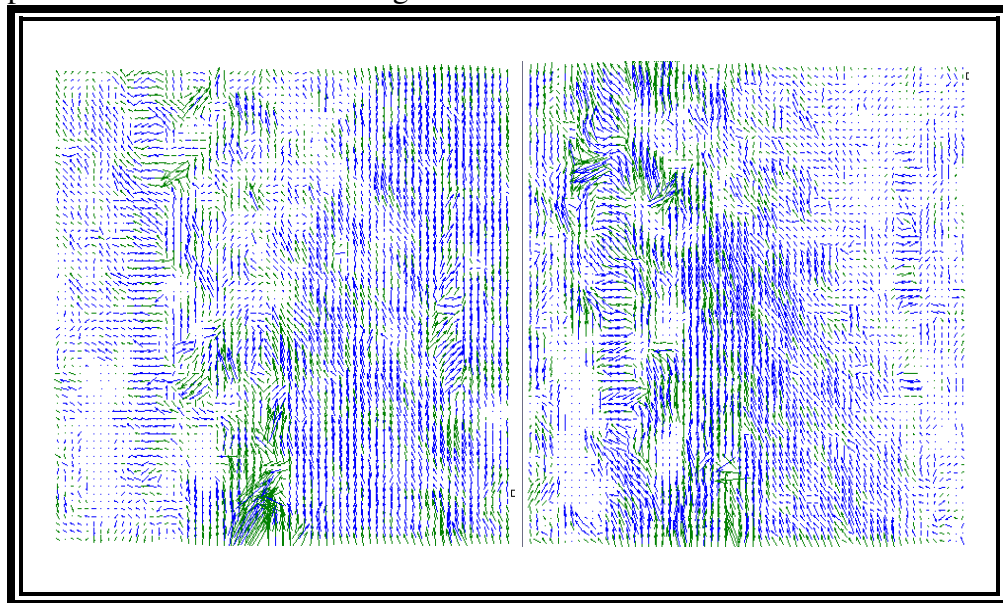


Figure 4.49: Instantaneous flow field vector at 3 cm bed height (2nd Gen)

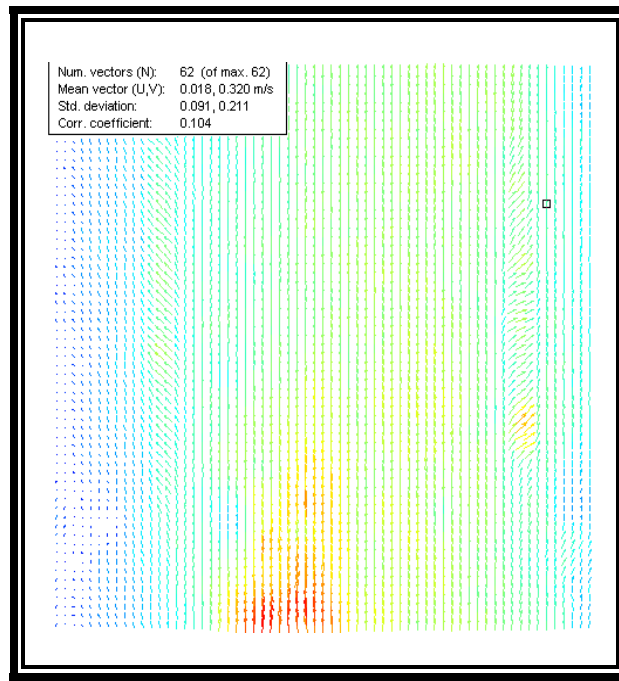


Figure 4.50: Average flow field vector at 3 cm bed height (2nd Gen)

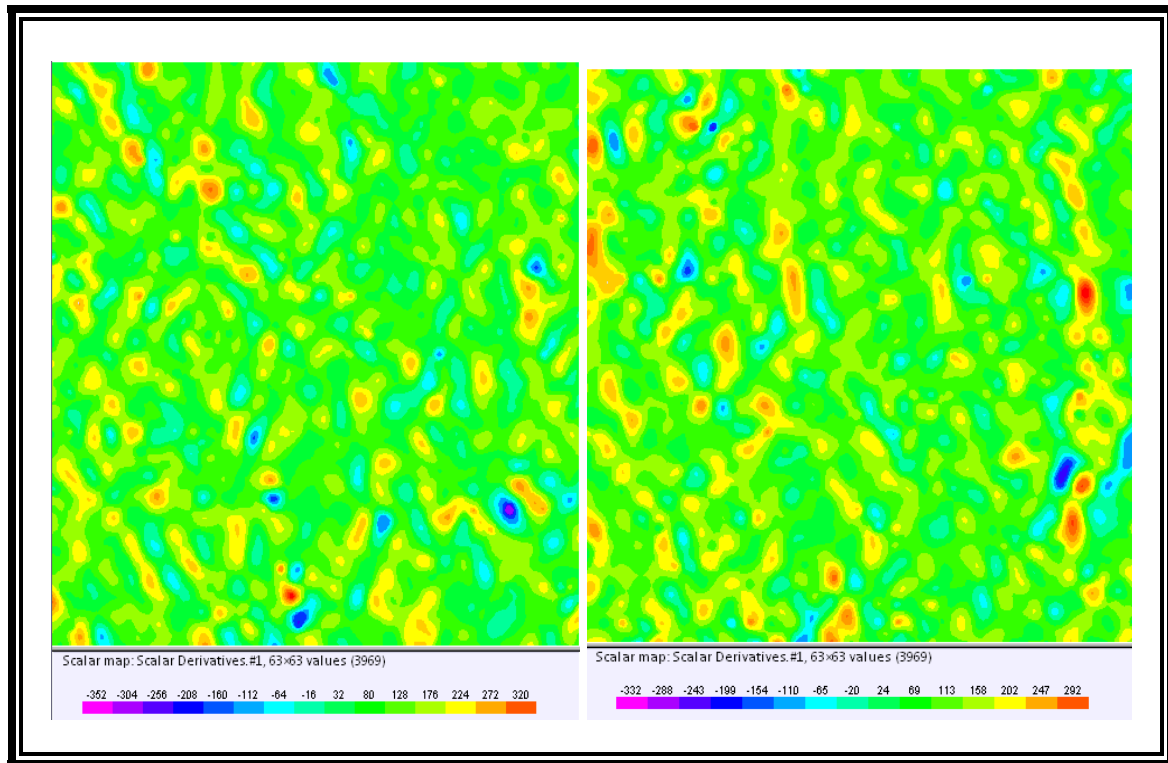


Figure 4.51: Instantaneous vorticity at 3 cm bed height (2nd Gen)

4.2.3 Effect of Particle Sphericity

The comparisons of bed performance with respect to spherical and non-spherical particles without using flow straighter and using the flow straighter are presented in Figure 4.52 and Figure 4.53. From the figures it can be seen that the data for the non-spherical particle have the gas superficial velocity range between 0.1 to 0.8 m/s whereas the spherical particles have range greater than 4. The non-spherical particles were selected from a range of 150 to 2000 μm where most of the particles are in the range of 150 to 700 μm or in other words powders. Hence, the 150-600 micron particles are producing more pressure drop across the bed with a very low flow requirement. They are reaching the terminal velocity earlier than the other particles, and hence they are trying to escape from the bed. But the spherical particles due to highly packed they require for more air flow than the non-spherical particles. Here, the packing of the particles due to sphericity might be another reason for the requirement of drag force for which the non-spherical particles as a whole are showing completely non-uniform fluidization behavior.

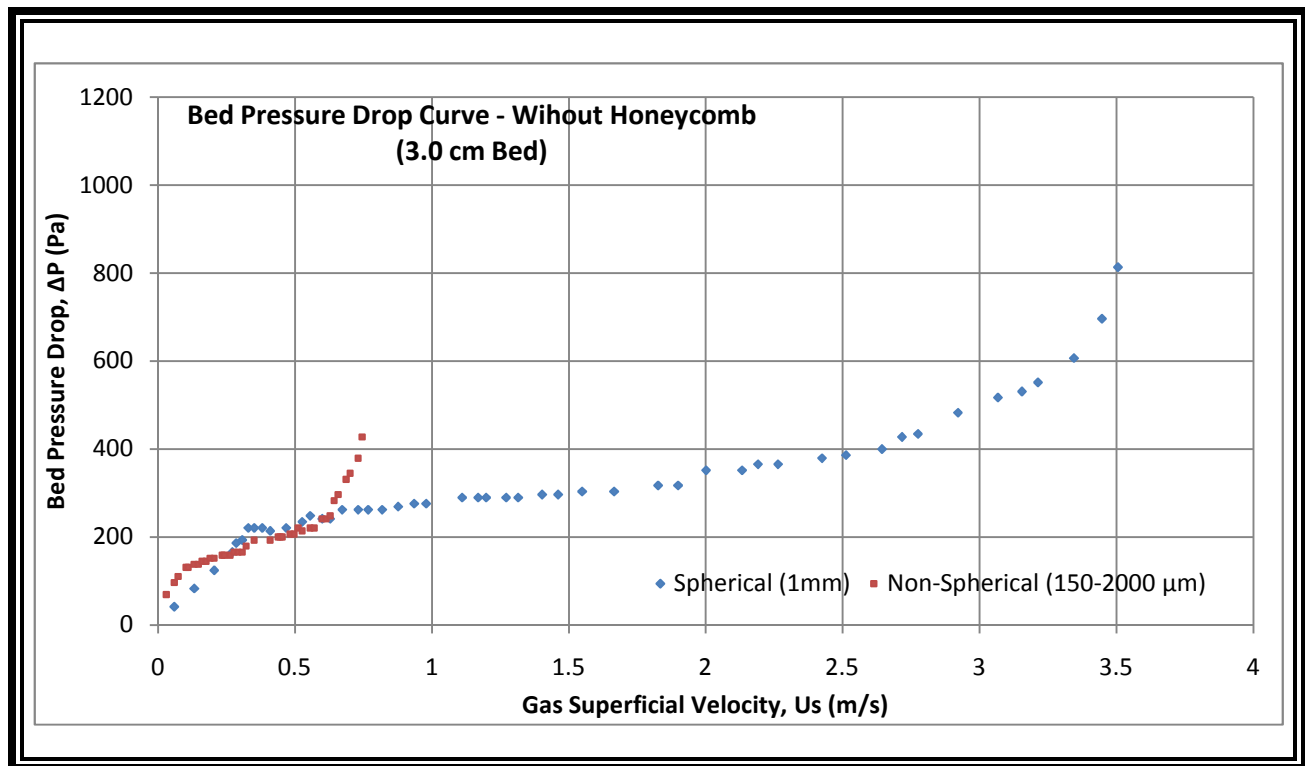


Figure 4.52: Bed performance curve with spherical and non-spherical particles without honeycomb

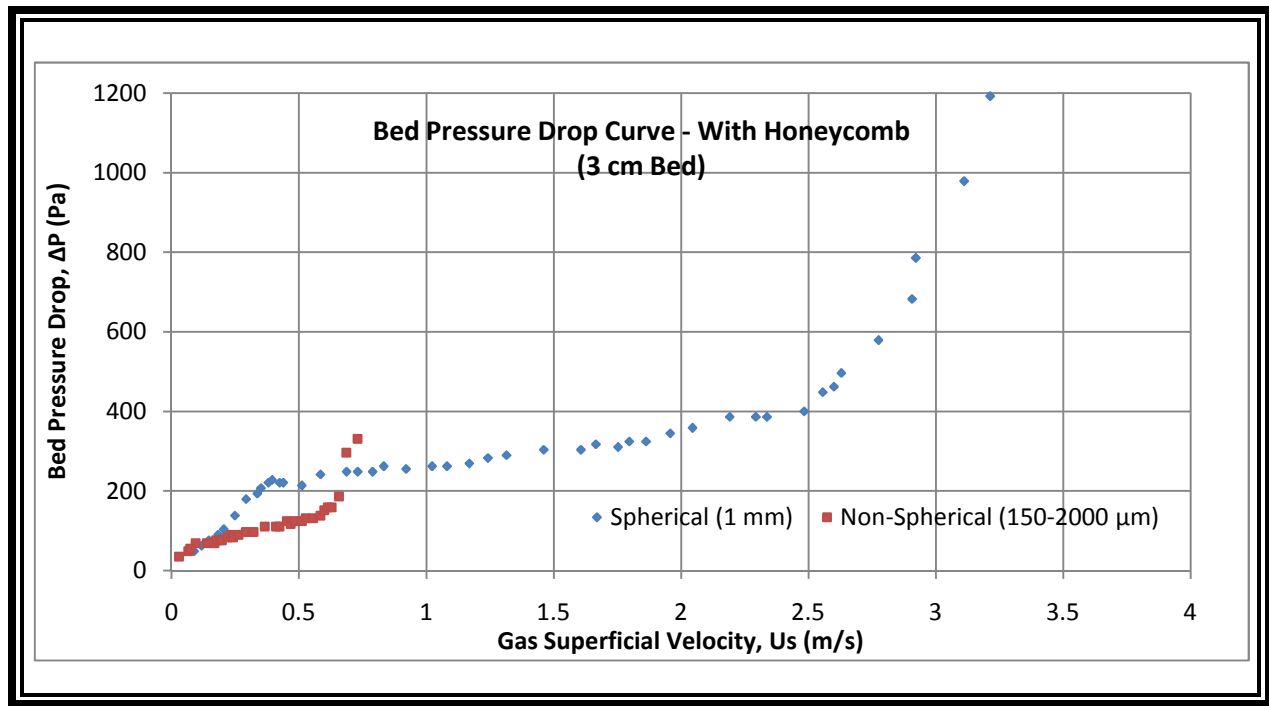


Figure 4.53: Bed performance curve with spherical and non-spherical particles with honeycomb

4.3 EFFECT OF BED DIAMETER

Figure 4.54 presents the effect of bed diameter on fluidization at a static bed height of 5 cm using 1 mm spherical glass beads. Due to large volume of particles, the total mass in 2nd Gen bed is higher than that of 1st Gen bed. Still the analytical pressure drop for both of the bed is approximately same. From the graph it can be seen that the bed pressure drop gradually increases for 2nd Gen bed after the minimum fluidization which means non-uniform fluidization occurs in this region whereas for the 1st Gen cm bed, the pressure drop curve shows approximately constant behavior after the minimum fluidization and up to the maximum fluidization. On the other hand, the 1st Gen bed with a static bed height of 5 cm is assumed to be a long shallow bed for which the fluidization behavior is not supposed to be better. Hence, the use of 2nd Gen bed makes more robust choice as the fluidized bed rather than the 1st Gen bed. The bed performance for the 2nd Gen bed could be more developed using a better designed flow distributor, a low range high sensitivity differential pressure transducer.

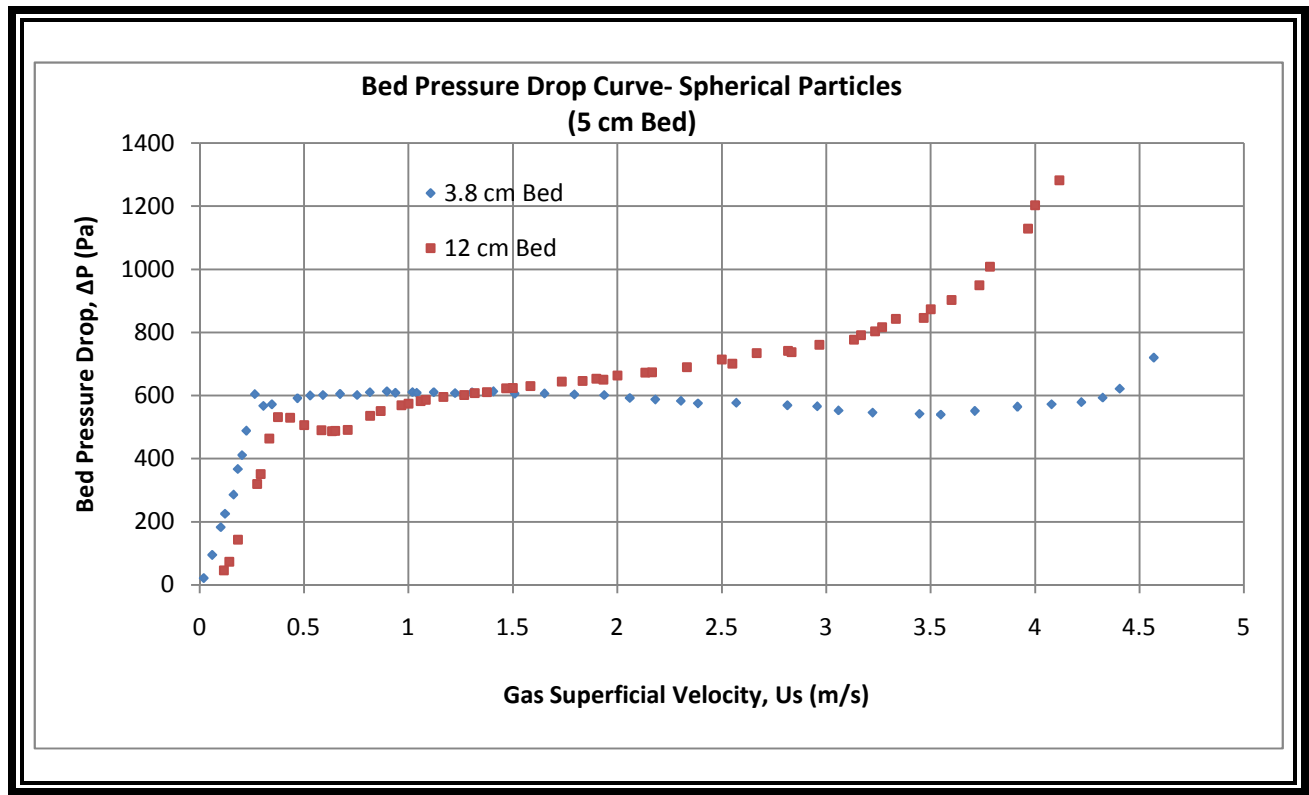


Figure 4.54: Effect of bed diameter on bed performance

4.4 DRAG ANALYSIS RESULTS

The drag coefficient analysis was initiated with a single particles rice grain. Then the multiple particles crushed non-spherical particle drag analysis was performed to attain the drag coefficient values. All experimental data were then compared to Haider and Levenspiel drag correlation for non-spherical particles presented in Eqn. (2.19).

4.4.1 Single Particle Drag Analysis

The rice grains shown in Figure 4.55 were assumed to be ellipsoid in shape. To approximate the sphericity of the rice particle, 35 particles were measure using a vernier caliper. The average equatorial diameter along X-axis was found to be approximately 6.76 mm, average equatorial diameter along Y-axis was found to be 2.076 mm, and average polar diameter along Z-axis was found to be approximately 1.72 mm. Then the sphericity of the particle was determined using Eqn. (4.4) and was found to be approximately 0.43.

The initial terminal velocity for determining the approximate particle travel distance was calculated using Eqn. (4.4) which is the modified terminal velocity equation derived for ellipsoidal rice particle.

$$V_t = \sqrt{\frac{\frac{8}{3} c g (\rho_s - \rho_f)}{\rho_f C_D}} \quad (4.4)$$

Where V_t is the terminal velocity, c is the mean polar diameter of rice particle along the z-axis, ρ_s is the density of rice grain, ρ_f is the density of air, and C_D is the drag coefficient.

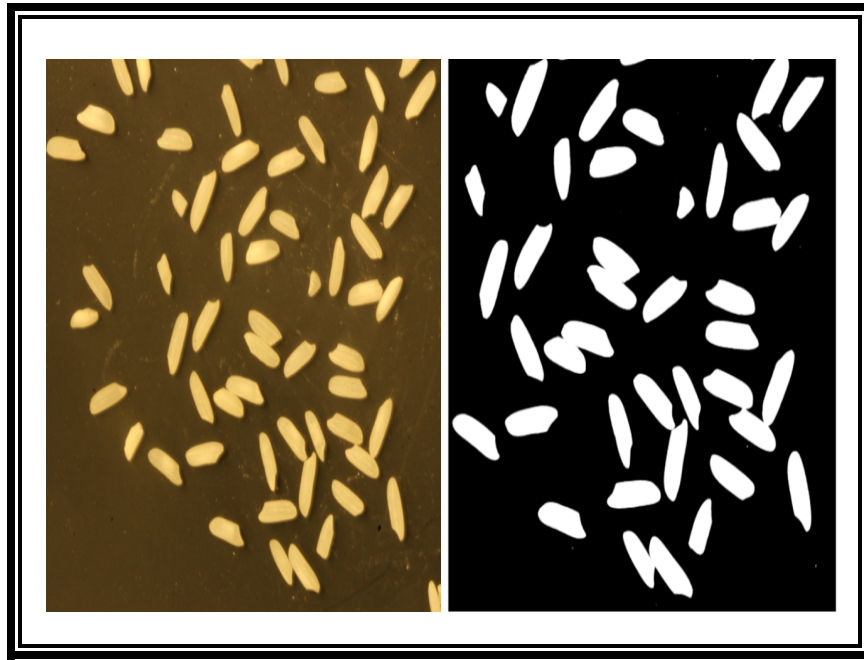


Figure 4.55: Magnified photograph of rice grains

The distance from top of the bed to the point where a single particle was supposed to reach the terminal velocity was calculated using Eqn. (3.3). Assuming the rice density as 577 kg/m^3 , air density as 1.2 kg/m^3 , the preliminary terminal velocity was found to be approximately 5.94 m/s and the height required to obtain the free falling terminal velocity was found to be approximately 1.8 m .

The camera frame length traveled by a single particle, presented in Figure 4.56, was measured using an mm scale. After obtaining the travel time, the particle terminal velocity was obtained using Eqn. (3.4).

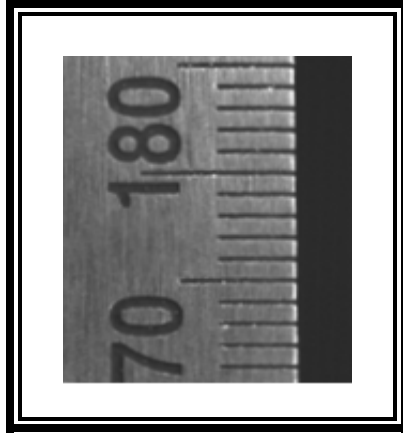


Figure 4.56: Scaling of the camera frame

The terminal velocity was found to be approximately 4.7 m/s for horizontal rice grain. Finally the drag coefficient was determined experimentally using Eqn. (4.5) which was also modified for the known particle shape and was found to be approximately 0.58. This result was validated with the numerical result⁴⁶.

$$C_D = \frac{\frac{8}{3} c g (\rho_s - \rho_f)}{\rho_f V_t^2} \quad (4.5)$$

4.4.2 Multiple Particle Drag Analysis

For multiple particle drag analysis, non-spherical particles with four sphericity range and five nominal diameter ranges were chosen. The sphericity range varied from 0.51-0.55, 0.56-0.60, 0.61-0.65, and 0.66-0.70. The sieve ranges for each sphericity range were 500-600 μm , 600-710 μm , 710-850 μm , 850-1180 μm , and 1180-2000 μm . Then for the analysis sphericity was assumed to be 0.53, 0.58, 0.63, and 0.68 which are the averages of the ranges specified. The diameters were chosen as 550 μm , 655 μm , 780 μm , 1015 μm , and 1590 μm .

Approximately 30 particle free falling at the terminal velocity were captured using the high speed camera. The terminal velocities were calculated using Eqn. (3.4) and then averaged for the mean terminal velocity estimation for all diameters at single particle sphericity. For the Reynolds number calculations, equivalent particle diameter was calculated from the nominal diameter. Then the drag coefficient was estimated from the Eqn. (3.5). Figure 4.57 presents the experimental drag analysis results with the Haider and Levenspiel Correlation for sphericity of 0.53 at different Reynolds number.

Figure 4.58 shows the results for sphericity 0.58, Figure 4.59 for sphericity 0.63, and Figure 4.60 shows the results for the sphericity 0.68. Then all the results are combined in Figure 4.61.

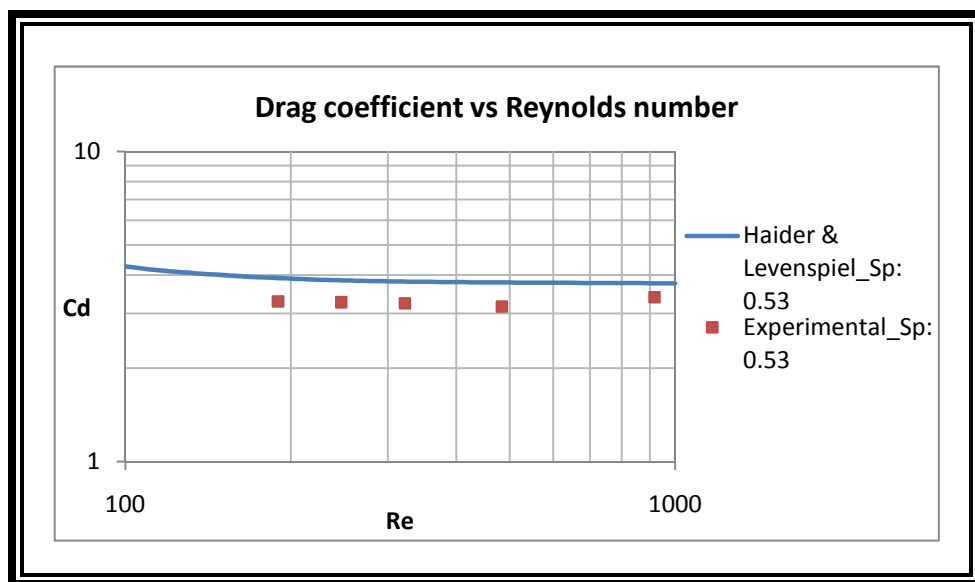


Figure 4.57: Drag coefficient for $\Phi = 0.53$

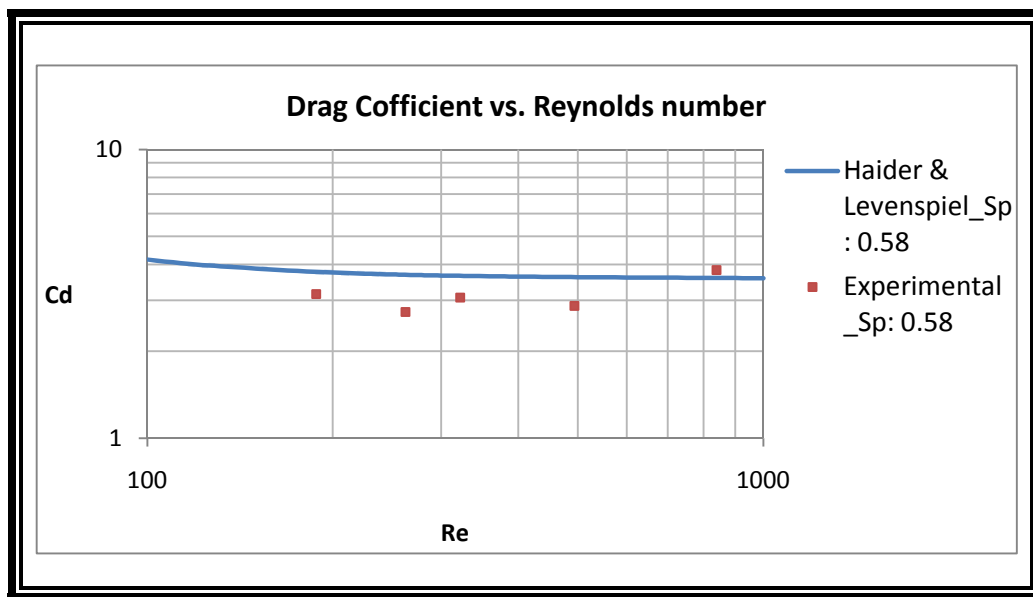


Figure 4.58: Drag coefficient for $\Phi = 0.58$

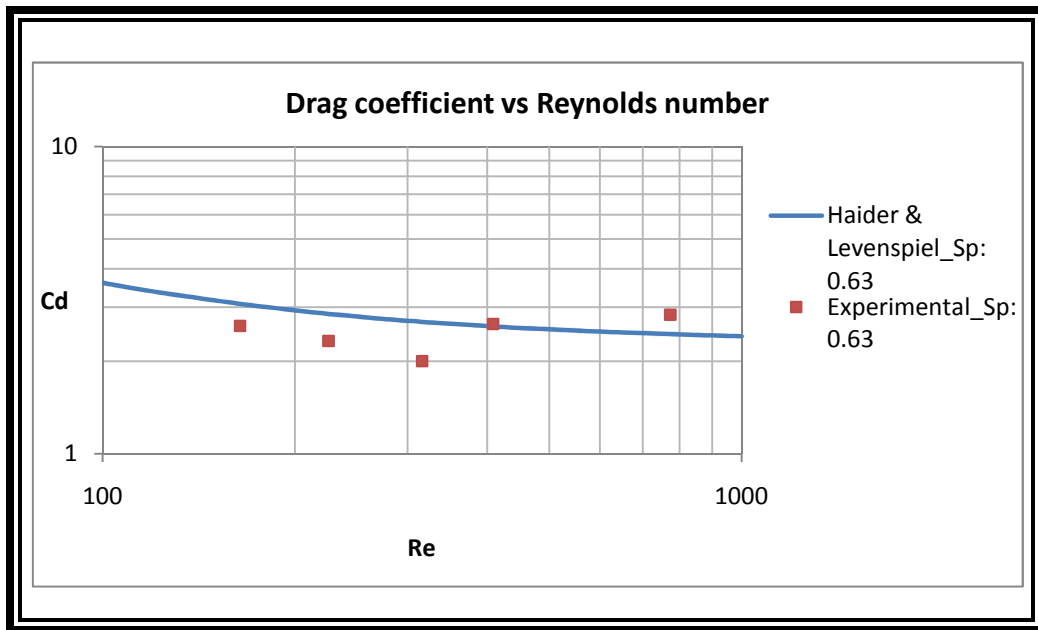


Figure 4.59: Drag coefficient at $\Phi = 0.63$

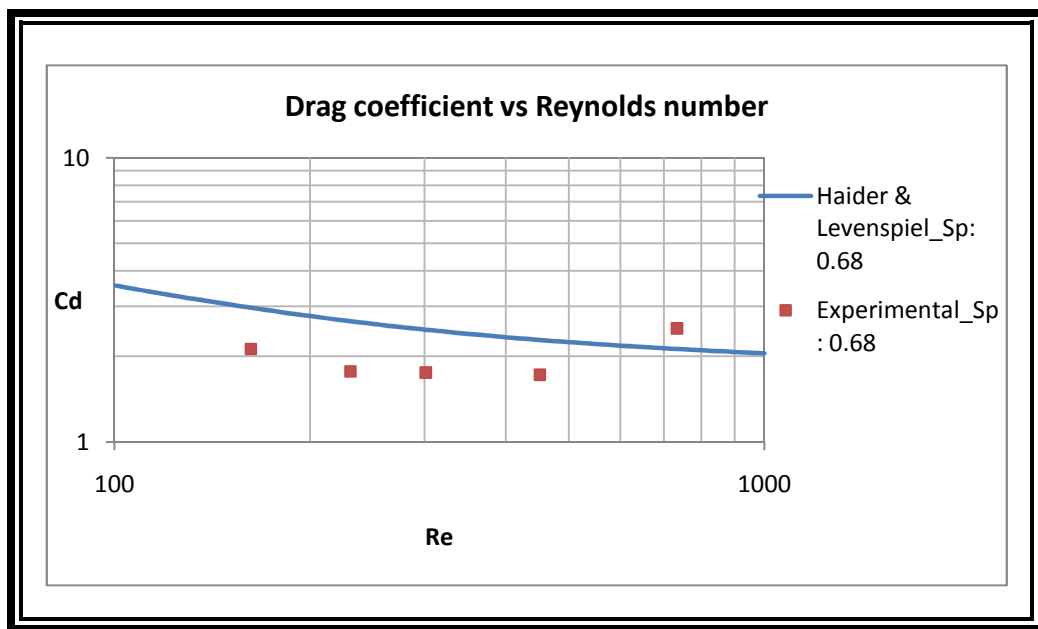


Figure 4.60: Drag coefficient at $\Phi = 0.68$

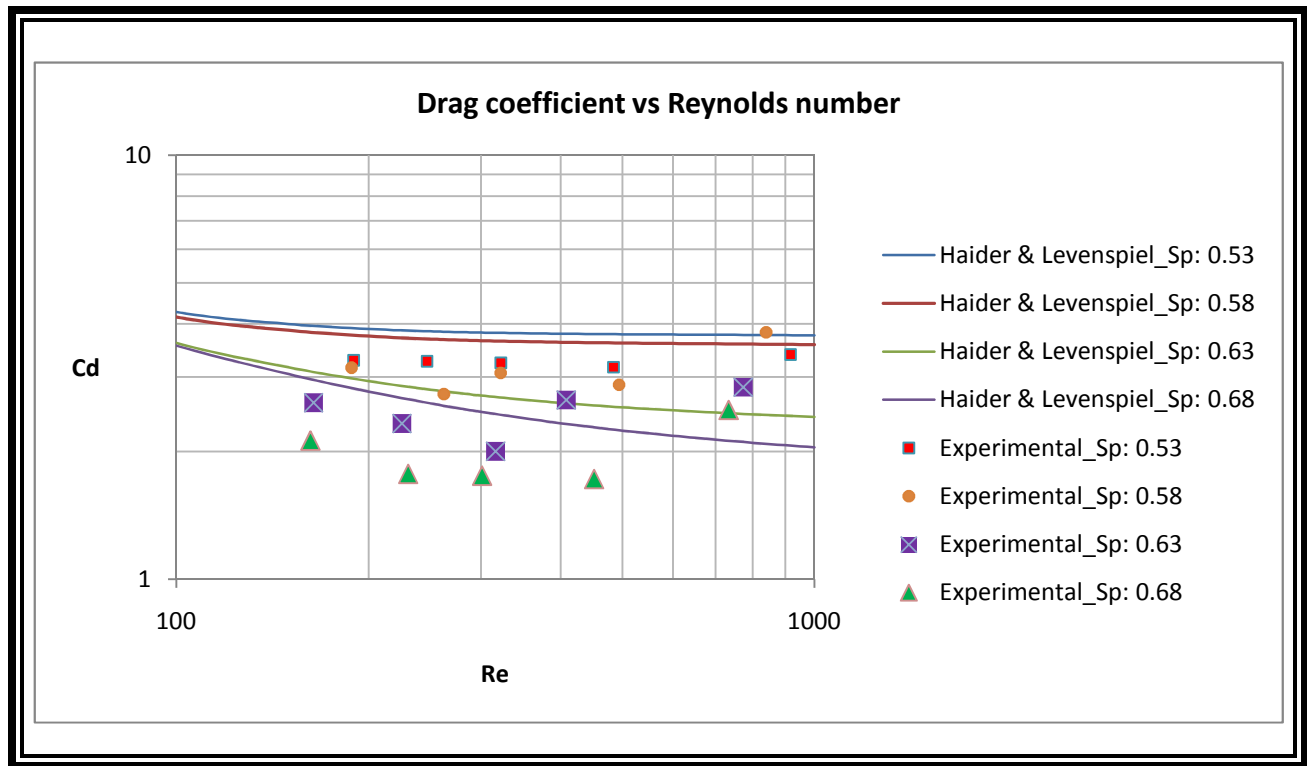


Figure 4.61: Drag coefficient for all sphericities

From these multiple drag analysis results, it could be observed that the experimental results are deviated from the empirical correlation. One reason for that might be the particle sphericity. Since the particles were chosen in a range rather than in a single quantity, and then all the calculations were performed using the average sphericity, hence, it might happen that most of the particles captured for velocity calculations might be in a sphericity range lower or higher than the average sphericity. Another reason is the particle diameter itself. Since, the sieve test technique provides the particle dimensions in a range, and then, the nominal diameter was calculated by averaging the sizes of two sieves, hence, it's not unusual that the particles captured are smaller or bigger than the average diameter.

Chapter 6: Summary and Conclusions

6.1 SUMMARY OF RESULTS

The popularity of fluidized bed combustion is largely due to the fuel flexibility of this technology. Almost any combustible material from coal to municipal waste can be burned with keeping the pollutant emission standards. The US Department of Energy set a goal for the last year to complete research and development for advanced power systems which will be capable of achieving 45 and 47 percent electrical efficiency at a capital cost of \$1,600 per kilowatt or less for a coal-based plant⁴⁷. Motivated by these issues, this thesis presented (1) hydrodynamic behavior of a fluidized bed operated with both spherical and non-spherical particles and (2) the drag force acting on non-spherical particles.

To achieve the first objective of this thesis, bed pressure drop analysis was performed with two different beds of different diameters. Bed performance was analyzed with performing the experiments at different static bed height of particles, with spherical and non-spherical particles. This thesis also develops a fundamental method to analyze the bed hydrodynamics by presenting the high speed imaging system to characterize different flow regimes.

For this two phase flow system, air was used as the gas phase and as the solid phase borosilicate glass particles were used. The pressure fluctuation across the bed primarily presents the bed behavior at the gas phase. To characterize the particle scale motion, initially the fundamental MatPIV analysis was applied. The MatPIV results reflect the solid particle properties in fluidization such as particle velocity, flow field vector, particle vorticity. After performing some fundamental analysis with the MatPIV, this thesis also presents some primary PIV results to characterize the particle scale motion in a fluidized bed. These primary results could be a baseline for more robust and useful PIV analysis characterizing the flow profile.

Since, in most real world applications of fluidized bed are associated with the use of non-spherical particles, hence, a comparative analysis of bed behavior with spherical and non-spherical particles was performed which reveals the behavioral deviation of the bed from the analytical solutions. This thesis also includes some design consideration factors such as flow distributor, bed diameter, bed

height, particle size and shape. This thesis presents some bed performance results showing the effect of flow distributor.

Drag force analysis required to uplift the particles in a fluidized bed reactor is also studied in this work. This is the second phase of this thesis. To achieve the drag coefficient for multiple non-spherical particles, single particle drag analysis with known sphericity and known dimension was performed and validated. With successful completion of this single particle drag analysis, this thesis attempts to document the some initial results with multiple non-spherical particles. The experimental drag data was then compared with the available drag correlation for non-spherical particles.

6.2 CONCLUSIONS

The following conclusions can be made from the current study presented in this thesis:

- Significant difference in pressure drop across the bed for spherical and non-spherical particles was observed. Since, a fluidized bed is designed considering the solid particles as spherical shaped whereas the particles used in the real practice are non-spherical most often; hence, the bed behavior shows significant deviation in the fluidization phenomena. Non-spherical particles with approximately similar size of spherical particles at same static bed height require less gas flow with almost similar bed pressure drop to initiate the fluidization. On the other hand the bed shows higher non-uniform fluidization behavior at the higher gas superficial velocities where the bed pressure drop is supposed to be approximately constant. An optimization of the particle size and shape should be made to overcome these issues.
- With increasing the particle bed height, the bed performance gets better with more uniform fluidization and increased bed pressure drop with approximately same gas flow requirement. Still each bed is limited to a certain height up to which the particle bed height could be used. After that height the bed performance is supposed to deteriorate. Hence, an optimum static bed height with gas flow requirement and bed pressure drop is required to be developed for the reactor design.
- The bed diameter plays an important role in the design and controlling a fluidized bed reactor process. With increasing the bed diameter the pressure drop requirement to start the fluidization decreases where the flow requirement increases on the other hand. In case of terminal velocity condition, the fluidized bed with larger diameter requires less gas flow to achieve the higher pressure drop to achieve the full fluidization than the bed with smaller diameter.
- At higher gas superficial velocity, the flow is extremely turbulent. Due to chaotic behavior of the flow, it is required to insert a flow straitening device to attain uniform flow distribution to the packed bed. The flow straighter also requires to be designed as perfectly as possible. Otherwise the channeling might be observed as presented in this

work. Here though the results do not show significant difference due to the distributor, it is required to make a perfect design of the flow distributor. This thesis concludes that the flow distributor used in the current study requires to be modified.

- This study presents a technique to investigate the flow field behavior characterizing different flow regimes such as packed bed regime, minimum fluidization condition, bubbling bed regime and turbulent churning regime. Since, a mesh catch was used at the top of the bed to restrain particles moving out of the bed after the turbulent churning regime, hence, the fast fluidization and pneumatic transport regimes were not captured here.
- The particle scale motion showing the flow field vector, particle velocity, particle rotational motion, are also included in this thesis to develop a fundamental idea regarding the flow profile for a gas-solid based fluidized bed.
- Pressure measurements suggest the importance of particle geometry and size in the design and optimization of fluidized beds.
- An electrostatic buildup is also observed in this process due to less moisture content in the supplied air, approximately 25%. On the other hand, particle interlocking might occur with higher moisture content. Hence, an optimized humidity condition is required to get better performance of a gas-solid based fluidized bed.

6.3 RECOMMENDATIONS FOR FURTHER STUDY

Some recommendations are made here to extend this thesis for further analysis and to overcome the limitations presented in this thesis.

1. The pressure measurement port is 2.54 cm above the bottom of the bed. This port could be made closer to get better pressure fluctuations across the bed.
2. The gas inlet port from the bed to the pressure transducer is covered by a brass screen to restrain the particles moving out of the bed through the pressure measuring port. This screen is supposed to provide some resistance to the flow or in other words, a pressure drop is supposed to occur in this screen which deteriorates the actual pressure drop readings.
3. The pressure drop used for the current study has an accuracy of $\pm 1\%$ FS, and the range of operation is too high (0-7500 Pa). This pressure transducer is not suitable for pressure drop sensing within a very small range. Hence, a differential pressure transducer with smaller range and higher sensitivity is supposed to improve the bed pressure drop measurements.
4. The honeycomb shaped flow straighter used here was 2.54 cm in length. A distributor larger length might provide more uniform flow distribution which in turn will provide better and uniform fluidization behavior across the bed.
5. A mesh catch was used to restrain particles moving out of the bed at the gas terminal velocity which makes the bed pressure drop increasing after the maximum fluidization region. A cyclone separator instead of this mesh catch could provide the actual bed pressure drop and the gas terminal velocity after the initiation of particle entrainment region.
6. The non-spherical particles used for the 2nd Gen fluidized bed were in a range of 150-2000 μm where approximately 30% of the particles were in the range of 150-355 μm . In this range, the particles are powders that become fluidized much earlier than the other bigger particles. This is why the bed pressure drop curves for the non-spherical particles show unusual behavior. This range could be made smaller and could be get as closer as

possible to the 1 mm size to produce some high quality, comparable, and useful data for the characterization of the fluidized bed.

7. The PIV analysis for the 2nd generation bed system was performed using a CCD camera of 62 Hz which captured and stored only 62 images per second. To generate a well defined average flow profile data 500 or more images are supposed to be analyzed. Hence, high speed PIV could provide better particle scale motion analysis results.

References

- ¹Clean Coal & Natural Gas Power Systems - Coal Gasification R & D website, U.S Department of Energy, URL: <http://www.fossil.energy.gov/programs/powersystems/gasification/index.html>.
- ²Fariborz Taghipour, Naoko Ellis, and Clayton Wong, "Experimental and computational study of gas-solid fluidized bed hydrodynamics," *Chemical Engineering Science*, Vol. 60, Issue 24, Dec. 2005, Pages 6857-6867.
- ³Li, S. "Modelling of the behaviour of gas-solid two-phase mixtures flowing through packed beds", *Chemical Engineering Science*, 200603.
- ⁴Christopher E. Brennen, "Fundamentals of multiphase flows", California Institute of Technology, Pasadena, California, Cambridge University Press, 2005, ISBN 0521 848040.
- ⁵Vivek V. Ranade, *Computational Flow Modeling for Chemical Reactor Engineering*, Vol. 5, Academic Press, California and London, 2002, Chap. 12.
- ⁶H. S. Fogler and L. F. Brown, "Reactors, ACS Symposium Series", vol.168, p. 31 1981, H. S. Fogler ed.
- ⁷Gasification- Wikipedia, the free encyclopedia. URL: <http://en.wikipedia.org/wiki/Gasification>
- ⁸Coal and Gasifier- Sasol: Mind Over Matter. URL: http://sasol.investoreports.com/sasol_mm_2006/html/sasol_mm_2006_9.php
- ⁹Pyrolysis- Wikipedia, the free encyclopedia. URL: <http://en.wikipedia.org/wiki/Pyrolysis>
- ¹⁰Oxidation and Reduction (electrons): Mnemonic. URL: http://ict4us.com/r.kuijt/en_oxidation_reduction.htm
- ¹¹Fluidized bed-Wikipedia, the free encyclopedia. URL: http://en.wikipedia.org/wiki/Fluidized_bed.
- ¹²BFB Combustion- mw power, Local Energy Solutions. URL: http://www.mwpower.fi/mwpower/mwpower_pages.nsf/WebWID/WTB-090422-22575-10279?OpenDocument
- ¹³Frontiers in Reactor Engineering- Science, AAAS.ORG. URL: <http://www.sciencemag.org/content/325/5941/698.figures-only>
- ¹⁴Rectilinear Vibrating Fluid Bed Drying Equipment (ZLC)- Changzhou Haoyue Drying Equipment Co., Ltd. URL: <http://czhaoyue.en.made-in-china.com/product/fbaEozdKhWY/China-Rectilinear-Vibrating-Fluid-Bed-Drying-Equipment-ZLG-.html>
- ¹⁵File: Fluidized Bed Reactor Graphics.SCG- Wikipedia, the free encyclopedia. URL: http://en.wikipedia.org/wiki/File:Fluidized_Bed_Reactor_Graphic.svg
- ¹⁶J. R. Howard, Fluidized Bed Technology: principles and applications, Adam Hilger; Adam Hilger, Bristol and New York, J R Howard 1989.
- ¹⁷Anaerobic downflow stationary fixed-film treatment (III) Anaerobic expanded/fluidized bed treatment (V) Comparison of high-rate anaerobic wastewater treatment reactors (VI), URL: <http://www.bvsde.paho.org/bvsair/e/repindex/rep154/anadow/anadow.html>
- ¹⁸Subramanian, Shankar R., "Flow through Packed Beds and Fluidized Beds" summary obtained from: W.E. McCabe, J.C. Smith, and P.Harriott 2001. Unit Operations of Chemical Engineering, McGraw Hill, New York, and Perry's Chemical Engineers Handbook, 7th Edition. 1997 (Ed: R.H. Perry, D.W. Green, and J.O. Maloney), McGraw-Hill, New York.
- ¹⁹SOLIDS NOTES 5, George G. Chase, The University of Akron, URL: <http://chemical.uakron.edu/fclty/chase/Solids/SolidsNotes5%20Fluidization.pdf>
- ²⁰Basu Prabir, Combustion and gasification in fluidized beds, CRC Press, 2006, Taylor and Francis Group.
- ²¹Gerardo Vargas Durate, "An Experimental Study of The Hydrodynamics of Multiphase Flow In Fluidized Beds", MS Thesis, Mechanical Engineering Dept., University of Texas at El Paso, El Paso, TX, 2009

- ²²J. M. Dalla Valle. Micromeritics. Pitman, London, 1948.
- ²³Phillip P. Brown and Desmond F. Lawler, "Spherical Drag and Settling Velocity Revisited", Journal of Environmental Engineering, ASCE, March 2003, DOI: 10.1061/(ASCE)0733-9372(2003)193:3(222).
- ²⁴Olumuyiwa Owoyemi, Luca Cammarata, Paola Lettieri, Derek Colman, "Analysis of different drag models for bubbling fluidized beds using CFD", Dept. of Chemical Engineering, University College London, and BP Chemicals Ltd, UK.
- ²⁵M. Syamlal and T. J. O'Brien. Computer Simulation of Bubbles in a Fluidized Bed. AIChE Symp. Series, 85:22–31, 1989.
- ²⁶D. Gidaspow, R. Bezburuah, and J. Ding. Hydrodynamics of Circulating Fluidized Beds, Kinetic Theory Approach. In Fluidization VII, Proceedings of the 7th Engineering Foundation Conference on Fluidization, pages 75–82, 1992.
- ²⁷C. Losenno and W.J. Easson, "PIV Measurements of Free-falling Irregular Particles", School of Mechanical Engineering, the University of Edinburgh, Scotland, UK
- ²⁸Drag Coefficient- Wikipedia, the free encyclopedia. URL: http://en.wikipedia.org/wiki/Drag_coefficient
- ²⁹Drag of Cylinders and Cones- Aerospace Web. URL: <http://www.aerospacweb.org/question/aerodynamics/q0231.shtml>
- ³⁰Ergun, Sabri and A.A. Orning. "Fluid Flow Through Randomly Packed Columns and Fluidized Beds", Industrial and Engineering Chemistry, vol. 41, pp. 1179-1184. The American Chemical Society: 1949, Washington D.C.
- ³¹Ergun, Sabri. "Fluid Flow Through Packed Columns", Chemical Engineering Progress, vol. 48, pp. 89-94. American Institute of Chemical Engineers: 1952, New York.
- ³²Davidson JF, Harrison D, Fluidization, Academic Press, New York, 1971, pp 471-450
- ³³J.P. Constantineau, J.R. Grace, C.J. Lim and G.G. Richards, "Generalized slugging-bubbling reactor model", Chemical Engineering Science 62 (2007) 70 – 81, Elsevier, 2006 DOI:10.1016/j.ces.2006.08.011
- ³⁴Bangyou Wu, Guang Yu, Celine Bellehumeur, Apostolos Kantzas, "Dynamic flow behavior measurements in gas–solid fluidized beds using different non-intrusive techniques and polyethylene powder", Elsevier Flow Measurement and Instrumentation 18 (2007) 197–203, 2007
- ³⁵Jan Albert Laverman, Ivo Roghair, Martin van Sint Annaland and Hans Kuipers, Investigation Into the Hydrodynamics of Gas–Solid Fluidized Beds Using Particle Image Velocimetry Coupled With Digital Image Analysis", The Canadian Journal of Chemical Engineering, Vol. 86, June 2008
- ³⁶J.E. Hilton, L.R.Mason, P.W.Cleary, "Dynamics of gas–solid fluidized beds with non-spherical particle geometry", Elsevier Chemical Engineering Science, 2009
- ³⁷M. Kumar, V. C. Srivastava, "Simulation of a Fluidized-Bed Reactor for Dimethyl Ether Synthesis", Chemical Engineering & Technology, Volume 33, Issue 12, pages 1967–1978, 2010, DOI: 10.1002/ceat.201000158
- ³⁸SS-1RS8-Swagelok Company. URL: <http://www.globalspec.com/datasheets/2609/Swagelok/F7588C6E-1E6A-4B5D-A2D1-A099735B7A86>
- ³⁹Differential Pressure Transmitter with Field Selectable Ranges-Omega.com. URL: http://www.omega.com/ppt/pptsc_lg.asp?ref=PX277&Nav=
- ⁴⁰Rahman, Md M., Ruvalcaba, M., Love, N., Choudhuri, A., "Investigation of Gas-Solid Fluidized Bed Dynamics with Spherical and Non-Spherical Particles", 49th AIAA Aerospace Sciences Meeting including the New Horizons Forum and Aerospace Exposition, AIAA, Orlando, Florida
- ⁴¹Terminal Velocity- Wikipedia, the free encyclopedia. URL: http://en.wikipedia.org/wiki/Terminal_velocity

⁴²Mario A Ruvalcaba, “An Investigation On The Mixing Hydrodynamics Of A Gas-Solid Fluidized Bed”, MS Thesis, Mechanical Engineering Dept., University of Texas at El Paso, El Paso, TX, 2009

⁴³Wen-Ching Yang, HANDBOOK OF FLUIDIZATION AND FLUID PARTICLE SYSTEMS, Marcel Dekker, New York, 2003, Article 12

⁴⁴J. Kristian Sveen, “An introduction to MatPIV v. 1.6.1”, Dept. of MATH, University of OSLO, Norway, 2004.

⁴⁵SAM BOGGS, JR., “MEASUREMENT OF ROUNDNESS AND SPHERICITY PARAMETERS USING AN ELECTRONIC PARTICLE SIZE ANALYZER,” *Journal of Sedimentary Petrology*, Vol. 37, No. 3, 1967, pp. 907-913.

⁴⁶Mario Ruvalcaba, MD Mahamudur Rahman, Norman Love, and Ahsan Choudhuri, “ Investigation of Non-Spherical Particle Drag In A Fluidized Bed”, 9th Annual International Energy Conversion Engineering Conference, AIAA, San Diego, California

⁴⁷Clean Coal & Natural Gas Power Systems-Coal Gasification, US Department of Energy website. URL: <http://www.fossil.energy.gov/programs/powersystems/gasification/index.html>

⁴⁸Combustion Technologies- US Department of Energy, National Energy Technology Laboratory URL: http://www.fossil.energy.gov/programs/powersystems/combustion/Fluidbed_prog031.pdf

Appendix A

Sample Calculations

Particle Mean Size

The sieve analysis results for the particle size distribution for the 2nd Gen bed are summarized below:

Sieve Size (μm)	Average Sieve Size (μm)	Weight of Particles (gm)	Weight (%)
2000	1590	54.0	14.41
1180			
1180	1015	36.8	09.82
850			
850	780	49.6	13.24
710			
710	655	33.3	08.89
600			
600	550	32.1	08.57
500			
500	463	31.5	08.41
425			
425	390	29.8	07.95
355			
355	253	107.6	28.71
150			

Now, the mean particle size calculations are shown below:

Mean Diameter

$$= \frac{\sum \text{Weight Percent} \times \text{Average Sieve Size}}{\sum \text{Weight Percent}}$$

$$= \frac{14.41 \times 1590 + 9.82 \times 1015 + 13.24 \times 780 + 8.89 \times 655 + 8.57 \times 550 + 8.41 \times 463 + 7.95 \times 390 + 28.71 \times 253}{100}$$

$$= 680 \mu\text{m}$$

Analytical Bed Pressure Drop

The analytical bed pressure drop calculation for the spherical particles at 5 cm bed height for 1st generation fluidized bed is shown below:

The measured particle mass for 5 cm bed was 78.87 g. The diameter of the bed was 3.8 cm.

Hence, using Eqn. (2.2), the analytical bed pressure drop,

$$\Delta P = \frac{M g}{A} = \frac{78.87 \times 9.81}{1000 \times \pi \times 0.019^2} = 682.19 \text{ Pa}$$

Gas Superficial Velocity

The volumetric flow rates obtained from the flow meters were converted to gas superficial velocity using Eqn. (2.7). An example of this calculation is shown below:

For the 1st Gen bed at 5 cm static bed height and at 100 lit/min volumetric flow rate, the gas superficial velocity, U_s should be,

$$U_s = \frac{Q}{A} = \frac{100 \times 0.000016667}{\pi \times 0.019^2} = 1.47 \text{ m/s}$$

Error Analysis

For 2nd Gen bed eight pressure measurements were taken at a gas superficial velocity of 1.67 m/s for 1 mm spherical particles and at 5 cm bed height at an interval of 30 minutes to perform the error analysis. This error calculation with a confidence interval of 95% is shown below:

The standard deviation calculations are presented below:

Number N	Bed Pressure Drop P (Pa)	Average Pressure P_avg (Pa)	Deviation, $D=(P-P_{avg})^2$	D_Total	D_Total /(N-1)	Standard Deviation $S=\sqrt{(D_Total/(N-1))}$
1	601.0913		514.6783			
2	631.5397		60.24695			
3	639.5335		248.2422			
4	622.7004	623.78	1.160844	891.2286	127.32	11.28
5	629.6554		34.54673			
6	621.1878		6.707813			
7	625.4991		2.962885			
8	619.0151		22.68289			

The uncertainty calculations are shown below:

1. Average pressure, $p_m = 623.78 \text{ Pa}$

2. Standard deviation, $S_x = 11.28$ Pa
3. Student T-value, t_x
 Let, $\alpha = 0.05$
 Degree of Freedom, $\nu = N-1 = 8-1 = 7$
 From the Student T-distribution table, at $\alpha = 0.05$ & $\nu = 7$,
 $t_{\alpha/2} = t_x = 2.36462$
4. Random Error, $P_x = t_x \times S/\sqrt{N} = 2.36462 \times 11.28 / \sqrt{8} = 9.43$ Pa
5. Confidence Interval:
 $CI = p_m \pm P_x = 623.78 \pm 9.43$ Pa = 614.35 to 633.21 Pa
6. Bias Error, $B_x = 1\%$ Full Scale of 3750 Pa = 37.5 Pa
7. Measurement Error, $\omega = \sqrt{(P_x)^2 + (B_x)^2}$
 $= \{(9.43 \text{ Pa})^2 + (37.5 \text{ Pa})^2\}$
 $= 38.67$ Pa
8. Hence, Average Bed Pressure = Pressure reading ± 38.67 Pa

Terminal Velocity of Free Falling Single Rice Grain

An object falling through a fluid under its own weight can reach the terminal velocity when the weight of the particle is balanced by the uplifting drag force and the buoyancy force.

$$W = F_b + D$$

Where W is the weight of the object, F_b is the buoyancy force, and D is the drag force acting on the object.

Since, the rice grain was assumed to be an ellipsoid,

Hence,

$$\text{The volume of the rice grain} = \frac{4}{3} \pi abc$$

$$\text{The projected area of the rice grain} = \pi ab$$

Where a is the equatorial diameter along X-axis, b is the equatorial diameter along the Y-axis and c is the polar diameter along the Z-axis.

Now,

$$W = \frac{4}{3} \pi abc \rho_s g$$

Where ρ_s is the density of particle and g is the acceleration due to gravity.

$$F_b = \frac{4}{3} \pi abc \rho_f g$$

Where ρ_f is the density of fluid.

$$D = \frac{1}{2} C_d V_t^2 \pi ab$$

Substituting the values from W, F_b , and D into the balanced equation,

$$V_t = \sqrt{\frac{\frac{8}{3} c g (\rho_s - \rho_f)}{\rho_f C_d}}$$

Flow Blockage Ratio

The flow blockage ratio was determined using Eqn. (3.1).

$$\beta = 1 - \frac{n \times \text{Cross sectional area of the hexagonal tube}}{\text{Cross sectional area of the column}}$$

Here,

r = Radius of the hexagonal tube = 0.1 inch

D = Inside diameter of the fluidized bed = 4.75 inch

Cross sectional area of the hexagonal tube = $\frac{3\sqrt{3}}{2} r^2 = 0.02598 \text{ inch}^2$

Cross sectional area of the bed column = $\frac{\pi D^2}{4} = 17.721 \text{ inch}^2$

Counted number of hexagons from the drawing file = 464

Hence,

$$\beta = 1 - \frac{464 \times .02598}{17.721} = 0.32$$

Appendix B

Key Parts and Instruments Specifications

Grainger 7AV38 High Pressure Blower

Description	Specification
Motor HP	5
Phase	3
Hz	60
Voltage	208-230/460
Full Load Amps	12.9-11.7/.8

Grainger 1JBF9 MILWAUKEE Butterfly Valve

Description	Specification
Valve Diameter	5 in
Flange Thickness	2.25 in
Rated PSI	200
Temperature Range	-25 to 250 F

SMC AC40-N043-Z Air Filter, Pressure Regulator & Lubricator

Description	Specification
Fluid	Air
Max. Operation Pressure	1.0 Mpa
Set Pressure Range	0.05 to 0.85 Mpa
Ambient and Fluid Temperature	-5 to 60°C (with no freezing)
Blow Material	Polycarbonate
Weight (kg)	1.74

INGERSOLL-RAND SSR-EP25 Air Compressor

Description	Specification
Capacity	97 CFM
Max Discharge Pressure	125 PSIG
Nominal Drive Motor	25 H.P.
Total Package Amps	64/32
Volts	230/460
Phase/Hz	Mar-60
Control Voltage	120

Omega FMA 1845 Digital Mass Flow meter

Description	Specification
Units	SLM
Range	0-1000 L/min
Type	Linear
Output	0 to 5 Vdc
Maximum Pressure	500 PSIG
Operating Voltage	12 Vdc
Accuracy	±1.5% of full scale

PHOTRON FASTCAM-Super 10K High Speed Camera

Description	Specification
Image Sensor	CCD
Features	High Speed recording up to 10000 fps
Recording media	IC memory (DRAM), 128 Mbytes
Recording rate	Full frame-512x480 pix and 30;60;125;250 fps
Recording capacity	546 full frames
Operating Voltage	12 Vdc
Shutter speed	1/recording rate;1/500 to 1/20,000

Octagon Digital 6242-10 Sieve Shaker

Description	Specification
Voltage	110 V
Phase	Single
Frequency	60 Hz

LOKO-Power Supply DPS-3050

Description	Specification
Input Voltage	115VAC \pm 10%
Output Voltage	0 ~ 50VDC (Adjustable)
Output Current	0~3A (Adjustable)

Omega PX277-30D5V Differential Pressure Transducer

Description	Specification
Excitation	12 to 35 Vdc
Output	0 to 5 or 0 to 10 Vdc (selectable)
Accuracy	\pm 1% FS
Operating temperature	0 to 175°F
Pressure Fittings	0.2" hose barbs
Pressure selectable ranges (inH ₂ O)	0 to 30, 0 to 15, 0 to 7.5, -15 to 15, -7.5 to 7.5, -3.75 to 3.75

Swagelok SS-1RS8 Needle Valve

Description	Specification
Flow Pattern	Straight (2-way)
Valve material	Stainless Steel
End Connections size	1/2 in
End Connections type	Swagelok® tube fitting
Max Temperature with Pressure Rating	450°F @ 3435 PSIG / 232°C @ 236 BAR
Orifice	250 in
Room Temperature Pressure Ratings	5000 PSIG @ 100°F / 344 BAR @ 37°C

Appendix C

Nomenclature

Ar	=	Archimedes number
d	=	Particle mean diameter
g	=	Acceleration due to gravity
M	=	Mass of solid particles
A	=	Cross-sectional area of bed
Re_{mf}	=	Reynolds number based on the minimum fluidization velocity
U_{mf}	=	Minimum fluidization velocity
U_T	=	Gas terminal velocity
V_t	=	Particle terminal velocity
ε	=	Turbulent dissipation rate
ε_{mf}	=	Void fraction
ϕ	=	Sphericity factor
μ_f	=	Fluid viscosity
ρ_f	=	Fluid density
ρ_p	=	Particle density
Δp	=	Bed pressure drop
C_D	=	Drag coefficient

Curriculum Vita

Md Mahamudur Rahman, the youngest son of Md Muslim Ali and Hasina Bakool, was born on October 17, 1985 in Dhaka, Bangladesh. He completed his high school degree from Notre Dame College, Bangladesh and joined Bangladesh University of Engineering and Technology (BUET), Bangladesh in 2002 to pursue his Bachelor of Science in Mechanical Engineering degree. During this time he worked in the field of solid mechanics as his thesis and also developed a computer interfaced alarm with heat sensor and smoke detector as his undergraduate project. After completing his bachelor's degree, he took admission in The University of Texas at El Paso (UTEP) in January 2010 to pursue his Master of Science in Mechanical Engineering degree. For the last one and half years he has worked in the Center for Space Exploration and Technology Research (cSETR) as a Graduate Research Assistant where his research focus is on investigating the hydrodynamics of a gas-solid fluidized bed operated with both spherical and non-spherical particles experimentally. During his first semester he submitted an abstract for the American Institute of Aeronautics and Astronautics (AIAA) 2010 conference paper. His accomplishments include publishing one conference paper from AIAA, one conference paper from International Energy Conversion Engineering Conference (IECEC), one article for Southwest Energy Science and Engineering Symposium, and submitting two conference paper abstracts for AIAA 2012, and being secretary of the Bangladesh Student Association (BSA) at UTEP, and student member of the AIAA.

Permanent address: 54 East Bashaboo, 2nd Floor (Right Side)
Dhaka- 1214, Bangladesh

This thesis was typed by Md Mahamudur Rahman